A STUDY OF THE ELASTIC AND INELASTIC SCATTERING OF ALPHA PARTICLES BY LITHIUM-7

Thesis by
Ronald Y. Cusson

In Partial Fulfillment of the Requirements
for the Degree of
Doctor of Philosophy

California Institute of Technology
Pasadena, California
1965
(Submitted May 25, 1965)

ACKNOWLEDGEMENTS

We gratefully acknowledge the help of the entire staff of the Kellogg Radiation Laboratory, without whose collaboration this work would have been impossible.

We wish to thank in particular Professor C. A. Barnes who originally suggested this problem and who supplied constant encouragement throughout this work, Professor T. Lauritsen with whom we have had many enlightening discussions on models for light nuclei, and Professor W. Whaling for help in comparing our results with previous published work.

We thank Barbara Zimmerman and the staff of the Booth Computing Center for their assistance in performing the many computer calculations involved in this work.

Finally, we acknowledge the essential financial assistance of a Navy Contract research assistantship and recently, a fellowship from General Atomic Division of General Dynamics Corporation.

ABSTRACT

The absolute cross sections for the reactions $Li^7(\alpha, \alpha)Li^7$ and $Li^7(\alpha, \alpha')Li^{7*}(.48)$, have been measured in the range of energies and angles, $1.6 \leq E_{\alpha L} \leq 12.0$ MeV, $20^o \leq \theta_{\alpha L} \leq 150^o$, using thin Li^7-bearing targets. Solid state detectors were used to detect the scattered α-particles. Nineteen scattering anomalies have been observed in this energy range. In the excitation energy range, $9.88 \leq E_{exc.}(B^{11}) \leq 11.27$ MeV, six levels were observed. The measured cross sections were fitted in this energy region using a multilevel R-matrix theory model-program for the 7094 computer. The best fits were obtained with the assignments: $9.88(3/2^+)$, $10.26(3/2^-)$, $10.32(5/2^-)$, $10.60(7/2^+)$, $11.0(5/2^-)$, $11.27(7/2^+, 9/2^+)$. Some alternatives for these assignments are discussed. The results were found to be consistent with the level structure of the analogue nucleus C^{11}. The applications of the rotator model of the nucleus to the excited states of B^{11} and C^{11} are discussed.

TABLE OF CONTENTS

I. INTRODUCTION

A nuclear, multi-channel, two-body scattering experiment may emphasize several points of view depending on the predominant reaction mechanism.

A matrix quantity, called the collision lifetime $\underset{\approx}{Q}$, which is often found useful when classifying such mechanisms, can be defined by the equation

$$\underset{\approx}{Q} = \underset{\approx}{S}(t\underset{\approx}{S})^{\dagger}$$

where $t = \hbar/i\frac{\partial}{\partial E}$, $\underset{\approx}{S}$ is the unitary S matrix, $\dagger$ denotes hermitian conjugation.

The matrix $\underset{\approx}{Q}$ can be diagonalised. It can be shown[1] that if, for some value of the total energy E, the eigenvalues of $\underset{\approx}{Q}$ are large compared to R_o/v, where R_o is an approximate range for the interaction and v is the relative velocity of the fragments in the incoming channel, then metastable states of the whole system will be formed whose structure is well defined. These states are usually called resonances of the compound system(nucleus). If, on the other hand, the above condition is not realized, several types of reactions are possible, some of which ("direct" type) can yield information concerning the residual system. In this study we shall be mostly interested in the first case, that is resonant scattering, and assume the properties of the residual system known.

Figure 1 shows the status, before this experiment, of the energy level diagram for B^{11}, the compound nucleus formed in the resonant scattering of alpha particles on Li^{7}. Some relevant

features of this diagram are:

a) Few levels above an excitation energy of 8.57 MeV have spin and parity assignments.

b) The (Li^7, α) channel which opens at 8.67 MeV excitation and the (Li^{7*}(.48), α') channel which opens at 9.15 MeV provide the only heavy particle decay modes up to about 11.4 MeV where several other channels open within a few hundred keV.

c) Several levels in that energy region have been seen only in the reaction $Li^7(\alpha, \alpha')Li^{7*}$(0.48), by observing the .48 MeV deexcitation gamma ray[2-4].

From these and other considerations discussed below it was felt that a detailed investigation, as a function of energy and angle, of the alpha particle yield from the present reactions might shed light on these highly excited states of B^{11}.

Recent successes in generating the normal-parity ground-state level sequence[5, 6] from rotational model considerations suggest that a similar effort be applied to excited level sequences, although additional complications are to be expected. For example, evidence has been found[7] in the case of Be^9 for such an excited sequence, as predicted by the Nilsson Model[8].

Since new level assignments have been obtained recently by Overley[9, 10] in the mirror nucleus C^{11} at excitation energies for which the analogue states in B^{11} are accessible <u>via</u> alpha plus Li^7 scattering, there is an additional incentive for this experiment. Any spin assignment we can get for B^{11} helps us identify the analogue state and/or allows a confirmation of the C^{11} assignments.

We shall discuss in order, the experimental techniques used, the treatment of the raw data before analysis, the precision of the data, the analysis of such data in the framework of R-matrix theory, the results of the analysis, and finally, a comparison of the results with various nuclear models.

II. ACQUISITION OF DATA

A. Description of Apparatus

1. The Alpha Beams

The beams of alpha particles were supplied by two different electrostatic generators (E. S. G.) of the Van de Graaff type located in the Kellogg and Sloan buildings on the C. I. T. campus. For laboratory beam energies below 3.22 MeV, the Kellogg 3-MeV E. S. G. was used. Above this energy and up to 12 MeV the O. N. R. - C. I. T. tandem accelerator was used.

a) The low energy beam

This beam is first analysed magnetically to select the 1^+ charge state and then passes through an electrostatic analyser (E. S. A.) to define its energy within about 2-5 kev[11]. The analyser calibration was redetermined using the standard Li^7(p, n) threshold technique[11] and found consistent with the previous measurements within the accuracy quoted above. Two sets of tantalum cups placed at the exit of the E. S. A. defined a square beam, 1 mm on the side, at a distance of approximately 24 cm from the target (see Figure 2 for a schematic view of the target chamber). A sharp focus indicated by maximum beam intensity in the target chamber was first obtained; then the beam was defocussed at the ion source by decreasing the focus electrode voltage until the intensity dropped by about a factor of two. Stable α^+ beams of about .05 microamperes were consistently obtained this way. After several hours of bombardment thin targets showed a uniform blackening over the 1 mm square area hit by the beam. The meaning of this blackening will be discussed under target properties.

Beam integration was performed using the electrometer-tube beam-integrator which is part of the electronic equipment of the 3-MeV E. S. G.. It was found that +900 volts on the target was sufficient to insure that the beam intensity measured with and without target was the same to about 5% at all energies employed. An electron suppressor with a 3 mm diameter hole was placed inside the target chamber and maintained at -300 V. A beam "scraper" with a 1.6 mm diameter hole helped keep slit scattering from being observed in the counter.

Figure 2 shows the general layout of the target chamber. A cold trap extension can be seen in the figure. We will comment on it when discussing target properties.

b) The high energy beam

At energies between 3.22 and about 4.5 MeV we have used the singly charged beam from the tandem accelerator. Above 4.5 MeV the doubly charged beam is more prolific and was thus used. The highest energy data were taken at 12 MeV alpha lab energy.

Due to the particular beam-optical focussing system of the tandem accelerator, the tandem beams were found to be consistently less uniform over a 1 mm square area at the target than those of the 3-MeV E. S. G.. Beam collimation at the entrance to the target chamber (11" diameter in this case) was done twice, first, 5 feet from the target with a square aperture 1.2 mm on the side, and again 1 foot from the target with a 1 mm square aperture, these apertures being defined by tantalum slits. After alignment and maximization, the beam was defocussed at the target room quadrupole, located about 10 feet from the target, by a factor of 6 to

8 in intensity. This beam was still often found to have a "hot" spot in its center. The procedure would be repeated until a better beam was obtained. Indeed the intensity distribution seemed to vary with time in a difficult-to-predict fashion. When taking small energy steps it is fairly easy to hold the beam current at a fixed value but due to the lack of a beam profile scanning device it was not possible to guarantee the uniformity throughout a large number of energy changes. Target depletion is sensitive to beam uniformity so that the only recourse during excitation runs was to come back frequently to a given energy to check the target depletion. For angular distributions this problem was less severe since the beam focussing was then left undisturbed.

In the 11" scattering chamber used here the target was held at ground potential and the beam was stopped in a 2"-diameter x 6"-long Faraday cup, 1 foot beyond the target, which was held at 50 V. above ground potential. The doubly-charged alpha beam appeared unchanged to within 1% when the thin target was put in the beam. The singly-charged beam was stripped to doubly-charged upon passing through the target and the measured beam current was doubled (to an accuracy of 1%). Again the same cold trap extension was used during the tandem experiments in order to decrease the accumulation of contaminants on the bombarded area of the target.

2. Detectors and associated Electronic Circuitry

Scattered charged-particle energy spectra were obtained using solid state Au-Si surface barrier detectors 200 microns or more in thickness. A counter energy resolution of 40 keV or better was demanded from the detector although the line width due to the

target thickness was often 75 keV or more, especially at low bombarding energy. A low-electrical-capacity connection coupled the detector to a low-noise charge-sensitive preamplifier. The output from the preamplifier was then shaped, amplified to a 20-50 V. level and fed to a 400-channel transistorised pulse height analyser. The analyser and sometimes also the beam were gated by the current integrator. Spectra of 200 channels or less were recorded on punched paper tape for subsequent analysis.

The gamma-ray excitation curve shown in Figure 3 was obtained using a 2" x 2" NaI scintillator crystal "integrally-mounted" on a photomultiplier tube and inserted in a 2"-thick cylindrical lead shield[12]. The crystal was placed 7" from the target at 90 degrees to the beam axis, and viewed the gamma rays through a 1/2" x 2" diameter lucite port. A transistorized phototube preamplifier fed the signal to the same pulse-height analyser system as used for obtaining charged-particle spectra.

3. Target Chamber and Detector Geometry

In setting up the target chamber and counter geometry we had in mind the following considerations:

a) The incident beam should be parallel, uniform and monoenergetic. In addition, it should be possible to collect all the beam after passage through the thin target.

b) The target (and the target holder) should be reproducibly locatable in height and angle with respect to the beam axis, should not intercept the incident or the scattered beam and should introduce no appreciable degradation of the non-scattered beam.

c) The counter collimator should see just the bombarded area, introduce no appreciable additional collimator scattering and define the laboratory angle.

d) Since the bombarded area seems to be chemically very active, the vacuum around the beam entrance and target should be good and particularly free from hydrocarbon vapours.

These requirements led to the configuration sketched in Figure 2, for the low energy part of the experiment, which was performed in a 5.5"-diameter target chamber. The same counter collimator and cold trap extension were used at higher energy in the 11" chamber.

The large chamber configuration was similar. There the initial angular calibration was done by sighting with a telescope along the optical axis of the beam. The active area on the counter was defined by a .015" x .200" vertical slit made from tantalum .005" thick. The plane of this slit was at a distance of 1.75" from the target. The broadening of the angular aperture at $\theta_L = 20$ degrees due to the vertical extension of the counter collimator slits, was calculated and found to be unimportant.

This concludes our description of the apparatus. It is by no means exhaustive and indeed we have discussed only those points which were either of special relevance for this experiment or which have caused difficulty.

B. Target Preparation and Properties

The targets we used to collect the data presented in this thesis consisted of thin layers of Li^7OH or Li^7F, supported on thin carbon-

foil backings. Our method for making carbon foils is essentially identical to the one used at Harwell by Dearnaley[13]. Our only comment on this point is that, in the art of self-supporting thin-film fabrication, moderate care is no virtue and exaggerated cleanliness is no vice. The target layer was sometimes evaporated while the carbon was still on the glass and sometimes on the mounted foil. We have produced good targets using both methods. To make the hydroxide targets, Li^7 metal was evaporated in vacuo on the backing and allowed to form Li^7OH by introducing water vapour in the bell-jar. To make the other type of target, Li^7F was evaporated directly on the backing. Our success rate in making targets turned out to be, on the average, about 25%. The average thickness of the carbon backing was about 10 $\mu gm/cm^2$ and no foils thicker than 15 $\mu gm/cm^2$ were used.

To calculate the energy loss of alpha particles in our targets, we have used the formulae[14]

$$\left.\frac{\epsilon_\alpha}{\overline{Z_\alpha^2}}\right|_E = \left.\frac{\epsilon_p}{\overline{Z_p^2}}\right|_{E/4} \qquad \text{(II-1)}$$

$$\epsilon_{mol.}(X_aY_b) = a\epsilon_{at.}(X) + b\epsilon_{at.}(Y)\,, \qquad \text{(II-2)}$$

where $\epsilon_\alpha|_E$ is the specific energy loss of alpha particles at the energy E, etc. $(\overline{Z^2})$ was evaluated from Zaidins's graphs[15]. The resulting curves for the energy loss vs E are presented in Figure 4. We have found that, for $E < 2$ MeV, the energy loss was higher than the values given by the graph. In fact the dotted line shown in the graph, obtained by putting $\overline{Z^2} = 4$ at all energies,

seemed to give agreement with our observed value for the energy loss at about 700 keV.

In Figure 5 we present a semi-log plot of a pulse-height spectrum obtained by scattering alphas from a fresh carbon foil, at 90 degrees in the laboratory and at 2 MeV lab. incident energy. The high atomic weight contaminants probably come from the release agent used (Duponol C, a brand of sodium lauryl sulfate, similar to Shell "Teepol", which is recommended by Dearnaley) and have caused no difficulty. However, the low energy asymmetry of the elastic peak (often more pronounced than that shown in Figure 5) and the rising low energy background were severe experimental limiting factors. At backward angles, the scattered alpha particles from lithium have low energy and so could not be well resolved from the background. The forward angle alpha groups merged with the elastic alpha groups from the other constituents of the target and thus could not be well separated at very forward angles (θ_L < 25 degrees lab.). A foil, sufficiently thick to stop 100-keV alphas, was inserted in front of the counter and did completely remove the low energy rising background; from this we concluded that it was composed of heavy charged particles. We have also verified that it was present at all settings of the counter angle. Further tests were made to determine the origin of this background. When the target foil was removed and the foil holder was otherwise left undisturbed, the low energy background disappeared; this meant that it was not due to stray beam scattering from the target holder. A low Z (Al^{27}; the target chamber is made of steel!) anti-scattering baffle was placed on the opposite side of the target chamber, facing the counter aperture; this made no difference and thus eliminated rescattering

effects associated with the target chamber, as a source of the background. We then proceeded to compute the shape of the energy spectrum, resulting from single and double scattering in a thin target; we found that this spectrum has a low energy rising background roughly proportional to $1/E^3$ and an asymmetrical line shape. For a target thickness of 500 Å, however, the calculated effect was smaller, by a factor of 10, than the observed one. It may be that target non-uniformity tends to enhance it. Another possible explanation is that we were observing the true beam energy distribution, as defined by the tantalum slits, the low energy component being produced by energy losses in the beam passing through the edges of the slits.

We have also studied the line shape of the elastic alphas from C^{12} and Li^7 with a 16" double-focussing magnetic spectrometer[16]. The superior resolution of the magnetic spectrometer allows an actual measurement of the energy loss inside the target. Knowing the approximate magnitude of the nuclear cross sections involved one could then compute a value for the specific energy loss in the target. Figures 6 and 7 show typical inverse-momentum spectra. In the case of C^{12} (Figure 6) we could unfold the spectrometer line shape. This proved more difficult for the Li^7OH target for various reasons, which we will not discuss here. There is an alternate method, possibly less accurate but sufficient for our purpose, to measure the energy loss of the incoming beam in the target, which we will describe shortly.

We now turn to a short discussion of the problem of carbon buildup on the bombarded target spot. Figure 8 shows a profile of the alphas elastically scattered by the carbon present in a Li^7OH target after approximately 1000 microcoulombs of bombardment at about 2.75 MeV. This was done with "reflection geometry", and

with the Li^7OH deposit facing the counter. The main carbon peak, due to the backing, is shifted as expected. One also notices a sizeable contribution all the way through the target due to carbon accumulation. This was also clearly visible in spectra made with solid-state counters. Such targets when inspected visually at atmospheric pressure were definitely opaque, while the part not bombarded was definitely transparent. It is to minimize this effect that a cold trap extension was installed. We have found that the trap extension decreased the carbon accumulation rate by a factor of 5 or more.

Another way to measure the energy loss of the incident beam in the target is to look at narrow resonances in the yield as a function of the bombarding energy. There is one such peak in the reaction considered here, $Li^7(\alpha, \alpha')Li^{7*}(.48)$, at $E_L = 3.03$ MeV (see Figure 3). We define the target angle as the angle between the normal to the target plane (on the backing side) and the beam direction. We first measure the excitation function over the resonance, at $\theta_L = 60^\circ$ and a target angle of 0°. This is then repeated with a target angle of 60°, which doubles the target thickness. A comparison of the two yield curves reveals a shift in the peak position and a broadening of the line, the magnitude of the effect depending on the ratio of target thickness to the width of the resonance. By folding a Breit-Wigner line shape of width Γ with a rectangular target window, one finds the relation between the target thickness ΔE_t and the shift of the peak. Figure 9 shows the effect for $\Delta E_t = 0$, $\Gamma/2$, Γ with normalization to the same total number of scattering nuclei. We have measured these two excitation functions with a target whose thickness was independently estimated to be about 65 keV (from a magnetic spectrometer measurement). Good agreement with the

curves no. 2 and 3 of Figure 9 was found. A simple calculation gave the values $E_r = 3.03 \pm .015$ MeV and $\Gamma_L = 110 \pm 15$ keV after the target thickness corrections. Similar yield curves were measured at the tandem laboratory both as a check of target thickness and energy calibration. All our data were taken with targets satisfying $\Delta E_t/2 \lesssim 30$ keV, at $\theta_t = 45^o$ and $E_L = 3.1$ MeV., with one exception: the data shown in Figures 11 and 12 above 7.5 MeV were taken with a $\Delta E_t/2 \simeq 250$ keV target and shifted accordingly. All angular distributions runs were corrected by raising the beam energy by $\Delta E_t/2$.

The quality of a target was gauged by considering the peak-to-valley ratio of the number of counts, in the pulse height spectra of the alpha particles scattered at $\theta_L = 60^o$. A few very good targets yielded useable data down to $\theta_L = 20^o$, with a peak-to-valley ratio of 10^3 or higher at $\theta_L = 60^o$ (compare Figure 10). During prolonged bombardment the peak-to-valley ratio decreased. Targets were discarded when it became less than 50.

Target depletion was often a problem for the high energy part of the experiment. All targets showed a slow depletion rate of about 1%/100 microcoulombs, although occasionally some targets would be depleted by as much as 50% in a bombardment of 100 microcoulombs. Data from the latter targets were rejected, while the data from the former were corrected for depletion.

C. Running Procedure

Once the beam was obtained as explained previously, energy spectra were compared with the scattering kinematics to confirm the identity of the scattering nucleus. Since separated Li^7 was used throughout the experiment this was relatively simple.

During excitation function runs, frequent checks at a given energy were performed when depletion was suspected. No angular distributions showing depletion greater than 1% per point were analysed.

The target condition was monitored by noting the target chamber vacuum (always $\leq 5. \times 10^{-6}$ mm Hg), the peak-to-valley ratio, and the size of the carbon scattering edge. For each run, the following information was recorded: date and run number, beam energy (E. S. A. or N. M. R. setting), counter and target angles, energy spectra from the analyser on punched paper tape, analyser live-time, clock-time, channel no. of elastic and inelastic peaks, charge integrated and approximate beam intensity.

Yield curves as a function of bombarding energy were done first (Figures 11 and 12) to locate the resonances, and then angular distributions at fixed energies (Figures 14, 17-20). We have taken data in the energy range 1.5 MeV $\leq E_{\alpha L} \leq$ 12 MeV and the angular range $25^{o} \leq \theta_{\alpha L} \leq 150^{o}$ with varying detail, depending on the amount of information wanted in any energy region. Thirty-eight angular distributions were measured containing on the average 15 angles each. These plus the excitation functions (Figures 11, 12 and 16), in steps of 100 keV or smaller, constitute the data obtained for this study.

III. ANALYSIS OF THE DATA

A. Reduction of the Spectra

A typical solid-state counter spectrum is shown in Figure 10. An average data collection session would result in 30 to 100 such spectra taken at various bombarding energies and laboratory angles. The reduction of a spectrum consists in summing the counts under the relevant peaks, subtracting the background, normalizing to a given amount of charge, correcting for dead time, effective target thickness (which was changed either when a new spot was selected or the target angle changed) and performing depletion corrections when applicable. When this is done, one has a set of 30 to 100 numbers which are each proportional to a differential cross section in the laboratory system of coordinates and all have the same relative normalization.

Since over 1000 spectra were recorded on punched paper tape, it was not found practical to carry out the plotting and reduction by hand. A program was written for the Datatron 220 computer, located in the Booth Computing Center, to plot the spectra on a digitilized point plotter under program control. This program and a few other simple ones, which were used for data reduction and analysis, will not be described here since they represent rather standard coding techniques and involve no interesting physics or mathematics.

Once the plots were obtained, the background was drawn in by hand from the knowledge of the spectrum shape for a similar target without Li^7 in it. The number of background counts per channel along with dead time, live time, and integration normalization were punched on paper tape. We spliced this tape to the data tape and

used the resulting reel of tape as input to another program which summed the peaks, subtracted the background and performed the two other corrections. The partially corrected yields obtained at this point, were then plotted vs. energy or angle, as needed, to detect gross errors which were then corrected. The final correction for relative target thickness was done by hand. At this point we had laboratory angular distributions and yield functions.

B. Absolute Normalization

Li and Sherr[11] have obtained absolute normalization for the total inelastic cross section of the reaction $Li^7(\alpha, \alpha')Li^{7*}(.48)$, using thick target techniques, with a probable error $\leq 20\%$. This normalization was used in Figure 3, where we have extended their work and that of Bichsel and Bonner[2] to higher energy. Figure 3 was used to supply the absolute normalization for the whole experiment, as we will explain shortly. The usual normalization in experiments of this type consists in assuming Rutherford scattering at forward angles and low energy ($E_{\alpha L} \leq 1$ MeV would be required in this case). This method was not found practical here because of the difficulties involved in making accurate low-energy thin-target measurements, with an alpha beam and a LiOH target.

The next step was then to normalize all the angular distributions and yield curves with respect to one another. To do this we first plotted the excitation functions for the elastic and inelastic scattering yield at $\theta_L = 60^\circ$, from $E_L = 1.5$ MeV to $E_L = 12$ MeV. This curve was measured several times, with various targets, in overlapping fashion. This assured us of a correct relative normalization to about 10% from the lowest energy to the highest. We then used this yield curve to normalize the angular distributions to one

another. Thus, at this point, all the data at all energies and angles, contained one normalization constant (called CNO, in Fortran language). These laboratory cross sections were next converted to the center-of-mass system with the help of a simple Fortran program.

The last step in determining cross sections from the data was to evaluate the number CNO defined above. To do this we have fitted, using the standard least-squares method[17], the inelastic angular distributions with expansions in Legendre polynomials. Although the coefficients C_L of the Legendre polynomials $P_L(\theta)$ proved rather unstable, for $L \geq 1$, as L_{max} was increased up to 6, the coefficient C_0 could be obtained reliably. Figure 13 shows the energy dependence of this coefficient. Since it is proportional to $\sigma_{I,\,total}$, which we already know (Figure 3), and CNO, which we want to determine, the problem is solved. The error flags in Figure 13 indicate the average fluctuation of C_0 as L_{max} was increased in integral steps from 1 to 7. The agreement with the gamma ray (.48 MeV) yield curve is good so that the relative normalization is accurate to approximately 5%. This scale was used in Figures 11, 12, 14, 16, 17-20, all showing measured cross sections.

C. Accuracy of the Measurements

The sources of error on the stated values of the cross section are: a) counting statistics, b) background subtraction, c) target thickness instabilities, d) energy variation of the beam integration efficiency, e) variations in the pulse height analyser efficiency with counting rate (dead time corrections), f) uncertainties in the absolute normalization constant derived from the work of Li and Sherr.

We have found that background subtraction was a much more important source of errors than the counting statistics, for the integrated charge we have used. The statistical error on the number of counts in a peak was, on the average, 3% (1000 counts) for the elastic peaks. Although the background could be consistently estimated, it is difficult to state the absolute accuracy with which it could be determined. For $E_{\alpha L} < 2.7$ MeV, we have estimated the background subtraction error to range from 2% to 50%, in the best and worst cases respectively. One may get a rough idea of these two effects by noting the scatter of the points in Figures 14, 17-20. The errors due to target instabilities in our final values of the relative cross sections are no more than 2-4%, due to the multiple-checks system we have used during the runs. For $E_{\alpha L} > 2.5$ MeV we claim 5% accuracy in beam collection efficiency stability; in the region $1.5 \text{ MeV} \leq E_{\alpha L} < 2.5$ MeV, 10% accuracy represents a fair estimate. No reliable data were obtained below $E_{\alpha L} = 1.5$ MeV due in part to this effect. We have always taken care to keep the multichannel analyser dead-time below 20%, and the beam intensity constant during a run. We have verified that under those conditions the dead time correction was correct within 2%. The Li and Sherr measurement is quoted to about 20% accuracy. This represents the greatest uncertainty; on the other hand it is certainly the hardest number to obtain.

Thus, the overall absolute accuracy of our measurement is about 22% for the elastic cross section and 26% for the inelastic cross section.

D. Extraction of Resonance Parameters

The object of this section is to outline the procedure we have used to determine the spins and parities of some of the levels observed in this experiment.

What we have done is to specialize the general expansions of R-Matrix theory[18] to the case of two channels only. A computer program, written in Fortran language, was used to calculate angular distributions and yield curves for a given set of resonance parameters, which were then plotted and compared visually with the data. The resonance parameters were then varied and the values giving best agreement with the data were noted. In part IV the results for each resonance are discussed in detail. The next few paragraphs consist of elementary considerations related to the expansion in partial waves of the scattering amplitude. Two often-quoted references will be referred to as JW[19] and LT[18].

The scattering amplitude for two spinless particles, scattering in their center-of-mass system, has the familiar expansion (LT, equation 1.24)

$$kf(x) = \sum_{L=0}^{\infty} (2L + 1) f_L \cdot P_L(x) . \qquad \text{(III-1)}$$

When the particles have spin, the expressions given by LT are more complex. However, JW have pointed out that in the so-called helicity representation, the expression analogous to (III-1) is again simple, namely,

$$kf^{ji}(E, x) = \sum_{J} (2J + 1) f_J^{ji}(E) d_J^{ji}(x) , \qquad \text{(III-2)}$$

where, j, i = spin projection along the direction of motion (helicity), in the final and initial states, respectively,

$d_J^{ji}(x)$ = rotation operator (also the wave-function for a symmetrical top), and

$f_J^{ji}(E)$ = scattering amplitude in the state J, at energy E, with initial and final helicities i and j.

If we have many channels, (III-2) is similar again but has channel indices (c, c') attached to f_J.

Now, the number of J values contributing to (III-2), at a given energy, is limited by the centrifugal and Coulomb barriers. The number of independent amplitudes for each J value is limited by the number of channels, the spins in each of them, unitarity and time reversal invariance. We first find the number of amplitudes for each J value $\geq 3/2$.

The two channels of interest are:

$$\begin{aligned} c &= E \leftrightarrow Li^7(S = 3/2^-) + \alpha(S = 0^+) , \\ c' &= I \leftrightarrow Li^{7*}(.48)(S = 1/2^-) + \alpha'(S = 0^+) , \end{aligned} \qquad \text{(III-3)}$$

for $E_{\alpha L} < 4.46$ MeV, the $B^{10} + n$ threshold. For each J value $\geq 3/2$ we have the set of states $|i, c\rangle$:

$$|3/2, E\rangle , \ |1/2, E\rangle , \ |-1/2, E\rangle , \ |-3/2, E\rangle , \ |1/2, I\rangle , \ |-1/2, I\rangle , \qquad \text{(III-4)}$$

where $i = \underset{\sim}{\sigma} \cdot \underset{\sim}{p} / |p|$ = spin projection along the direction of motion (not along the z axis, as is usually done). The scattering amplitude

matrix $\langle j, c' | F^J | i, c \rangle$ is then a 6 x 6 matrix of complex energy-dependent functions (not all independent). JW further show that under time reversal, this matrix is transposed; therefore, it must be symmetric to be invariant. JW also show that a state $|J, i, c\rangle$ transforms under parity according to

$$P|J, i, c\rangle = -(-1)^{J-S_c} |J, -i, c\rangle \quad , \tag{III-5}$$

where $S_E = 3/2$, $S_I = 1/2$ in our case. Using (III-5) we may define a new basis for the states (III-4) as $|\pi, |i|, c\rangle$:

$$|+, |3/2|, E\rangle, \ |+, |1/2|, E\rangle, \ |-, |1/2|, E\rangle, \ |-, |3/2|, E\rangle,$$

$$|+, |1/2|, I\rangle, \ |-, |1/2|, I\rangle \ . \tag{III-6}$$

Since $\underset{\approx}{F}^{J, \pi}$ conserves parity, it breaks up into two 3 x 3 matrices in the basis (III-6). The unitary S matrix $\underset{\approx}{S}^{J, \pi}$ is related to $\underset{\approx}{F}^{J, \pi}$ by

$$\underset{\approx}{F}^{J, \pi} = (\underset{\approx}{S}^{J, \pi} - \underset{\approx}{I})/2i \ . \tag{III-7}$$

It is easy to see that if we define

$$\underset{\approx}{S} = (\underset{\approx}{I} - i\underset{\approx}{K})^{-1} (\underset{\approx}{I} + i\underset{\approx}{K}) \quad . \tag{III-8}$$

where $\underset{\approx}{K}$ is a real, symmetric 3 x 3 matrix, then $\underset{\approx}{S}$ is unitary and $\underset{\approx}{F}$ is symmetric. Thus, we conclude that six independent real functions of energy are necessary to completely describe our reaction, for each $J \geq 3/2, \pi$, below the B^{10} + n threshold.

The next important question is to find the effect of the barriers, in order to determine the number of contributing J values. Although the helicity representation is very convenient for formal considerations, it turns out that the Coulomb amplitude is not diagonal in that basis (since it is diagonal in the basis which diagonalizes the spin projection along the z axis). An alternate set of complete channel labels is $|J, M, L, c\rangle$ (the familiar J, M representation). Since M is conserved during scattering, we may neglect that index in the labelling. The matrix element between the two bases is given by JW as

$$\langle J, L, S | J, \lambda \rangle_c = \left[\frac{2L+1}{2J+1}\right]^{1/2} C(L, S_c, J; 0, \lambda) \, . \qquad \text{(III-9)}$$

Table I shows these matrix elements, corrected for parity, for $1/2 \leq J \leq 9/2$. We have found it convenient, throughout this work, to refer to nuclear properties in the $|J, \pi, |\lambda|, c\rangle$ basis, then to see what actually comes out by referring to Table I to find what L values were involved. We wish to point out some particular features of the matrix elements given in Table I. Let us assume that the $J = 3/2^-$ channel were resonating. Such a state could decay in the channels $| \, |\lambda|, c\rangle = | \, |1/2|, E\rangle$, $| \, |1/2|, I\rangle$, $| \, |3/2|, E\rangle$. Each of these in turn consists of a definite mixture of L values, so that in the limit where $|\lambda|$ is a good quantum number, a strong effective spin-orbit force must be present to account for the mixture. Although $|\lambda|$ is known to be a good quantum number in molecular-beam scattering experiments[20], involving semi-classical rotators, it is not known

whether the same result should hold for nuclei. It is unfortunate that in the cases studied here, we were not able to decide the question, because of the very strong L dependence of the penetration factors. Figure 15 shows a graph of the penetration factors for L = 0-6, using a nuclear radius of 6.0 fermis. In part IV we shall discuss the reasons for this unusually large radius.

We have developed enough formalism, at this point, to see what would be involved in an attempt to unfold the data directly, using a truncated partial wave expansion. The simplest approach is to fit the data with a linear least-squares expansion of the cross section. This then neglects unitarity. We have attempted such a fit, with no success whatsoever. The linear fit is highly unstable, in a curious fashion: using a six-parameter fit on an angular distribution consisting of 30 angles, we obtained values of χ^2 of order 6-10, which is quite reasonable, but the values of the determined parameters were of order 10^5, whereas they should have been of order unity. This type of linear instability was discussed in detail by Overley in his thesis; we find the same effect here.

A more sophisticated approach is the use of non-linear least-squares fitting routines. We may estimate the number of independent amplitudes that should be included in truncated expansion, at $E_{\alpha L} = 4.0$ MeV. After consulting Figure 15 we conclude that an L = 4 resonance has a maximum width of about 700 keV. If we include partial waves up to L = 4, Table I tells us that 46 independent amplitudes contribute to the expansion. Our data is not precise enough to determine that many numbers, not to mention the multiple solutions that certainly exist, due to the many possible roots of non-linear equations. Even if helicity is assumed to be a conserved quantum number, 23 amplitudes still survive.

Thus, we see that a model program is mandatory, and the method outlined above, in the second paragraph of this section, is the preferred choice. The detailed equations for a single resonance in the presence of a Coulomb field and a potential background are given in Appendix I, along with a definition of units. The results contained in Appendix I were found essential in the process of debugging the more complex many-level model-program described in Appendix II. The reader is urged to peruse Appendices I and II now, since the model-program will, from now on, be our main tool.

We have made a list of all the scattering anomalies observable by visual inspection of the measured yield curves (Figures 11, 12 and 16). This list is presented in Table III. Six anomalies are visible below $E_{\alpha L} = 4.38$ MeV, so we expect that at least a six-level model will be necessary to explain the observed cross section. As pointed out in Appendix II, each level can be specified by the following five parameters; $E_r, J^{\pi}, \Gamma_T, \Gamma_I/\Gamma_E$, $\varphi = \tan^{-1}\frac{\gamma_{L+2}}{\gamma_L}$. Given $\Gamma_T, \frac{\Gamma_I}{\Gamma_E}, \varphi$, the reduced widths $\gamma_{3/2,E}$, $\gamma_{1/2,E}$, $\gamma_{1/2,I}$ are easily calculated (this is done by the model-program as shown in Table IV). In addition, the potential radius must be specified. As a starting point, a one-level fit was attempted in the region of the 10.60 MeV resonance (level 4 in Table III), since its width is small (see Figure 12). Mainly because of the strong $L = 3$ interference effect visible in Figure 18, $J^{\pi} = 7/2^+$ soon appeared as the best choice. The potential and penetration radii, however, had to be given different values. We selected

$$R_{pot.} = 3.8 \text{ fermis} ,$$

$$R_{pen.} = 6.0 \text{ fermis} .$$

These choices for the radii will be discussed in detail in part IV. A second level was added and its parameters adjusted to produce the best results. Then the parameters of both levels were varied to see if the addition of a new level might allow new possibilities. The point of diminishing returns was reached with a 7-level model whose parameters are given in Table IV. The level at E = 2.90 is heavily shifted and actually resonates at $E_{\alpha L} \cong 3.6$ MeV; it corresponds to level 5 of Table III. The level at $E_{C.M.} = 2.5$ MeV only supplies background. The other five levels are levels 1, 2, 3, 4, 6, of Table III. In this manner, the first six levels of Table III were accounted for. Including debugging time, Table IV represents about three hours of 7094 time. The computer run from which Table IV and Figures 21-23 were obtained, took three minutes of that time. We next present a detailed discussion of the results contained in Table IV and discuss some alternatives.

IV. RESULTS

We divide this section into two parts. Part A contains a rather detailed discussion of the spin assignments for the six anomalies visible below the B^{10} + n threshold. Part B deals with the few results that can be obtained above that threshold and up to 16.31 MeV excitation, the highest energy at which data were obtained.

A. Spins and Parities of Levels Between 9.88 and 11.46 MeV Exc.

The six levels occur at excitation energies 9.88, 10.26, 10.32, 10.60, 11.0, and 11.27. We discuss them in order of increasing excitation energy.

1. The 9.88 MeV Level

Our best fit to this level, using the model-program, is $J^{\pi} = 3/2^{+}$. We shall now present arguments to explain why this is a preferred value. The resonant elastic cross section, at resonance, is $\alpha \frac{\Gamma_E^2(2J+1)}{\Gamma_T^2}$, while the inelastic one goes like $\Gamma_E\Gamma_I(2J+1)/\Gamma_T$. From Figure 3, showing the total inelastic cross section, we may write

$$\frac{k^2 \cdot \sigma_I}{4\pi} = \frac{2J+1}{2S+1} \cdot \frac{\Gamma_E\Gamma_I}{\Gamma_T^2} \simeq .16 , \qquad \text{(IV-1)}$$

yielding

$$x(1 - x)(2J + 1) = .64 , \qquad \text{(IV-2)}$$

where $x = \Gamma_E/\Gamma_T$, $S = 3/2$. This quadratic equation in x has the following solutions

J	1/2	3/2	5/2	7/2	9/2
x_1	.50 + .26i	.20	.12	.09	.07
x_2	.50 - .26i	.80	.88	.91	.93

(IV-3)

It is to be expected, and we have checked numerically, that, if we use the second solution, the elastic cross section will show the resonance quite strongly. Now it is characteristic of the data (Figures 11, 16-20), that this level has a very weak effect in the elastic channel. For this reason the fits using the second solution were poor and were discarded. Since $x_2 = 1 - x_1 = \Gamma_I/\Gamma_T$, the table (IV-3) also prescribes Γ_I/Γ_T, for the selected solution.

We have then found numerically and this can be inferred from appendix I, that $J = 1/2^{\pm}$, $x_1 = 0.5$, gave a sizeable elastic interference at 159° and somewhat too small a total inelastic cross section. For this reason, these assignments seem less likely than $3/2^{+}$ (table III). Next we consider the penetration factor. We have

$$\Gamma_I = 2P_L \gamma_{LI}^2 , \quad \text{and} , \qquad \text{(IV-4)}$$

$$\gamma_{LI}^2 = \frac{\hbar^2}{MR^2} \theta_{LI}^2 \cong .451 \, \theta_{LI}^2 , \qquad \text{(IV-5)}$$

where P_L is the penetration factor plotted in Figure 15, for the L values shown in Table I and R_o = 6 fermis. γ_{LI}^2 is the so-called reduced width and θ_{LI}^2 the dimensionless reduced width which would be 1 for a square well. Taking Γ_T = 0.15 $MeV_{C.M.}$ from Table IV, we make a list of the values of θ^2 for the remaining J^π,

J^π	$3/2^+$	$3/2^-$	$5/2^+$	$5/2^-$	$7/2^+$	$7/2^-$	$9/2^+$	$9/2^-$
θ_I^2	1.5	6.5	66.	6.5	66.	>100.	>100.	>100.

(IV-6)

On the basis of (IV-6), in order not to have too large a value of θ^2, our choice is narrowed down to $J^\pi = 3/2^+$. It might be argued that if most of the wave function for that level were concentrated near the nuclear surface, the Wigner limit (θ^2 = 1.5) might be exceeded. But, if we take into account the energy derivative of the level shift, we find that the observed width Γ_T^o of a resonance is bounded from above by the inequality

$$\Gamma_T^o \leq \left. \frac{2P_c}{\frac{dS_c}{dE}} \right|_{E = E_R,\ r = r_c} , \qquad \text{(IV-7)}$$

where P_c is the penetration factor in the channel 'c' for which $\theta_c^2 \to \infty$, and $\frac{dS_c}{dE}$ is the energy derivative of the shift function, evaluated at E_R and $r = r_c$. In this case $\frac{dS_c}{dE}$ was found large enough to give all the assignments of (IV-6), except $3/2^+$, a value of $\Gamma_T^o \leq .075$ MeV. Indeed, it was in the process of fitting this resonance that we were forced to increase the radius for penetration, from the usually

accepted value[4] of 3.8-4.8 fermis, to the value 6 fermis used here. It was found very difficult to maintain Γ_I/Γ_T and Γ_T^o simultaneously, when using a small radius, even when the Wigner limit was very badly exceeded, due to the effect mentioned above. Figures 21-23 show the computed cross section near that resonance ($E_{\alpha C.M.}$ = 1.209 MeV) and should be compared with Figures 3, 16 and 11. The agreement is qualitatively excellent and quantitatively fair.

We have also found that the potential phase shifts resulting from a radius of 6 fermis produced too large a background cross section. Thus, we used a different radius to compute them. The value used in Figures 21-23 was 3.6 fermis. This procedure may be justified on physical grounds, following some calculations made by Vogt[22]. Vogt has shown that using a Saxon-Woods potential having a surface thickness of 1 fermi, the penetration factor was effectively increased by a factor of nearly 8, over the value predicted when using a square well with the same average radius. However, the non-resonant phase shifts for a Woods-Saxon potential having an average radius R_o and a square well with radius R_o are similar. We shall return later to the question of background scattering, in connection with possible direct interaction effects.

2. The 10.26 and 10.32 MeV Levels

We consider these two anomalies together because Γ/D, the ratio of the width to the separation is of order unity. The C.M. energies where these anomalies appear are E_α = 1.59 and 1.656 MeV. The laboratory energies are 2.50 and 2.60 MeV. In Figure 3, showing the γ-ray yield, only one anomaly is visible at 2.50 MeV. In

Figure 11, showing the elastic 90° C. M. yield, only one anomaly is visible again, but this time around 2.65 MeV. Figure 16, showing the 159° elastic cross section, reveals a well-developed low-energy asymmetry for the 10.32 MeV level. Since it was easy to reproduce this asymmetry numerically, using two levels (see Table IV and Figures 21-23), we believe there is little doubt about the presence of two levels close together in energy. The 10.32 MeV level was first observed, rather weakly, in the reaction $B^{10}(d, p)B^{11}$ by Elkins[23], with a total width of 54 ± 17 keV in the C. M. system. This is not inconsistent with the yield curve Figure 11. Figures 21-23 show the model-program prediction for a level at $E_{C.M.} = 1.59$ MeV, with $J = 3/2^{-}$, $\Gamma_{TC.M.} = 200$ keV, and another one at $E_{C.M.} = 1.656$ MeV, with $J = 5/2^{-}$, $\Gamma_{TC.M.} = 100$ keV, at $\theta_{C.M.} = 159^{\circ}$. This prediction is in good qualitative agreement with the data (Figure 16).

From Figure 11, we see that the elastic yield at 90° has a very strong anomaly. This anomaly presumably comes from one of the two levels presently under consideration. The 90° yield, for a negative orbital-parity resonance, does not interfere with anything and only receives contributions from the square of the resonant amplitude; this squared term may be non-zero since the particles involved have spin. We have tried, on the computer, all values of J from $1/2^{+}$ to $9/2^{+}$, and found that none of them gave yield curves similar to that of Figure 11. The discrepancy is, in this case, two-fold: first, the positive parity levels give symmetrical line shapes (no interference) and second, the calculated scattering anomalies are always too small, even with large values for J. For this reason we believe that one of the two states has negative parity (most probably the 10.32). Such a state will interfere with the background at 90°. Unfortunately, it turns out that the phase of the Coulomb

amplitude gives a negative interference term for all the values of J considered ($\leq 9/2$). This implies that the potential phase shift is large. For a reasonable value of the potential radius (3.8-5 fermis), however, we get only a slight improvement (the interference term is too small but is at least positive), so that we can not get the large effect shown in Figure 11. Indeed, we were not able to find any background, due to any number of resonances, which would give correct yield curves both at 90^{o} and 159^{o}. One of our best results is given in Figures 22 and 23. It may be argued that a broad level (say $3/2^{-}$) with the proper mixture of L = 0, 2 might give an interference at 90^{o} while not being visible at backward angles. This possibility was investigated numerically. No resonant background was found suitable, essentially because the interference of the resonant background with the Coulomb amplitude was always negative and tended to cancel the positive interference with the 1.656 MeV state.

There remain two alternatives: either we select a different potential radius for each L value or we introduce a non-resonant background in the R-matrix itself. An earlier version of the model-program attempted to take into account the elastic background due to a square well of fixed depth. It was found that the effect of the square well was very sensitive to the depth and radius selected, since, in this case, a square well may produce sharp resonances ($\Gamma \leq 300$ keV), because of the Coulomb barrier. Also, equation IX-1.3 of LT

$$\frac{1}{L'} = \frac{1}{L^{o}} - R^{o} , \qquad \text{(IV-8)}$$

indicates that a new penetration factor P' = Im L' must be chosen when the background R^O is present. As an example, if we consider only the R^O due to the finite Coulomb repulsion inside the nucleus, we find that P' actually has some zeros for certain values of the energy, thus completely excluding any observable resonances there. Our conclusion was that an R^O term could only be included if one were doing a straight inversion of the data with few partial waves. We have not attempted to use separate potential radii for each L value, because it is then difficult to maintain a smooth angular dependence for the background cross section. We will discuss how this lack of background knowledge influences our fit.

Assuming for the time being that the 1.656 MeV level has $J^{\pi} = 5/2^-$, we look at the 1.59 MeV state. To study the possibilities here, we repeat the steps (IV-1)-(IV-3), using this time $\left.\frac{k^2\sigma_I}{4\pi}\right|_{res} \cong .065$, obtained from Figure 3. The quadratic for x(IV-2) now has the solutions

J	1/2	3/2	5/2	7/2	9/2	
x_1	.135	.070	.042	.034	.027	(IV-9)
x_2	.845	.930	.958	.966	.973	

The first solution is unsuitable because it produces only a very small effect in the elastic channel, and it was therefore discarded. It turns out that using $J = 3/2^{\pm}$, the asymmetry at 159^O can be reproduced quite well (compare Figures 22 and 16). The fit is rather insensitive to parity. If we take $J \geq 5/2$, the asymmetry comes out too large, if we take $J = 1/2$ it comes out somewhat too small. Because of our

failure to reproduce the 90^{o} yield around this doublet, caution must be exercised in putting limits on the spin of this level. Thus a conservative estimate is $1/2 \leq J \leq 5/2$ (parity unknown), with $3/2^{-}$ as our best fit.

Using this value for the 1.59 MeV level, we have found that $J = 5/2^{-}, 7/2^{-}$ were equally likely for the 1.656 MeV state, $1/2^{-}$ and $3/2^{-}$ being excluded because they gave too small a yield at 159^{o}, $9/2^{-}$ being excluded, because it gives too small a barrier penetration.

3. The 10.60 MeV Level

After the target thickness corrections, we find the resonance energy to be $E_{\alpha L} = 3.032 \pm .01$ MeV and the width to be $\Gamma_{T\,lab} = 100 \pm 10$ keV. In the C. M. system these values are respectively 1.93 and .070 MeV. Our value for the excitation energy in B^{11} is in good agreement with the recent measurement of Groce et al.[24] ($E_{exc.} = 10.594 \pm 0.012$ MeV).

From the elastic angular distributions given in Figures 17-20, it is not difficult to see that an elastic yield curve, at $\theta_{C.M.} = 140.8^{o}$, shows no sign of the resonance. This angle is a zero of $P_3(\cos\theta)$. This means that, in the elastic channel, the observed flux is almost entirely due to a L = 3 resonating amplitude interfering with the non-resonant amplitude. An obvious explanation for this is to have a strongly inelastic resonance with $J^{\pi} = 7/2^{+}, 9/2^{+}$ (see Table I). Because $J^{\pi} = 9/2^{+}$ decays with L = 5 in the inelastic channel, we may exclude it, since the penetration factor is too small (Figure 15). The model-program results for $J^{\pi} = 7/2^{+}$, $\Gamma_{TC.M.} = 75\ keV_{C.M.}$, $\Gamma_{E} = 37.5\ keV_{C.M.}$, $E_{rC.M.} = 1.94$ MeV can be seen in Figures 21-23. The agreement with the data is good.

The yield in the elastic channel is rather sensitive to the type of background used, and to the value of Γ_E/Γ_T. Some backgrounds were used, for which $\Gamma_E/\Gamma_T = .3$ gave a reasonable value of the 159^o cross section. For these backgrounds the resonant yield at 140.8^o was small. For the model given in Table IV, the angle where the zero resonant yield occurs is shifted slightly, but the general behaviour of the computed elastic and inelastic angular distributions (not shown here) is in good agreement with the data (at these higher energies the inelastic angular distributions could be measured more reliably). The models built on $J^\pi = 3/2^+$, $5/2^+$ would offer no explanation for the strong F-wave elastic interference since they can decay via P-wave in the elastic channel. Furthermore, $J^\pi = 3/2^+$ yields a total inelastic cross section which is too small by about a factor of two, while $5/2^+$ fails in the same respect by about 25%. Thus, $7/2^+$ is preferred and $5/2^+$ is, a possible, though unlikely alternative.

4. The 11.0 MeV Anomaly

The only evidence we have for the existence of a state at this energy is a broad maximum in the total inelastic cross section (Figure 3), around $E_{\alpha L} = 3.6$ MeV. Since this cross section remains rather high, up to 5 MeV, it is quite possible that many broad levels are overlapping in that region. For this reason, our fit to this anomaly only indicates that this anomaly may be a state.

We have found that the non-resonant total inelastic cross section up to $E_{\alpha L} = 3.2$ MeV could be fitted rather well, assuming a large P and D-wave inelastic amplitude (the S-wave inelastic amplitude is D-wave in the elastic channel, and would be expected

to rise more slowly with increasing bombarding energy than the P-wave inelastic amplitude, which is also P-wave in the elastic channel). A broad state with $J^{\pi} = 1/2^{+}$, $\Gamma_T = 4.0$ $MeV_{C.M.}$, $\Gamma_E/\Gamma_I = 1$, was located at $E_{\alpha C.M.} = 2.5$ MeV to saturate the inelastic P-wave channel. With $\Gamma_T = 4.0$ MeV, it also served the purpose of maintaining the total inelastic yield at higher energy.

We then looked for a spin and parity assignment, to superimpose on the broad $1/2^{+}$ level, which would fit the elastic 159^{o} and $90^{o}_{C.M.}$ yields, while providing the correct total inelastic cross section. The only levels having a D-wave inelastic amplitude are $3/2^{-}$ and $5/2^{-}$. Of these, $5/2^{-}$ seemed to give a somewhat better overall fit to the elastic yield curves and angular distributions and to the 11.27 MeV state which we will discuss next. It was selected for presentation here for this reason. Because of our selection for the boundary condition at the nuclear surface, which was chosen for the 1.656-MeV level, the $5/2^{-}$ level is heavily shifted, from $E_{\lambda C.M.} = 2.90$ MeV in Table IV to $E_{rC.M.} \cong 2.15$ MeV in Figure 21.

5. The 11.27 MeV State

This state was first identified by Groce et al.[24] at $E_{exc.} = 11.266 \pm .007$ MeV. Since it has a negligible inelastic width (Figure 3), it has escaped detection in previous work on the inelastic scattering.

The elastic yield curve at $159^{o}_{C.M.}$ (Figure 16) shows a large peak at about 4.1 MeV_{Lab} = 2.61 $MeV_{C.M.}$. We thus expect to find a large value for the spin of that level. The elastic yield shows only a small symmetrical bump at $\theta_{C.M.} = 90^{o}$ (Figure 11),

indicative of a positive parity level (no interference at $\theta_{C.M.} = 90^{o}$). Many choices for spin and parity were tested with the model-program. Models with $J \leq 3/2$ could not reproduce the large 159^{o} cross section, and were rejected. Models with $J^{\pi} = 5/2^{-}$, $7/2^{-}$, or $9/2^{-}$ showed rather pronounced 90^{o} interference and were also rejected. The three remaining possibilities, in order of decreasing goodness-of-fit, were $J^{\pi} = 7/2^{+}$, $9/2^{+}$ and $5/2^{+}$. The assignment $5/2^{+}$ suffers from two diseases: its 159^{o} cross section is too small, and if it has any P-wave component, the line shape is incorrect at 159^{o} (a dip on the low energy side). The two remaining choices, $7/2^{+}$ and $9/2^{+}$, seem equally promising, the $7/2^{+}$ giving somewhat too small a cross section and the $9/2^{+}$ producing the opposite effect. However, the background due to the 11.0 MeV anomaly can be adjusted in both cases to give good fits. Each of the two possibilities has a special appeal. A level with $J^{\pi} = 7/2^{+}$ at 11.28 MeV excitation energy could supply S-wave flux into the opening neutron channel at 11.46 MeV. A threshold cusp might then be seen there[25] which would explain the scattering anomaly, which occurs at precisely that energy (see Figures 3 and 12). On the other hand, a level with $J^{\pi} = 9/2^{+}$ has an $L = 5$ decay in the inelastic channel. Thus, we would have an obvious explanation for the lack of inelastic yield for that level, since the penetration factor would then be very small.

B. The Scattering Anomalies from 11.46 to 16.31 MeV

We have pointed out earlier that the opening of several new channels, near 11.4 MeV exc. in B^{11} (see Figure 1), makes our model-program inadequate above this energy, since it is a two-

channel model. However, for the sake of completeness, we now summarize qualitatively whatever can be concluded about this energy region without performing detailed numerical calculations.

We have made a list of all the bumps and kinks that can be seen in Figures 11 and 12, which show the elastic and inelastic yield at $\theta_{\alpha L} = 60^{o}$ vs the laboratory bombarding energy. This list is presented in Table III, along with the approximate width of these anomalies and some comments. Thirteen "objects" are seen in the energy range under present consideration. It is probable that they do not all represent states of B^{11}. For example, the anomalies numbered 7, 11, 14, 15, 18, all coincide, within their width, with the thresholds for forming the first five excited states of B^{10} plus a neutron. Since tests exist[25], within R-matrix theory, to determine the effects of S-wave neutrons thresholds, which effects are sometimes known to be large[26], it might be prudent to investigate this point before building nuclear models involving these anomalies. We spend the next paragraph discussing the general features of the observed cross section, before going into a detailed discussion of the thirteen observed anomalies.

The behaviour of the cross section is rather puzzling in this many-channel region, apart from apparent threshold effects. The elastic cross section shows strong backward peaking (Figures 17-20) while the inelastic angular distributions (Figure 14) seems to have diffraction-type maxima and minima, whose positions have a smooth energy dependence. We may speculate that this behaviour is due to the presence of a large direct interaction amplitude. We have investigated numerically some simple models for this effect. If one considers Li^{7} to look somewhat like an alpha particle bound to a triton, one can show rather simply that triton exchange effects tend

to uncouple the even and odd L amplitudes. This effect can be represented in a naive way using a "direct" and an "exchange" potential. When one considers only the cross section due to the "hard sphere" phase shift, its angular dependence is no longer monotonic. For example, if $V_{ex.} = -V_d$, the potential vanishes for even L values and the background cross section acquires a strong backward peak! We do not present here any details of these calculations because they are not quantitatively relevant due to their oversimplification of the problem. The inelastic scattering might also be understood as an exchange mechanism, if we do not assume that the exchanged triton is captured in the ground state of the triton-alpha system. However, there is another source of inelastic scattering which could also be important; it is a transition from the ground state to the first excited state of Li^7 via the BE(2) matrix element, which is known to be near the collective limit[27, 28] ($BE(2) \cong 7.3 \pm .15\ e^2f^4$). We have calculated the total Coulomb excitation cross section[29] at $E_{\alpha L} = 2.0$ MeV, that is, .56 MeV below the Coulomb barrier for R = 5 fermis. We find

$$\left.\frac{k^2 \cdot \sigma_t}{4\pi}\right|_{\text{Coul. exc.}} \cong 4 \times 10^{-3}. \qquad \text{(IV-10)}$$

This is too small to have an appreciable effect, but, this is only the contribution of the Coulomb force. There is, in principle, no objection to using the nuclear force to make the transition. Since the potential strength squared occurs in (IV-10), it is not unrealistic to expect a factor of 100 or more in enhancement of the cross section as we go over the Coulomb barrier. This would then give the BE(2)

excitation cross section a value comparable to the one actually observed. The energy dependence, at a fixed angle, of a direct interaction cross section may exhibit broad maxima and minima. If the direct amplitude is allowed to interfere with a few narrow resonances, the resulting (total or differential) inelastic cross section may show bumps that are displaced in energy from the resonance position. For this reason, the level identification may be unreliable. This should be kept in mind in the next few paragraphs where we discuss our thirteen anomalies.

We begin with anomalies number 7 and 8 (Table III) at 11.46 and 11.60 MeV exc. In Figure 11 (90^{o} elastic) they are not resolved, and all we see is a small bump at about 11.5 MeV exc. and a small dip about 100 keV higher. If this dip is an interference effect, then one of the two levels should be of negative parity. In Figure 12 (92^{o} inelastic), they are again unresolved and only a large peak can be seen around 11.5 MeV. In Figure 3 (total inelastic), they are barely resolved. If they represent one level which has an S-wave neutron width, then this level should be $5/2^{+}$ or $7/2^{+}$ and it is expected to produce a threshold cusp. This is not unattractive in view of the similarities between the yields here and those near the 10.60 ($7/2^{+}$) and the 11.27 ($7/2^{+}$, $9/2^{+}$). This object would further have to be identified with the bump seen at 11.68 MeV exc. in the reaction $Li^{7}(\alpha, n)B^{11}$ [30]. The highly speculative nature of this assignment is indicated by a double bracket in Table III.

Anomaly number 9 in the list is well resolved in all our data. In Figure 11, however, it appears as a definite dip in the 90^{o} elastic cross section. From this we may infer that this level has negative parity.

Next we consider items 10 and 11. Level 10 is included in order to account for the broad maximum in the elastic cross section in the region 5 MeV $\leq E_{\alpha L} \leq$ 6 MeV. Item 11 represents only a small dip in the elastic cross section above the threshold for $B^{10*}(1^+, .717) + n$.

Level number 12 at 12.55 MeV exc. is well resolved in the inelastic channel, but it appears highly unsymmetrically in the elastic scattering. If this is an interference effect, then this level must be of negative parity.

Items 13 and 14 are again considered together. Level 13 appears to be about 300 keV wide, but its proximity to a neutron threshold could distort it considerably. Since it only shows up as a dip in the elastic cross section, it should also have negative parity. Item 14 is a kink in the elastic cross section at 13.20 MeV. It was also seen as a strong peak in the plot of χ^2 vs energy for a sixth order Legendre polynomial fit to the inelastic cross section (this fit is not presented here for reasons mentioned previously).

Items 15 and 16 are unresolved in Figure 12 (inelastic 92^o), and only a dip is observed in Figure 11 (elastic 90^o) at 14.0 MeV exc. Does this mean again negative parity for item 16?

Anomaly number 17 might be close enough to the threshold $B^{10*}(2^+, .36) + n$ at 15.04 MeV exc. (item 18), to be distorted; if this were the case these two anomalies might be produced by having one broad level suffering from threshold distortion. If, on the other hand, threshold distortion does not take place, then items 17 and 18 should be considered as separate levels.

Finally, item 19 represents a small peak in the 92^o inelastic yield at about 15.73 MeV exc. It does not show up in Figure 11. A resonance at this energy has also been seen in the reaction $Li^7(\alpha, n)$[30].

It is probable that detailed angular distributions of the reactions $Li^7(\alpha, \alpha)Li^7$ and $Li^7(\alpha, \alpha')Li^{7*}$ (.48) could yield more detailed information about the level structure of B^{11} in this energy region, using techniques similar to the ones we have used in section A of this part of the thesis, if the question of threshold effects could be settled properly. Such a study would also require much better information on the reaction $Li^7(\alpha, n)B^{10*}$ than is presently available.

V. COMPARISON WITH NUCLEAR MODELS

We have seen in part IV that, as a result of the present experiment, we have some new information about the level structure of B^{11} in the excitation energy region from 9.88 to 11.27 MeV. In part A of this section, we compare our results with those that have been obtained for the mirror nucleus C^{11}. In part B, we seek to understand the experimental evidence about the level structure for the A = 11 system, in terms of the shell model[31] and the unified model[8] of the nucleus.

A. Comparison of the Levels of B^{11} and C^{11}

As we have seen earlier, the level structure of B^{11} appears rather complex above 11.46 MeV exc., the energy of the first threshold for neutron decay. Since it is not known, at the present time, to what extent these neutron-decay channels can distort the various observed particle spectra, we will limit our comparison to excitation energies below 11.46 MeV. Another reason for this limitation is that little information is available about the levels of C^{11}, above 10.89 MeV exc.

Figure 25 shows a scale diagram for the energy levels of B^{11} and C^{11}. The lower energy part of this figure is adapted from Olness et al.[32]. The level sequence starting at 9.28 MeV exc. in C^{11} is adapted from Overley and Whaling[10]. The levels in B^{11}, above 9.28 MeV exc. were discussed earlier in this work and the identification of the analogues of these states in C^{11} will be discussed presently.

Thirteen states in B^{11} are reported between 6.81 and 11.23 MeV exc. As an empirical rule for finding analogue states, we subtract .52 MeV from all these energies and look for nearby states of C^{11}, having approximately the resulting energies. This yields the following list:

$E_{exc.}(B^{11})$	$E_{exc.}(B^{11})$ - .52 MeV	$E_{exc.}(C^{11})$	ΔE	
6.81	6.29	6.35	0.06	
7.30	6.78	6.90	0.12	
7.99	7.47	7.50	0.03	
8.57	8.05	8.10	0.05	
8.92	8.40	8.43	0.03	
9.19	8.67	8.66	-0.01	
9.28	8.76	8.70	-0.06	(V-1)
9.88	9.36	9.28	-0.08	
10.26	9.74	9.74	0.0	
10.32	9.80	-	-	
10.60	10.09	10.08	-0.01	
11.0	10.48	-	-	
11.27	10.75	10.69	-0.06	

Beginning with the 9.87 MeV level in B^{11}, we associate with it a level a 9.28 MeV exc. in C^{11}, reported once by Cerineo[33], but not seen by Overley in the elastic scattering of protons by B^{10}. Our present assignment for this level would then be $3/2^+$, which would imply a D-wave decay for it, in the channel B^{10} + p, at about 600 keV. Since this level should have a large width in the channel Be^7 + α, it would not have been seen by Overley because its Wigner limit width for decay into B^{10} + p is about 13 keV. Overley could not see states below E_p = 700 keV, which had $\Gamma_p/\Gamma_T \lesssim 0.05$.

One of the members of our doublet at 10.26 and 10.32 MeV exc. in B^{11} should be associated with the 9.74 MeV anomaly in C^{11}.

Overley has reported difficulties in fitting his observed cross section in the region of the 9.74 MeV level. The dotted line below the 10.08 MeV level in Figure 25, indicates his conjecture to explain the discrepancy. The existence of this doublet, and, if it exists, which state in C^{11} is the analogue of the other member of the doublet in B^{11}, remain uncertain.

It is gratifying that our most definite assignment, $J^{\pi} = 7/2^{+}$, for the 10.60 MeV level in B^{11}, finds its analogue in the 10.08 MeV level in C^{11}, which is also reported to be $7/2^{+}$ by Overley[10].

We find no analogue, in C^{11}, for the 11.0 MeV state in B^{11}. However, because of its large width ($\Gamma_T \cong 3$ $MeV_{C.M.}$), this level would be very difficult to identify in C^{11}, in all the experiments which have been carried out.

The 11.23 MeV level in B^{11} should be the analogue of the 10.69 MeV state in C^{11}. The spin assignments for these two levels ($9/2^{+}$ in C^{11}, $7/2^{+}$, $9/2^{+}$ in B^{11}) are consistent.

Thus, we may conclude that the level structures of the two mirror nuclei, C^{11} and B^{11}, continue to be similar, up to 11 MeV exc., in agreement with the prevailing assumption of the charge independence of the nuclear force.

B. Comparison with the Shell and the Collective Model

We have seen that the level structure of C^{11} and B^{11} are similar, within experimental uncertainty, up to $E_{exc.} \cong 11$ MeV. This gives us confidence that nuclear models assuming isotopic spin projection invariance should apply fairly well to the A = 11 system, and should reproduce the observed level structure. Indeed, one of the earliest attempts to account quantitatively for the level

scheme, by Inglis[34], showed that intermediate-coupling wave functions did predict the ground states to be $3/2^-$, rather ambiguously.

Kurath[31] and more recently Boiarkina[35] have computed exhaustive level sequences for the negative parity levels in the 1-p shell, using intermediate-coupling assumptions. A typical predicted sequence is

E_{exc} MeV	0	1.9	5.2	5.7	6.9	12.2
J^π, T	$3/2^-, 1/2$	$1/2^-, 1/2$	$5/2^-, 1/2$	$7/2^-, 1/2$	$3/2^-, 1/2$	$1/2^-, 1/2$

(V-2)

The first five levels fail qualitatively to reproduce the observed sequence, in only one respect: the upper $3/2^-$ and the $7/2^-$ should be inverted. Kurath pointed out that one should expect that levels more than about 8 MeV above the lowest level with the same T can involve the 2s-1d shell, so that predictions based exclusively on the 1-p shell might be erroneous at higher excitation. This effect would possibly explain the discrepancy in the ordering of the two levels mentioned above.

To obtain negative parity levels at higher energy, one should certainly consider the excitation of a pair of nucleons to the 2s-1d shell. However, the positive parity levels, formed by exciting one nucleon to the 2s-1d shell, are predicted to lie at too high an excitation energy, as compared with experiment. The shell model, at least as applied up to the present, appears to be unable to deal with highly excited configurations. Fortunately, it was shown by Elliott[36] that the rotational model and the shell model lead to

similar predictions for low-lying states, at least in the 2s-1d shell. This raised hopes that the treatment of nuclear energy spectra within the framework of the rotational model might account better for the highly excited states, while retaining the successes of the shell model for the low-lying states. Kurath and Pičman[37] showed that Elliott's generating procedure also works successfully in the p-shell. More recently, Clegg[5] carried out detailed numerical calculations and obtained the following predicted level sequence for the ground state band of B^{11}.

E_{exc} MeV	0	2.19	4.54	4.98	6.75	13.3	17.1	(V-3)
J^{π}	$3/2^-$	$1/2^-$	$3/2^-$	$5/2^-$	$7/2^-$	$5/2^-$	$7/2^-$	

The $3/2^-$ that was too high in (V-2) is now too low; the experimental result lies in between (V-2) and (V-3)!

We have calculated the total energy for 11 particles in a deformed axially-symmetric oscillator potential, for various configurations, as a function of η, the deformation parameter of Nilsson[8]. The results are shown in Figure 24. We have used the same value of κ as Litherland et al.[38], namely $\kappa = 0.08$. For small deformation the parameter η is approximately equal to the ratio ϵ/κ, where ϵ is proportional to the deformation and κ measures the strength of the spin-orbit coupling. The strength $\hbar\mathring{\omega}_o$ of the undistorted oscillator potential was chosen to be 18.4 MeV, as calculated from Nilsson's formula

$$\hbar\mathring{\omega}_o = 41.\ A^{-1/3}\ .$$

We may note the following interesting features of this diagram:

i) The $K = 1/2^-(1^4 3^4 2^3)$ and the $K = 3/2^-(1^4 2^4 3^3)$ bands have a small energy separation for negative $\eta(\Delta E \cong 1.5$ MeV) and the $3/2^-$ band has the lower energy. This situation was the starting point of Clegg's calculation (however, his fit, given in (V-3) uses $\Delta E = .88$ MeV).

ii) A second $K = 1/2^-$ band with positive η should begin near $E_{exc.} \cong 4.0$ MeV. There is no experimental evidence for such a band at such a low excitation energy (see Figure 25).

iii) A $K = 1/2^+$ band should begin near $E_{exc.} \cong 8.0$ MeV with $\eta \cong 6.0$. From Figure 25, we presume that the 6.81 MeV level is the first member of that band.

iv) The configuration $1^4 3^4 6^3$ has not yet reached a minimum at $\eta = 10.0$, and as we shall see, we find no definite evidence for a band with such a large deformation at low energy.

v) The $1^4 3^4 2^3$ configuration seems to have two minima, one at $\eta \cong -6.0$, and the other at $\eta = +3.0$. Which value of η represents the equilibrium deformation?

Before we attempt to identify the observed highly excited states of the A = 11 system with a band generated from Figure 24, let us consider in some more detail two difficulties associated with the rotator model for light nuclei.

The first problem is that of spurious states. Physically, spurious states arise because we are using too many degrees of freedom, namely, 11 for Figure 24 and 3 more for the rotator degrees of freedom giving rise to the bands. Mathematically, the

problem is analogous to that of the spurious states in the spherically symmetric shell model, arising from translational non-invariance of the Hartree-Fock potential used in shell model theory[40]. The analogy has been exploited by Baym[41]. However, an additional difficulty arises in the case of rotational states. One knows that the C. M. coordinate is $\underset{\sim}{R} = 1/A \sum_{i=1}^{A} \underset{\sim}{r}_i$, to which there corresponds $\underset{\sim}{P} = 1/A \sum_{i=1}^{A} \underset{\sim}{p}_i$. Given a wave function $\psi_k(\underset{\sim}{r}_i)$, one can perform a linear transformation

$$\underset{\sim}{r}_i \rightarrow \underset{\sim}{R} \quad \text{and} \quad \underset{\sim}{\xi}_j = \underset{\sim}{r}_j - \underset{\sim}{R}, \; j = 1, \ldots 10, \; \text{for } A = 11,$$

and reexpress the wave function as $\psi_k(\underset{\sim}{R}, \underset{\sim}{\xi}_j)$. The Schroedinger equation is separable in these new variables for certain assumed potentials so that we have

$$\psi_k(\underset{\sim}{r}_i) = \Phi_k(\underset{\sim}{\xi}_j)\varphi(\underset{\sim}{R}) .$$

If $\varphi(\underset{\sim}{R})$ is not in its ground state then we know we have a spurious state. For angular momentum, the relevant coordinate whose degree of freedom must be removed is $\underset{\sim}{J} = \sum_{L=1}^{A} \underset{\sim}{j}_i$. The conjugate variables corresponding to $\underset{\sim}{J}$ are the Euler angles θ_1, θ_2, θ_3, of the whole system. The change of variables from the $\underset{\sim}{r}_i$'s to θ_λ, ξ_j is no longer linear, and Schroedinger's equation does not separate.

Baym does not give an explicit solution to the problem, so that one is reduced to investigating each case separately. We outline how

such an investigation proceeds. We suppose that we have a state g_k with a given η, in the intrinsic (body-fixed) coordinate system. A state in the space-fixed (laboratory) system is a linear combination of such states with different orientations of the body axis, but with the same value of η. Thus, the laboratory state contains the state

$$G_k = e^{i\underset{\sim}{n}\cdot\underset{\sim}{J}} g_k(\eta) \quad . \tag{V-4}$$

For an infinitesimal rotation, we have

$$G_k = (1 + i\epsilon\hat{\underset{\sim}{n}}\cdot\underset{\sim}{J})\, g_k(\eta) \quad . \tag{V-5}$$

In particular, G_k contains the state G_k^o

$$G_k^o(\hat{\underset{\sim}{n}}, \eta) = \hat{\underset{\sim}{n}}\cdot\underset{\sim}{J}\, g_k(\eta) \quad . \tag{V-6}$$

Now we consider all the states $g_k'(\eta)$ of the Nilsson diagram (say Figure 24), for that value of η, and the matrix elements

$$\langle g_k' \mid G_k^o \rangle \quad . \tag{V-7}$$

Whenever the matrix element (V-7) is near 1. for some $\hat{\underset{\sim}{n}}$ and g_k', the state g_k' must be considered redundant, since it will appear as a member of a rotational band based on g_k. Given J in the intrinsic coordinate system and the expansion of g_k in the form given by Nilsson[8], one can express (V-7) as an explicit function of $\hat{\underset{\sim}{n}}$, at which point it is possible to decide the maximum size of the matrix

element. The possibility of spurious states will be kept in mind when we proceed to seek excited bands.

The second problem we wish to discuss is that there may be lower energy configurations than those given in Figure 24, if we do not assume the potential to be spheroidal (axially symmetric), but instead consider a general ellipsoidal harmonic oscillator potential of the form

$$V = \hbar\omega_o (a^2x^2 + b^2y^2 + c^2z^2),\ a < b < c \ , \qquad \text{(V-8)}$$

where x, y, z are the coordinates of a particle. Following van Winter[42], we may define an "asymmetry" parameter

$$\chi = \frac{(2b - a - c)}{a - c},\ -1 \leq \chi \leq 1 \ . \qquad \text{(V-9)}$$

When $|\chi| \neq 1$, there exists no unit vector $\hat{\underset{\sim}{n}}$ such that $[\hat{\underset{\sim}{n}} \cdot \underset{\sim}{L}, V] = 0$. This means that K is no longer a good quantum number. However, if we take

$$\hat{\underset{\sim}{n}}_o = \left(\pm \sqrt{\frac{b^2 - a^2}{c^2 - a^2}},\ 0,\ \pm \sqrt{\frac{c^2 - b^2}{c^2 - a^2}} \right), \qquad \text{(V-10)}$$

and go to a new coordinate system $\underset{\sim}{r}'$, obtained by rotating through a fixed time-independent angle about the y axis so that $\underset{\sim}{n}_o$ points along the z' axis, we may rewrite (V-8) as

$$V = V_o + V_1,\ V_o = \hbar\omega_o(b^2(x'^2 + y'^2) + (a^2 + c^2 - b^2)z'^2)$$

$$V_1 = -2x'z'\sqrt{(b^2 - a^2)(c^2 - b^2)}\ . \qquad \text{(V-11)}$$

It is from the term V_1 (proportional to one of the quadrupole moment operators) in (V-11) that we will get band mixing. Kurath and Pičman[6] claim that for B^{11}, the effect of V_1 imitates the rotation-particle coupling term, used by Clegg in his calculation of the ground state band mixing. We notice that equation (V-11) implies simply that the effect of an ellipsoidal distortion is completely equivalent to including a quadrupole interaction, in the single particle hamiltonian, a practice often used but usually introduced ad hoc. The calculation presented in Figure 24 was done taking $\chi = +1$. From the above considerations we expect that for some other value of χ, a new and deeper minimum will occur where the ground state band will not have a double minimum, and the band mixing will be prescribed. Further numerical calculations are planned, using (V-11). Of course, the rotational energy levels for an ellipsoidal band are no longer proportional to $J(J + 1)$, but according to van Winter we have

$$E_{rot} = \alpha J(J + 1) + \beta E(\chi, J)\ , \qquad \text{(V-12)}$$

where α and β are related to the moments of inertia of the core and $E(\chi = 1, J) = 0$. The function $E(\chi, J)$ must be evaluated numerically as a root of a fifth order polynomial. Equation (V-11) has been used by Davydov and Sardaryan[43], in an approximate form, to describe odd-A heavy nuclei having rotational-vibrational spectra. It is

intuitively plausible that a P_2 (second order Legendre polynomial) vibration of the nuclear surface might make the nucleus look like a non axially symmetric rotator. Clegg points out, apparently with some astonishment, that his best calculated spectrum for B^{11} has somewhat the character of a vibrational spectrum. In the light of Davydov's result and our previous comments, this result becomes more easily understood. This second problem, then, should again be kept in mind in the next paragraphs where we discuss the excited band structure of B^{11} and comment on the general situation in the light nuclei ($A \leq 20$).

The ground state band can be fairly well represented as the mixed band resulting from the configurations $1^4 3^3 2^4$ and $1^4 3^4 2^3$, taken at $\eta = -4.0$. The next state in B^{11}, at 6.81 MeV exc. is of positive parity with $J = 1/2$ or $3/2$ (Figure 25). Since the configuration $1^4 3^4 2^2 6^1$ occurs at about 6-8 MeV above the ground state configuration, we may consider it as a candidate to generate the first excited band. We take the equilibrium deformation to be $\eta = +6.0$. Using the eigenfunctions of Nilsson for this value of η, we calculate the so-called decoupling parameter to be $a \cong 2.0$. We must next decide how many states can be formed if we remain in the 1p and 2s-1d shell. We may couple the two particles in orbit 2 ($K = 3/2^-$) to form $K = 0$ or 3. According to Elliott[36], if we put one particle in the 2s-1d shell, the only possible states have $L = 0, 1, 2$. Thus, if $K_1 = 0$, $K = 1/2$, the band has the three states: $J = 1/2, 3/2, 5/2$. Using the value $a = 2.0$, the level ordering is 1/2, 5/2, 3/2. Using $\hbar^2/2I = .344$ MeV we get the level sequence: 6.81 ($1/2^+$), 8.16 ($5/2^+$), 9.87 ($3/2^+$). The closest level to 8.16 MeV is observed at 7.99 MeV in B^{11}. However, if we assign $5/2^+$ to this

level the allowed decay of Be^{11} to the 7.99 MeV state would lead to an assignment of $J = 3/2^+$ for Be^{11}, a possibility which although unlikely cannot be completely discounted. Another possibility is to allow $K_1 = 3$ and 0 in the formation of a band. The symmetrical part of the new wave functions obtained, has $J = 7/2^+, 9/2^+, 11/2^+$. Taking $a = 2.30$ and $\hbar^2/2I = .311$ MeV we find the level sequence

E_{exc} MeV	6.81	7.80	9.76	11.23	14.74
J^π	$1/2^+$	$5/2^+$	$3/2^+$	$9/2^+$	$7/2^+$
$E_{exc}(B^{11})$obs.	6.81	7.99	9.88	11.27	14.67
J^πobs.	$(1/2, 3/2)^+$	-	$(3/2)^+$	$(7/2, 9/2)^+$	-

(V-13)

This assignment appears to be consistent with the presently available data, but it leaves open the following question: how does one account for the 7.30 MeV level in B^{11}? If it is of positive parity, its spin must then be higher than 5/2 to prevent an allowed decay from Be^{11} (assumed to be $3/2^+$). Also, whatever its spin is, a new band must begin at this energy.

We may compare the value of the moments of inertia assumed for the two bands mentioned above with the values that would obtain for a rigid body. Assuming $R_o = 1.4\ A^{1/3}$, the radius of B^{11} is then about 3.1 fermis. For a uniform spherical mass distribution we have

$$2/5\ M R_o^2 = 42.8\ f^2 \text{ a. m. u.} \quad .$$

This gives $\hbar^2/2I = 0.488$ MeV .

This formula is not very sensitive to small deformations. The values 0.311 and 0.344 MeV used above represent about 70% of the rigid body value. We may compare this with the results of Chesterfield and Spicer[27], who find that the value $\hbar^2/2I = 0.50$ MeV yields level sequences in fair agreement with experiment. The rigid body value for Li^7, calculated as above, is 1.04 MeV. The experimental value is thus about 50% of our rigid body value for Li^7. Another comparison may be made with the rotational structure of Al^{25}. Litherland et al. find that the rotational structure of Al^{25} is well reproduced using exactly the rigid body value for the moment of inertia. Our present result for B^{11} lies in between.

Still another possibility is to assign $J^\pi = 5/2^+$ to the 7.30 MeV level, and $J^\pi = 1/2^+$ to Be^{11}. However, to get the correct spacing for the 6.81, 7.30, 9.87 MeV levels, one requires a decoupling parameter $a = 3.0$, which would demand a very large value of the equilibrium deformation. The orbit $1^4 3^4 6^3$ of Figure 24 would presumably be a better candidate to generate this band. The situation appears complex and it is probable that many more states actually contribute to the band structure than those we have considered. It is to be hoped that simplifications will occur when one considers ellipsoidal deformations, since this effect will tend to lift the existing energy degeneracies for the complex axially symmetric configurations we are dealing with here.

If one studies the level scheme for the odd A light nuclei, one finds recurring evidence for low lying $1/2^+$ and $5/2^+$ states. It is possible in several cases to identify triplets with: $1/2^+$, $5/2^+$, $3/2^+$,

a decoupling parameter of order 2.0 - 4.0, and a moment of inertia in the range of a few hundred keV. Because of the experimental difficulties involved in detecting high spin states, it is difficult to reach a conclusion about the failure to detect the predicted, low-lying, $9/2^+$ states required for the band extensions in these nuclei.

To summarize the situation we must admit that applying the rotational model to the A = 11 system, especially to the highly excited states, is still in the nature of a conjecture. The tentative band structures, proposed in the preceeding paragraphs, do seem to indicate that the rotational model can account for some of the features of the highly excited states of B^{11}, but it is clear that more refined calculations are necessary to determine the exact structure of the excited bands, or indeed, to determine whether or not this model has any value in describing the A = 11 system.

APPENDIX I

The One-Level Two-Channel Resonance Formula

In the main text we have outlined briefly the structure of the scattering amplitude expansion for the present reactions. Here we present detailed expressions for the single-level expansion, using the techniques of R-matrix theory. We write the expansion in Legendre polynomials for both the elastic and inelastic channels. The numerical values of the relevant coefficients are given in Table II. First we present our definition of the Coulomb amplitude. This is necessary because different authors often use different conventions.

In the center-of-mass system for two non-identical particles of mass m, m', scattering non-relativistically, we let:

Z, Z' be their charge (positive for protons), in units of $|e|$, where, in our hybrid system of units, we take $e^2 = 1.44$ MeV-fermis,

E = the energy in the C. M. system = $\hbar^2 \cdot k^2/2\mu$, with:

$\hbar^2$ = 41.6 MeV-f^2-a. m. u.,

k = the relative wave-number in f^{-1},

μ = the reduced mass $\frac{m \cdot m'}{(m + m')}$ in a. m. u.,

ρ = $k \cdot r$ the dimensionless distance between the two particles,

r = their separation in fermis,

η_c = the dimensionless strength of the Coulomb force in channel $c = \frac{k_c}{2E_c} Z Z' e^2 = \frac{1.51}{\sqrt{E_c}}$, for the present reactions.

x = The cosine of the C. M. scattering angle.

Gordon[21] has shown that there exists a solution φ of the Schroedinger equation, for the particles interacting via the Coulomb potential, which has the properties:

a) $$\varphi \xrightarrow[\rho(1-x)\to\infty]{} [\rho(1-x)]^{i\eta} \cdot e^{i\rho x} - \eta[\rho(1-x)]^{-i\eta-1} \cdot e^{i(\rho+2\sigma_o)} . \tag{AI-1}$$

b) $$\varphi = \sum_{L=o}^{\infty} (2L+1) i^L e^{i\sigma_L} \frac{F_L(\rho)}{\rho} \cdot P_L(x) . \tag{AI-2}$$

c) F_L is regular at the origin and has the asymptotic expansion

$$F_L(\rho) \xrightarrow[\rho\to\infty]{} \sin(\rho - \eta\log 2\rho - \frac{L\pi}{2} + \sigma_L) . \tag{AI-3}$$

$$\sigma_o = \arg \Gamma(1 + i\eta) . \tag{AI-4}$$

$$\sigma_L = \sigma_o + \sum_{n=1}^{L} \tan^{-1}\frac{\eta}{n} = \sigma_o + \omega_L, \quad L \geq 1 . \tag{AI-5}$$

These definitions agree with those currently in use in this laboratory for numerical calculations, and with the conventions of Lane and Thomas[18]. There are, of course, many ways of defining the Coulomb wave-functions but all three properties a), b), c) must be given self-consistently. Using the choice of phases which is standard here, we write the scattering amplitude and cross section as

$$k^2\sigma = |f_r|^2, \quad f_r = \frac{-\eta}{2\sin^2\theta/2} \cdot e^{-i\eta \log \sin^2 \theta/2} \quad . \tag{AI-6}$$

If there is, in addition, some spin independent background scattering resulting from a finite range scalar potential discontinuity, producing a phase shift - φ_L, just outside its range, we modify (AI-6) to read

$$k^2\sigma_b = |f_r + f_p|^2, \quad f_p = -\sum_{L=0}^{\infty} (2L+1) e^{2i\omega_L - i\varphi_L} \sin\varphi_L \cdot P_L(x) \quad . \tag{AI-7}$$

For example, a square well discontinuity yields a "potential" phase shift $-\varphi_L$, finite for all L's. The background cross section resulting from the discontinuity is a smooth function of energy and angle. The background terms may then be considered as a modification to the Coulomb cross section. We can also add to the amplitude a single resonance with total spin J, parity π, and decaying with orbital angular momenta L_1, L_2, in the elastic channel (see Table I). From R-matrix theory we find that, neglecting the level shift, we may write the resonant amplitude as

$$\langle J^\pi, L', c' | F^J | J^\pi, L, c \rangle = \frac{|L, c\rangle \, |L', c'\rangle}{E_\lambda - E - i\Gamma/2} \quad . \tag{AI-8}$$

$$|L, c\rangle = e^{i(\omega_L - \varphi_L)} \cdot \sqrt{P_L(r)} \cdot \gamma_{L,c} \Big|_{r = r_c} \quad , \tag{AI-9}$$

where P_L = the penetration factor in channel c, for $r = r_c$,
$\gamma_{L,c}$ = the reduced width for the decay of the resonant state in

channel $|L, c\rangle$. We add (AI-8) to $f_b = f_r + f_p$, and take the absolute value squared. The interference term between f_b and F^J will contain only terms of the form $F^J_{L,\,L,\,E}$, since the background we use is elastic and diagonal in the L representation (spin independent). After carrying out the C. G. algebra we find

$$k^2\sigma_E(x) = k^2\sigma_B(x) + 2\mathrm{Re}\left\{\sum_{L=o}^{\infty} f_b^*(x) F^J_{L,\,L,\,E}\cdot P_L(x)\cdot\frac{2J+1}{2S_E+1}\right\} + W^J_E(x)$$

(AI-10)

$$k^2\sigma_I(x) = W^J_I(x)$$

$$W^J_c(x) = \frac{1}{\epsilon^2}\sum_{\substack{L=o\\ L\ \text{even}}}^{\infty} B_{L,\,c}\,P_L(x),\quad \epsilon^2 = (E_\lambda - E)^2 + \frac{\Gamma^2}{4} \qquad \text{(AI-11)}$$

$$B_{o,E} = \frac{2J+1}{2S_E+1}\cdot\frac{\Gamma_E^2}{4},\quad B_{L,E} = \Omega^2_{L,\,E}\ , \qquad \text{(AI-12)}$$

$$B_{o,I} = \frac{2J+1}{2S_E+1}\cdot\frac{\Gamma_E\Gamma_I}{4}\ ,\quad B_{L,I} = \Omega_{L,E}\cdot\Omega_{L,I}\ . \qquad \text{(AI-13)}$$

S_E is the spin in the elastic channel and so is 3/2 here. By orbital parity conservation, only a few γ_L's are non-zero in (AI-9). Given the reduced widths in the parity-helicity basis, one then consults Table I to find which γ_L's are non-zero. There remains to find $\Omega_{L,c}$. In terms of the $\bar{Z}$ coefficients of LT and the definition (AI-9) we get

$$\Omega_{L,\,c} = \sum_{L_1,\,L_2} \langle L_2,\, c \,|\, L_1,\, c \rangle\, \bar{Z}(L_1,\, J,\, L_2,\, J,\, S_c,\, L)\,. \quad \text{(AI-14)}$$

$|L,\, c\rangle$ is not real, according to (AI-9), but the imaginary parts of the matrix elements cancel out in (AI-14), since $\Omega_{L,\,c}$ is symmetrical in L_1 and L_2. Thus, we may write

$$\Omega_{L,\,c} = \sum_{\substack{L_1 L_2 \\ L_1 \le L_2}} a_{L_1,\,L_2}\; P_{L_1} P_{L_2} \gamma_{L_1} \gamma_{L_2} \cos(\omega_{L_1} - \omega_{L_2} - \varphi_{L_1} + \varphi_{L_2}) \Big|_{r=r_c}\,. \quad \text{(AI-15)}$$

The a's are real. We have calculated them, with the help of a computer program, for all L_1, L_2, L, J, π, up to J = 9/2. The non-zero ones are presented in Table II. The values for L = o are also given, although Ω_o is simple, if only to indicate when an angular distribution is isotropic.

We do an example to illustrate the use of Table II. Consider a state with $J = 3/2^+$ and Coulomb scattering only. Put

$$sn = \sin^2 \theta/2\,, \quad \zeta = \eta \log(sn)\,.$$

Equation (AI-10) becomes, after consulting Table I and II

$$k^2 \sigma_E(x) = \frac{\eta^2}{4\,sn^2} - \frac{\eta}{sn} \cdot \mathrm{Re}\left[\frac{e^{i\zeta}}{e}\left(e^{2i\omega_1} P_1 \gamma_1^2 P_1(x) + e^{2i\omega_3} P_3 \gamma_3^2 P_3(x)\right)\right]_E$$

$$+\; W_E^{3/2}(x)\,.$$

P_1 and P_3 are the penetration factors in the elastic channel, γ_1 and γ_3 are the reduced widths for the decay of the resonance with L = 1 and 3 in the elastic channel,

$$W_E^{3/2}(x) = \frac{1}{|\epsilon|^2}\left[\frac{\Gamma_E^2}{4} + \Omega_{2,E}^2 P_2(x)\right] ,$$

$$\Omega_{2,E} = 0.8(\gamma_1^2 P_1 - \gamma_3^2 P_3) + 1.2\sqrt{P_1 P_3}\,\gamma_1\gamma_3\cos(\omega_1 - \omega_3) ,$$

$$W_I^{3/2} = \frac{1}{|\epsilon|^2}\frac{\Gamma_I}{2}\left[\frac{\Gamma_E}{2} + \Omega_{2,E} P_2(x)\right] .$$

The formulae derived in this appendix made no assumption about the number of open channels; they are thus valid above the neutron threshold and indeed at any non-relativistic energy. Of course, we must then assign Γ_E, Γ_I, Γ separately since they would no longer be related by the unitarity condition $\Gamma = \Gamma_E + \Gamma_I$, above the neutron threshold. This is one reason for presenting Table II: it solves the problem of elastic and inelastic single-resonance angular distribution, for our reaction, up to J = 9/2 and at all energies. The table was also found useful to check the main multilevel program, described in Appendix II, in its single level limit.

The main program uses the units and definitions introduced in this appendix or their immediate generalization when necessary. Thus, we have here a good illustration of the structure of this more complex program. The equations of many-channel R-matrix theory

are familiar and would only add bulk if they were reproduced here. For this reason only the use of the model-program is discussed in detail in Appendix II.

APPENDIX II

A Two-Channel Ten-Level Model-Program

This program essentially represents Fortran coding for equations 1.6b, 1.5, 2.6 of LT[18]. We have rederived these equations and corrected some obvious typographical errors contained there. The definitions of the Coulomb wave functions used in this program are those of Appendix I. We first present a list of the binary decks required, along with a short description of their function:

Deck Name	Function
YRCRT6	Main program, selects options, controls input-output, (listed here).
YRCBON	Selects the boundary condition to make the level shift vanish at the given (input) energies.
YRCCOF	Calls YRCCOU to tabulate penetration factors.
BAZPLC	Computes Legendre polynomials.
YRCCOU	Computes Coulomb wave-functions (listed here).
YRCSCA	Main subroutine, coding for equations 1.6b, 1.5, 2.6, (listed here).
YRCFPL	Plots model angular distributions.
YRCGPO	Calls YRCFPL, bookkeeping.
YRCWID	Computes reduced widths from given (input) total width, and mixing angle (defined below).

Deck Name	Function
YRCCOA	Calls YRCCOU to tabulate all Coulomb parameters.
YRCAND	Computes angular dependence.
YRCDMD	Double precision matrix division.
YRCINI	Initial tabulation of often-used C. G. coefficients.
MJMTRA	Auxiliary output, a trace subroutine for debugging.
YRCTAC	Reads tables of C. G. coefficients.
YRC3JS	Computes Wigner's 3-J symbols.
YRCDEL	Called by YRC3JS, triangle condition.
YRCFAC	BLOCK COMMON table of factorials.
YRCFDB	Double precision table of factorials.

A deck is submitted according to the standard Caltech format, IBJOB, containing all the binary decks listed above and a $DATA section, under the IBJOB option NO SOURCE. An N-level "model" consists of N + 3 data cards. The first card contains the number of levels, the first C. M. energy in MeV at which an angular distribution is to be obtained, the energy step size, the number of steps, the radius at which the elastic penetration factor is to be evaluated, the inelastic penetration radius, the potential radius. The second card contains printout control integers. The third card contains the ten values of the energies at which the level shift must vanish, for each $J^{\pi}(1/2 \leq J \leq 9/2)$. Each of the succeeding N cards contains the level parameters for one resonance, which may be specified as:

$\varphi = \tan^{-1} \frac{\gamma_{L+2}}{\gamma_L}$ the mixing angle in radians between the two L

values in the elastic channel (compare Table I), Γ_{total} in MeV, Γ_I/Γ_E, $\pi = \pm 1.0$, E_λ (which is equal to E_r if the level shift vanishes at E_λ), J = N.5, N = 1-4. The format of these data cards is specified in the listing of YRCRT6.

The model-program first evaluates the boundary condition. Then the reduced widths are selected to give the specified values of Γ_T, Γ_I/Γ_E and φ. Next all the necessary Coulomb and potential parameters are computed. These numbers are used as input to the main subroutine YRCSCA which computes the R-matrix, the L' matrix, inverts $(\underset{\approx}{I} - \underset{\approx}{R}\underset{\approx}{L}')$, computes the scattering amplitude $\underset{\approx}{F}^J$ according to the formula $\underset{\approx}{F}^J = \underset{\approx}{\Omega}(\underset{\approx}{I} + \underset{\approx}{P}^{1/2} \cdot (\underset{\approx}{I} - \underset{\approx}{R}\underset{\approx}{L}')^{-1}\underset{\approx}{R} \cdot \underset{\approx}{P}^{1/2} \cdot 2i)\underset{\approx}{\Omega}$, evaluates the coefficients of the Legendre polynomials for the interference, nuclear elastic and nuclear inelastic series. Control is then returned to the main program which calls subroutines to evaluate the Legendre polynomials series at various angles and print the answers. We provide here listings of the main program, the main subroutine, and the subroutine which computes Coulomb wave-functions. This last listing is presented here because it represents a departure from the current practice of evaluating the irregular wave-function with an asymptotic series. Both wave-functions are evaluated using power series. This, plus the use of a double-precision recursion relation, allows us to compute all the Coulomb parameters for L = 0-6 in 200 ms, on the 7094, thus saving nearly a factor of 5, in time, over the routines currently in use in this laboratory.

```
$IBFTC RT6     DECK
C      THIS VERSION DOES NOT TAKE A VARIABLE BACKGROUND.
C
C       NTET=1 NO WIDTH
C
       COMMON /WIDT/X(3),AMP(14),GAME,GAMI
       COMMON /HETO/ HETOL(6,5,14)
       COMMON /BCEC/ BCE(14,5)
       DIMENSION TE(3),CBE(46),SER(10),IZT(7,8),FIPV(10)
       COMMON /SCAT/ B1L(7),B2L(7),CLE(10),CLI(10),ITEST(5)
      1 ,SIGT(6,6),SIGTR(6,6),AIMT(6)
       COMMON /ANDIR/ CYET,CYIT,CBET
       COMMON /COULB/ PLE(14,5),SCOUL(14),OMEG(14,5),PHI(14),SLE(14,5)
       COMPLEX SCOUL,OMEG,CAP
       COMMON /COULP/PLEA(14),SCOULA(14),OMEGA(14),PHA(14),SLEA(14)
       COMPLEX SCOULA,OMEGA
       COMMON /R2L/ R2LM1(7),UTL(14,5,6),UCL(6,5,6)
       DIMENSION CYE(46),CYI(46)
       DIMENSION RMATPA(10,8),RMATL(10,16)
       DATA PI,TERI/3.14159265,.06635/
       DATA TE /1.571,2.775,3.1416/
C
C      INITIALISE
C
       CALL INITIA
       BLYE= .01
       BLYI= .001
C
C      READ DATA
C
   88 READ(5,77) NR,STARTE,DELE,NEN,RADE,RADI,STATE,DETET,NTET,
     1 STAFI,DEFI,NFI,RADP
   77 FORMAT (I2,2F7.4,I2,4F7.4,I2,2F7.4,I2,F7.4)
      IF(NR.EQ.0) STOP
      READ(5,83) IZT,V,INP,JP
   83 FORMAT (56I1,4XF10.6,7XI1,I2)
      READ(5,81) SER
   81 FORMAT (10F8.4)
      READ(5,79) ((RMATPA(I,J), J= 1,8), I= 1,NR)
   79 FORMAT (8F7.4)
      ASSIGN 13 TO NG
      IF(RADE.EQ.RADP) ASSIGN 15 TO NG
      WRITE(6,903) RADE, RADI,RADP
  903 FORMAT (16H ELASTIC RADIUS=, F7.4, 17HINELASTIC RADIUS= , F7.4,
     1 17HPOTENTIAL RADIUS= F7.4)
      CALL BOUND(SER,RADE)
      FIP= STAFI
      DO 10 IFI= 1,NFI
      E= STARTE
      DO 1 K= 1,NR
      ER= RMATPA(K,7)
      J= RMATPA(K,8)+ .5
      JPA= RMATPA(K,6)
      GAMT= RMATPA(K,3)
      JQ =-((JPA+1)/2)*3
      X(1)= RMATPA(K,1)
      X(2)= RMATPA(K,2)
      RIOE= RMATPA(K,5)
      IF(X(1).NE.20.) GO TO 19
      IF(IFI.EQ.1) FIPV(K)= X(2)
```

```
      FIP= FIPV(K)
      CALL WIDTH(ER,GAMT,FIP,RIOE,J,JPA,RADE,RADE,0)
      GO TO 17
   19 X(3)= RMATPA(K,4)
      DO 7 L = 1, 14
      AM = 0.
      DO 9 I = 1, 3
      IPA = I + JQ+ 3
    9 AM = AM + HETOL(IPA,J,L)*X(I)
    7 AMP(L) = AM
      WRITE(6,501) K,X,AMP
  501 FORMAT(24HX AND AMP VECTORS FOR K= I2/1P3(2XE12.5)/
     1 7(2XE12.5)/7  (2X E12.5))
   17 RMATL(K,16)= RMATPA(K,8)
      FIPV(K)= FIPV(K)+ DEFI
      RMATL(K,15)= RMATPA(K,7)
      DO 3 L= 1,14
    3 RMATL(K,L)= AMP(L)
    1 CONTINUE
      DO 12 IEN= 1,NEN
      IPOT= 1
      IP= 0
      IF(JP.LT.5) GO TO 11
      IP= 1
   11 GO TO NG, (13,15)
   13 CALL COULPA(E,RADP,RADP,IP,PHI,IPOT)
      IPOT= 0
   15 CALL COULFA(E,RADE,RADI,IP,PHA,IPOT,BCE)
      CALL SCATCO(E,NR,RMATL,PLE,OMEG,SLE,JP)
      IF(JP.LT.4) GO TO 5
      WRITE(6,959)
  959 FORMAT (/15HBOUNDARY MATRIX /)
      WRITE(6,961) BCE
  961 FORMAT (1P7(3XE12.5))
      WRITE(6,963)
  963 FORMAT (/18HPENETRATION MATRIX /)
      WRITE(6,961) PLE
      WRITE(6,965)
  965 FORMAT (/12HSHIFT MATRIX /)
      WRITE(6,961) SLE
      WRITE(6,967)
  967 FORMAT (/12HRMATL MATRIX/)
      WRITE(6,969) RMATL
  969 FORMAT (1P10(1XE12.5))
    5 A3= 1.
      WRITE(6,905) E,A3,ITEST,B1L,B2L,CLE,CLI
  905 FORMAT (1H0F10.4 ,4XF10.4, 4X5I1/7F10.4/7F10.4/10F10.4/10F10.4)
      IF(JP.LT.1) GO TO 85
      WRITE(6,951)
  951 FORMAT (11HAIMT VECTOR )
      WRITE(6,955) AIMT
      WRITE(6,953)
  953 FORMAT (12HSIGTR MATRIX )
      WRITE(6,955) SIGTR
  955 FORMAT((6(2XE12.5)))
      WRITE(6,957)
  957 FORMAT (11HSIGT MATRIX )
      WRITE(6,955) SIGT
C
C     PREPARE PLOTTING TABLE
```

```
C
      WRITE(6,505)
  505 FORMAT (/12HSCOUL VECTOR/)
      WRITE(6,507) SCOUL
  507 FORMAT ((1H/7(2F8.5,1H/)))
   85 AL= 1.51/SQRT(E)
      PH= 1.
      DO 701 IT= 1,3
      TER= TE(IT)
      CALL ANDI(AL,SCOUL,TER,B1L,B2L,CLE,CLI,PH)
      CYE(IT)= CYET
      CYI(IT)= CYIT
      CBE(IT)= CBET
  701 TER= TER+ TERI
  707 FORMAT (1H1)
      WRITE(6,709) E,(CBE(N),CYE(N),CYI(N),N= 1,3)
  709 FORMAT (31HELASTIC AND INELASTIC YIELD ARE /1P10(1XE12.5))
      CALL GPLOT(E,SCOUL,B1L,B2L,CLE,CLI,PH,INP)
   12 E= E+ DELE
   10 FIP= FIP+ DEFI
      GO TO 88
      END
$IBFTC SCA      DECK
      SUBROUTINE SCATCO(E,NR,RMATL,PLE,OMEGE,SLE,IP)
C     B1L IS THE COEF OF THE COS INT TERM
C     B2L IS THE COEF OF THE SIN INTERF TERM
C     CLE IS THE ELASTIC NUCLEAR PART
C     CLI IS THE INELASTIC NUCLEAR PART
C     RMATL CONTAINS THE R MAT. PAR. IN L REP.
C     NR IS THE NUMBER OF LEVELS
C     SUBR. INITIA MUST BE CALLED FIRST IN MAIN TO FILL TABLES
C     OF UTT AND R2LM1. UTT IS A FCN PROG.
      DIMENSION R(6,6),TS(6,6),OMEGE(14,5),PLE(14,5),SLE(14,5),RR(6)
      DIMENSION T(5,6,6),RMATL(10,16),PLC(6),OMC(6),SLC(6 )
      COMMON /SCAT/ B1L(7),B2L(7),CLE(10),CLI(10),ITEST(5)
     1 ,SIGT(6,6),SIGTR(6,6),AIMT(6)
      COMMON /R2L/ R2LM1(7),UTL(14,5,6),UCL(6,5,6)
      COMPLEX TS,OMP,T,OMEGE,CBP,OMC
      COMPLEX W(6,6)
      DOUBLE PRECISION RD(6,6),TSD(6,6),DT,DTT,EA(6,6),ARD(6,6)
C
C     GENERATE THE R MATRIX FOR J= .5 TO 4.5
C     THE R MAT. PAR. ARE IN L REP.
C
      DO 289 M= 1,6
      AIMT(M)= 0.
      DO 289 N= 1,6
      SIGT(M,N)= 0.
  289 SIGTR(M,N)= 0.
      DO 66 J= 1, 5
      F2J= 2*J
      EPS= 1.E-10
      JIN=  MAXO(1,J-1) -1
      J2= J+ 2
      J7= J+ 7
      J8= J+ 8
      DO 209 L = 1,6
      DO 209 LP= 1,6
  209 R(L,LP)= 0.
      IS= 0
```

```
      DO 230 K= 1,NR
      IF(RMATL(K,16).NE.(FLOAT(J)- .5))GO TO 230
      IS= 1
C
C     NOW COMPUTE R
C
      DO 291 M= 1,4
      LC= JIN+ M
  291 RR(M)= RMATL(K,LC)
      RR(5)= RMATL(K,J7)
      RR(6)= RMATL(K,J8)
      ENDENI= 1./(RMATL(K,15)- E)
      DO 207 L= 1,6
      DO 207 LP= 1,L
      R(L,LP)= R(L,LP)+ RR(L)*RR(LP)*ENDENI
      R(LP,L)= R(L,LP)
      RD(L,LP)= R(L,LP)
      ARD(L,LP)= RD(L,LP)
      RD(LP,L)= RD(L,LP)
      ARD(LP,L)= ARD(L,LP)
  207 CONTINUE
  230 CONTINUE
      IF(IS.EQ.0) GO TO 271
      DO 293 M= 1,4
      LC= JIN+ M
      PLC(M)= PLE(LC,J)
      OMC(M)= OMEGE(LC,J)
      SLC(M)= SLE(LC,J)
  293 CONTINUE
      DO 295 M= 5,6
      LC= J2+ M
      PLC(M)= PLE(LC,J)
      OMC(M)= OMEGE(LC,J)
      SLC(M)= SLE(LC,J)
  295 CONTINUE
      IF(IP.LT.1) GO TO 299
      WRITE(6,501)
  501 FORMAT(8HR MATRIX )
      WRITE(6,503) R
  503 FORMAT (1P(6(2XE12.5)))
C
C     GENERATE 1- RLO AND INVERT IT
C
  299 DO 297 L= 1,6
      OL= SLC(L)
      DO 297 LP= 1,6
      DT= 0.
      IF(L.EQ.LP) DT= 1.
      TSD(LP,L)= DT- RD(LP,L)*OL
  297 EA(LP,L)= TSD(LP,L)
      CALL DOMDIV(TSD,ARD,6,DETE,EPS,ITE)
      EPS= 1.E-10
      DO 211 L= 1,6
      DO 211 LP= 1,6
      DTT= 0.
      DO 283 K= 1,6
  283 DTT= DTT+ RD(L,K)*PLC(K)*ARD(K,LP)*PLC(LP)
  211 TSD(L,LP)= DTT+ EA(L,LP)
      CALL DOMDIV(TSD,RD,6 ,DETE,EPS,ITE)
      ITEST(J)= ITE+1
```

```
      IF(ITE.NE.0) RETURN
      DO  287 L= 1,6
      DO 287 LP= 1,L
      TOS= 0.
      DO 285 K= 1,6
  285 TOS= TOS+ SNGL(RD(L,K))*PLC(K)*SNGL(ARD(K,LP))
      W(L,LP)= CMPLX(SNGL(RD(L,LP)),TOS)
  287 W(LP,L)= W(L,LP)
C
C     IN R THERE IS NOW (1- RLO)INV*R= W
C     CONSTRUCT OMEG*W*OMEG+ I*SJ= T
C
      DO 215 L= 1,6
      DO 215 LP= 1,L
      TS(L,LP)= OMC  (L)*W(L,LP)*OMC  (LP)
  215 TS(LP,L)= TS(L,LP)
      IF(IP.LT.2) GO TO 301
      WRITE(6,505)
  505 FORMAT (8HW MATRIX )
      WRITE(6,507) W
  507 FORMAT ((1H/6(2F8.5,1H/)))
      WRITE(6,509)
  509 FORMAT (9HTS MATRIX )
      WRITE(6,507) TS
C
C     NOW CONVERT BACK TO THE HEL. REP. USING UTL MATRIX
C
  301 DO 217 M= 1,6
      DO 219 N= 1,M
      OMP= (0.,0.)
      DO 221 L= 1,6
      DO 223 LP= 1,6
      OMP= OMP+    UCL(L,J,M)*TS(L,LP)*UCL(LP,J,N)
  223 CONTINUE
  221 CONTINUE
      T(J,M,N)= OMP
      T(J,N,M)= OMP
      SIGTR(M,N)= SIGTR(M,N)+ F2J*(REAL(OMP)**2+ AIMAG(OMP)**2)
      SIGTR(N,M)= SIGTR(M,N)
      IF(M.NE.N) GO TO 219
      AIMT(M)= AIMT(M)+ F2J*AIMAG(OMP)
  219 CONTINUE
  217 CONTINUE
      IF(IP.LT.3) GO TO 66
      WRITE(6,511) J, ((T(J,M,N), M= 1,6), N= 1,6)
  511 FORMAT (16HT MATRIX FOR J = I2/  (6(2F10.6,1H/)))
      GO TO 66
  271 DO 273 M= 1,6
      DO 273 N= 1,6
  273 T(J,M,N)= (0.,0.)
      ITEST(J)= 3
C     THE NEXT CONTINUE IS THE END OF THE J LOOP
   66 CONTINUE
C
C     CALCULATE THE COEFFICIENTS OF THE LEGENDRE POLYNOMIALS
C
      JMAX= 0
      DO 275 J= 1,5
      IF(ITEST(J).EQ.1) JMAX= J
  275 CONTINUE
```

```
      LIM= JMAX+ 2
      LNM= 2*JMAX
C     CALCULATE THE INTERFERENCE COEFFICIENTS
      DO 36 L= 1,LIM
      CBP= (0.,0.)
      DO 35 J= 1,5
      IF(ITEST(J).EQ.3) GO TO 35
      DO 34 M= 1,4
      DO 33 N= 1,M
      DE= 2.
      IF(M.EQ.N) DE= 1.
      OMP= T(J,M,N)
      CBP= CBP+ .5*UTT(L,2,J,M,N)*DE*OMP
   33 CONTINUE
   34 CONTINUE
   35 CONTINUE
      CBP= (FLOAT(L)- .5)*.5*CBP
      B1L(L)= REAL(CBP)
      B2L(L)= AIMAG(CBP)
   36 CONTINUE
      IF(LIM.EQ.7) GO TO 279
      LIM= LIM+1
      DO 277 L= LIM,7
      B1L(L)= 0.
  277 B2L(L)= 0.
C
C     CALCULATE THE INELASTIC NUCLEAR PART
C     CALCULATE THE ELASTIC NUCLEAR PART
  279 DO 46 L= 1,LNM
      CLP= 0.
      CLEP= 0.
      CLIP= 0.
      DO 45 JP= 1,5
      IF(ITEST(JP).EQ.3) GO TO 45
      DO 44 J= 1,JP
      IF(ITEST(J).EQ.3) GO TO 44
      DEJ= 2.
      IF(JP.EQ.J) DEJ= 1.
      DO 43 M= 1,4
      DO 42 N= 1,M
      DEN= 2.
      IF(M.EQ.N) DEN= 1.
      CBP= T(J,M,N)
      OMP= T(JP,M,N)
      CLP= UTT(L,JP,J,M,N)  *(REAL(CBP)*REAL(OMP)+ AIMAG(CBP)*AIMAG(OMP
     1 ))*DEJ
      CLEP= CLEP+ DEN*CLP
      IF(L.NE.1) GO TO 42
      SIGT(M,N)= SIGT(M,N)+ CLP
   42 CONTINUE
      DO 52 N= 5,6
      CBP= T(J,M,N)
      OMP= T(JP,M,N)
      CLP= UTT(L,JP,J,M,N-3)*(REAL(CBP)*REAL(OMP)+ AIMAG(CBP)*AIMAG(OMP
     1 ))*DEJ
      CLIP= CLIP+ CLP
      IF(L.NE.1) GO TO 52
      SIGT(M,N)= SIGT(M,N)+ CLP
   52 CONTINUE
   43 CONTINUE
```

```
   44 CONTINUE
   45 CONTINUE
      CLE(L)= (FLOAT(L)- .5)*CLEP
      CLI(L)= (FLOAT(L)- .5)*CLIP
   46 CONTINUE
      IF(LNM.EQ.10) RETURN
      LNM= LNM+ 1
      DO 281 L= LNM,10
      CLE(L)= 0.
  281 CLI(L)= 0.
      RETURN
       END
$IBFTC COU      DECK
      SUBROUTINE COUL(ETA,RO)
C     TO CALCULATE AND STORE IN COMMON/COU/ THE COULOMB WAVE FUNC-
C     TIONS FROM L=0 TO L= 6
C     REF. H. DER PHYSIK P408 FOR L= 0 PART
C     AND LANE AND THOMAS P350 FOR RECURSION RELATIONS
      COMMON /COU/ F,FP,G,GP,PHI,AS,P,S,CP,IC,IPRINT
      DIMENSION F(7),FP(7),G(7),GP(7),PHI(7),AS(7),P(7),S(7),CP(7),ZM(6)
      DOUBLE PRECISION PI,PL0,PL1,SL0,SL1,PHI0,PHI1,AL,BL,ROD,ETAD,DL,
     1 ZM,A2,RN2,RN,REM,RN7
      DATAPI/3.141592653589793D0/,(ZM(K),K= 1,6)/.5772156649 01532 861,
     1 .20205 69031 59594 285, .36927 75514 33699 263D-1,
     2 .83492 77381 92282 683D-2,2*0./
C
C     CALCULATE S PART
C
      CN= SQRT(2.*ETA*SNGL(PI)/(SNGL(DEXP(2.D0*PI*DBLE(ETA))-1.D0)))
      BL0= 0.
      BL1= 1.
      BS0= 1.
      BS1= 0.
      TOETAR= 2.*ETA*RO
      ROSQR= RO*RO
      FI= 1.
      FIP= 0.
      PSI= 1.
      IC= 0
      DO 201 J= 2,400
      CJ= FLOAT(J*(J-1))
      BL2= (TOETAR*BL1- ROSQR*BL0)/CJ
      BS2= (TOETAR*(BS1- FLOAT(2*J-1)*BL2)- ROSQR*BS0)/CJ
      IF((FI+ BL2).NE.FI) GO TO 203
      IF((FIP+FLOAT(J-1)*BL2).NE.FIP) GO TO 203
      IF((PSI+ BS2).NE.PSI) GO TO 203
      GO TO 205
  203 FI= FI+ BL2
      FIP=   FIP+ FLOAT(J-1)*BL2
      PSI= PSI+ BS2
      BL0= BL1
      BL1= BL2
      BS0= BS1
  201 BS1= BS2
      IC= 1
C     THE 3 POWER SERIES HAVE BEEN EVALUATED
C     NOW CALCULATE F1(ETA)
C
  205 A2= ETA*ETA
      REM= 0.
```

```
      DO 207 N= 2,100
      RN= N
      RN2= RN*RN
      RN7= RN2*RN2*RN2*RN
      REM= REM+ 1./(RN7*(RN2+ A2))
  207 CONTINUE
      DO 101 I= 1,3
      II= 5- I
  101 REM= ZM(II )- A2*REM
      FETA= ZM(1)- 1./(1.+ A2)+ A2*REM
C
C     COMPUTE THE PARAMS FOR L= 0 AND INITIALISE THE RECURSION REL.
C
      F(1)= CN*RO*FI
      FP(1)= CN*(FI+ FIP)
      G(1)= (PSI+ 2.*ETA*(ALOG(2.*RO)+ FETA)*RO*FI)/CN
      GP(1)= (FP(1)*G(1)- 1.)/F(1)
      PHI(1)= ATAN2(F(1),G(1))
      AS(1)=F(1)**2+ G(1)**2
      P(1)= RO/AS(1)
      S(1)= (F(1)*FP(1)+ G(1)*GP(1))*P(1)
      CP(1)= 0.
      PL0= DBLE(P(1))
      SL0= DBLE(S(1))
      PHI0= DBLE(PHI(1))
      ROD= DBLE(RO)
      ETAD= DBLE(ETA)
C
C     THE RECURSION RELATION IS DONE IN DOUBLE PRECISION
C
      DO 211 L= 2,7
      DL= DBLE(FLOAT(L-1))
      AL= ROD**2*(1.D0+  (ETAD/DL)**2)
      BL= DL+ ROD*ETAD/DL
      PL1= AL*PL0/((BL- SL0)**2+ PL0**2)
      P(L)= SNGL(PL1)
      SL1=-BL+AL*(BL- SL0)/((BL- SL0)**2+ PL0**2)
      S(L)= SNGL(SL1)
      PHI1= PHI0- DATAN2(PL0,(BL- SL0))
      TSIN= SIN(SNGL(PHI1))
      TCOS= COS(SNGL(PHI1))
      AS(L)= RO/SNGL(PL1)
      TSQR= SQRT(AS(L))
      F(L)= TSQR*TSIN
      G(L)= TSQR*TCOS
      FP(L)= (SNGL(SL1)*TSIN+ SNGL(PL1)*TCOS)/SQRT(RO*SNGL(PL1))
      GP(L)= (FP(L)*G(L)- 1.)/F(L)
      CP(L)= CP(L-1)+ ATAN2(ETA,FLOAT(L-1))
      PHI(L)= SNGL(PHI1)
      PL0= PL1
      SL0= SL1
  211 PHI0= PHI1
C
C     THE TABLE IS COMPLETE, PRINT AND/OR RETURN
      IF(IPRINT.EQ.0) RETURN
      WRITE(6,221) RO,ETA,F,FP,G,GP,PHI,AS,P,S,CP,IC
  221 FORMAT (/10X26HCOULOMB PARAMETERS FOR RO= 1PE12.5,2X8HAND ETA=
     1 E12.5/ 5H L  = 12X1HO 15X1H115X1H215X1H315X1H415X1H515X1H6//
     2 5H F  =3X7(4XE12.5)/ 5H FP =3X7(4XE12.5)/ 5H G  =3X7(4XE12.5)/
     3 5H GP =3X7(4XE12.5)/ 5H PHI=3X7(4XE12.5)/ 5H AS =3X7(4XE12.5)/
     4 5H P  =3X7(4XE12.5)/ 5H S  =3X7(4XE12.5)/ 5H CP =3X7(4XE12.5)/
     6 5H IC = I1)
      RETURN
      END
```

REFERENCES

(1) See for example: Wu and Ohmura, "Quantum Theory of Scattering" Prentice Hall, 1962, especially chapters 5 and 6.

(2) Bichsel and Bonner, Phys. Rev. 108, 1025 (1957).

(3) Heidenburg and Temmer, Phys. Rev. 94, 1252 (1954).

(4) Li and Sherr, Phys. Rev. 96, 389 (1954).

(5) A. B. Clegg, Nuclear Physics 38, 353 (1962).

(6) D. Kurath and L. Pičman, Nuclear Physics 10, 313 (1959).

(7) Professor T. Lauritsen, private communication.

(8) S. G. Nilsson, Dan. Mat. Fys. Medd. 29, no. 16 (1955).

(9) J. C. Overley, "A Study of the Elastic Scattering of Protons by B^{10}," Thesis, California Institute of Technology, 1961, (unpublished).

(10) J. C. Overley and W. Whaling, Phys. Rev. 128, 315 (1962).

(11) R. K. Bardin, thesis, California Institute of Technology, (1961) (unpublished).

(12) This unit was used recently by P. Parker and is described in: P. D. M. Parker, thesis, California Institute of Technology, (1963), (unpublished).

(13) G. Dearnaley, Rev. Sci. Instr. 31, 197 (1960).

(14) "1960 Nuclear Data Tables", Part 3, pp 10, 18; published for The United States Atomic Energy Commission, (1960).

(15) C. S. Zaidens, "Charge States of Heavy Ions Beams in Matter", California Institute of Technology, (1962), (unpublished).

(16) C. W. Li, thesis, California Institute of Technology, (1951), (unpublished).

(17) For a convenient summary of the method, with equations given in Fortran language, see:
P. A. Seeger, "Summary-General Least Squares", California Institute of Technology, (1963), (unpublished).

(18) A. M. Lane and R. G. Thomas, Rev. Mod. Phys. 30, 257 (1958).

(19) M. Jacob and G. C. Wick, Annals of Physics 7, 404 (1959).

(20) Bates, Massey and Stewart, Proc. Roy. Soc. (London) A216, (1953).

(21) Gordon, Zeits. f. Physik, 48, 180 (1928).

(22) E. Vogt, Physics Letters, 1, 84 (1962).

(23) Elkins, Phys. Rev. 92, 127 (1953).

(24) D. E. Groce, J. H. McNally, and W. Whaling, Bull. Am. Phys. Soc. 8, 486 (1963).

(25) W. E. Meyerhof, Phys. Rev. 129, 692 (1963).

(26) H. W. Newson, R. H. Williamson, K. W. Jones, J. H. Gibbons and H. Marshak, Phys. Rev. 108, 1294 (1957).

(27) C. M. Chesterfield and B. M. Spicer, Nuclear Physics 41, 675 (1963).

(28) P. H. Stelson and F. K. McGowan, Nuclear Physics, 16, 92 (1960).

(29) Alder, Bohr, Huus, Mottelson and Winther, Rev. Mod. Phys., 28, 432 (1956).

(30) M. K. Mehta et al., Nuclear Physics, 48, 90 (1963).

(31) D. Kurath, Phys. Rev., 101, 216 (1956).

(32) J. W. Olness, E. K. Warburton, D. E. Alburger and J. A. Becker, Brookhaven National Laboratory preprint, no. BNL 8932 (To be published in the Physical Reviews).

(33) F. Ajzenberg-Selove and T. Lauritsen, Nuclear Physics 11, 1 (1959).

(34) D. R. Inglis, Rev. Mod. Phys., 25, 390 (1953).

(35) A. N. Boiarkina, Izvestia Akademii Nauk SSSR, 28, 337 (1964).

(36) J. P. Elliott, Proc. Roy. Soc., A245, 128 (1958).

(37) W. Whaling, Handbuch der Physik, E. Flugge, ed., Springer-Verlag, Berlin, (1958), Vol. 34.

(38) A. E. Litherland, H. McManus, E. B. Paul, D. A. Bromley and H. E. Gove, Can. J. Phys. 36, 378 (1958).

(39) T. Lauritsen and F. Ajzenberg-Selove, "Energy Levels of Light Nuclei", Nuclear Data Sheets, sets 5 and 6 (1962), published by the N. R. C.

(40) Elliott and Skirme, Proc. Roy. Soc. (London), A232, 561 (1955).

(41) G. Baym, Physics Letters, 1, 241 (1962).

(42) C. van Winter, Physica, 20, 274 (1954).

(43) A. S. Davydov and R. A. Sardaryan, Nuclear Physics 37, 106 (1962).

TABLE I

It has been found convenient, in the text, to characterize a resonance in the channel $Li^7 + \alpha$ by its value of J^π and its decay amplitude for a given value of $|\lambda|$ the absolute value of the spin projection along the direction of motion. This parity-helicity representation is, however, not suitable outside the nucleus where Coulomb effects are dominant. This table does the conversion from one representation to the other. For example, a resonance with $J^\pi = 5/2^+$ may decay in the elastic channel with a spin projection of 3/2 or 1/2. According to the table, the decay with spin projection 3/2 has an amplitude of 0.632 for being L = 1 and 0.774 for being L = 3.

TABLE I

Matrix Elements for Conversion from Helicity to Orbital Angular Momentum Representation

		Elastic channel						
	ℓ =	0	1	2	3	4	5	6
J^{π}	$\|\lambda\|$, C							
$1/2^+$	3/2, E							
	1/2, E		-1.					
	1/2, I							
$1/2^-$	3/2, E							
	1/2, E			1.0				
	1/2, I							
$3/2^+$	3/2, E		-0.948		-0.316			
	1/2, E		-0.316		0.948			
	1/2, I							
$3/2^-$	3/2, E	0.707		0.707				
	1/2, E	0.707		-0.707				
	1/2, I							
$5/2^+$	3/2, E		0.632		0.774			
	1/2, E		0.774		-0.632			
	1/2, I							
$5/2^-$	3/2, E			-0.925		-0.377		
	1/2, E			-0.377		+0.925		
	1/2, I							
$7/2^+$	3/2, E				-0.912		-0.408	
	1/2, E				-0.408		+0.912	
	1/2, I							
$7/2^-$	3/2, E			0.597		0.801		
	1/2, E			0.801		-0.597		
	1/2, I							
$9/2^+$	3/2, E				0.577		0.816	
	1/2, E				0.816		-0.577	
	1/2, I							
$9/2^-$	3/2, E					-0.904		-0.426
	1/2, E					-0.426		+0.904
	1/2, I							

TABLE I (continued)

For the decay of a resonance in B^{11} into the channel $Li^{7*}(.48) + \alpha'$, the situation is much simpler because $Li^{7*}(.48)$ has $J^{\pi} = 1/2^{-}$, thus, only one L value for each J^{π} is allowed, and the matrix elements are $\pm$ 1.0. The phase is relevant in the case where there is another inelastic amplitude which has the same J^{π}.

See text page 22.

TABLE I (continued)

		Inelastic channel						
	ℓ =	0	1	2	3	4	5	6
J^{π}	$\|\lambda\|$, C							
$1/2^+$	3/2, E							
	1/2, E							
	1/2, I		-1.0					
$1/2^-$	3/2, E							
	1/2, E							
	1/2, I	1.0						
$3/2^+$	3/2, E							
	1/2, E							
	1/2, I		1.0					
$3/2^-$	3/2, E							
	1/2, E							
	1/2, I			-1.0				
$5/2^+$	3/2, E							
	1/2, E							
	1/2, I				-1.0			
$5/2^-$	3/2, E							
	1/2, E							
	1/2, I			1.0				
$7/2^+$	3/2, E							
	1/2, E							
	1/2, I				+1.0			
$7/2^-$	3/2, E							
	1/2, E							
	1/2, I					-1.0		
$9/2^+$	3/2, E							
	1/2, E							
	1/2, I						-1.0	
$9/2^-$	3/2, E							
	1/2, E							
	1/2, I					+1.0		

TABLE II-a

This table is to be used in conjunction with Appendix I. The nuclear part of the angular distribution due to an isolated resonance in B^{11} may be expanded in Legendre polynomials. The coefficients of $P_L(\cos\theta)$ contain sums of products of decay amplitudes for various L_1 and L_2 values, each multiplied by a number related to a Racah coefficient. The exact expressions are defined in equations (AI-10-15). We tabulate here these relevant coefficients for the elastic angular distributions.

TABLE II-a

Coefficients for Elastic Angular Distribution from the Reaction $Li^7 + \alpha \rightarrow B^{11}(J, \pi) \rightarrow Li^7 + \alpha$

J, π	L	L_1	L_2	a_{L_1, L_2}	J, π	L	L_1	L_2	a_{L_1, L_2}
$1/2^-$	0	2	2	0.707	$1/2^+$	0	1	1	0.707
$3/2^-$	0	0	0	1.0	$3/2^+$	0	1	1	1.0
	0	2	2	1.0		0	3	3	1.0
	2	0	2	2.0		2	1	1	0.8
						2	1	3	1.2
						2	3	3	-0.8
$5/2^-$	0	2	2	1.224	$5/2^+$	0	1	1	1.225
	0	4	4	1.224		0	3	3	1.225
	2	2	2	-0.468		2	1	1	-0.916
	2	2	4	0.687		2	1	3	0.962
	2	4	4	-1.169		2	3	3	-0.720
	4	2	2	-1.296		4	1	3	-2.777
	4	2	4	-1.984		4	3	3	-0.567
	4	4	4	0.729					
$7/2^-$	0	2	2	1.414	$7/2^+$	0	3	3	1.414
	0	4	4	1.414		0	5	5	1.414
	2	2	2	-1.322		2	3	3	-1.029
	2	2	4	0.591		2	3	5	0.460
	2	4	4	-1.146		2	5	5	-1.440
	4	2	2	0.760		4	3	3	-0.161
	4	2	4	-1.853		4	3	5	-1.441
	4	4	4	0.207		4	5	5	1.128
	6	2	4	3.303		6	3	3	1.641
	6	4	4	0.985		6	3	5	2.569
						6	5	5	-0.656
$9/2^-$	0	4	4	1.581	$9/2^+$	0	3	3	1.581
	0	6	6	1.581		0	5	5	1.581
	2	4	4	-1.385		2	3	3	-1.596
	2	4	6	0.336		2	3	5	0.410
	2	6	6	-1.662		2	5	5	-1.451
	4	4	4	0.535		4	3	3	1.215
	4	4	6	-1.082		4	3	5	-1.322
	4	6	6	1.428		4	5	5	0.748
	6	4	4	0.672		6	3	3	-0.649

TABLE II-a (continued)

J, π	L	L_1	L_2	a_{L_1, L_2}	J, π	L	L_1	L_2	a_{L_1, L_2}
$9/2^-$	6	4	6	2.102	$9/2^+$	6	3	5	2.569
	6	6	6	-1.062		6	5	5	0.259
	8	4	4	-1.903		8	3	5	-3.702
	8	4	6	-3.029		8	5	5	-1.309
	8	6	6	0.595					

TABLE II-b

This table is similar to Table II-a although simpler because of the reduced channel spin ($1/2^-$) in the inelastic channel. We tabulate here the coefficients defined in Appendix I for the inelastic single-resonance angular distributions.

TABLE II-b

Coefficients for Inelastic Angular Distributions from the Reaction: $Li^7 + \alpha \rightarrow B^{11}(J, \pi) \rightarrow Li^{7*}(.48) + \alpha'$

J^π	L	L_1	L_2	$a_{L_1L_2}$	J^π	L	L_1	L_2	$a_{L_1L_2}$
$1/2^+$	0	1	1	0.707	$1/2^-$	0	0	0	0.707
$3/2^+$	0	1	1	1.0	$3/2^-$	0	2	2	1.0
	2	1	1	1.0		2	2	2	1.0
$5/2^+$	0	3	3	1.225	$5/2^-$	0	2	2	1.225
	2	3	3	-1.309		2	2	2	-1.309
	4	3	3	1.134		4	2	2	1.134
$7/2^+$	0	3	3	1.414	$7/2^-$	0	4	4	1.414
	2	3	3	-1.543		2	4	4	-1.543
	4	3	3	1.450		4	4	4	1.450
	6	3	3	-1.230		6	4	4	-1.230
$9/2^+$	0	4	4	1.581	$9/2^-$	0	5	5	1.581
	2	4	4	-1.741		2	5	5	-1.741
	4	4	4	1.683		4	5	5	1.683
	6	4	4	-1.557		6	5	5	-1.557
	8	4	4	1.309		8	5	5	1.309

TABLE III

We present here a list of all the scattering anomalies observed in one phase of another of this experiment. The first six anomalies were studied in detail. The information obtained about their spin and parity is given. A single bracket indicates a probable assignment while a double bracket indicates a possible assignment which is not in contradiction with any presently available data.

See text page 24.

TABLE III

Scattering Anomalies Observed in the Reactions
$Li^7(\alpha, \alpha)Li^7$, $Li^7(\alpha, \alpha')Li^7(0.48)$

Identification No.	$E_x B^{11}$ MeV	Γ_T keV C. M.	J^π Remarks
1	9.88	130.0	$(3/2^+)$
2	10.26	160.0	weak, ((3/2))
3	10.32	70.0	$(\geq 5/2)^-$
4	10.60	70.0	$7/2^+$
5	10.96	950.0	((5/2))
6	11.27	160.0	$(7/2^+, 9/2^+)$
7	11.46	(60.0)	B^{10} + n Threshold
8	11.60	160.0	$((5/2^+, 7/2^+))$
9	11.91	140.0	(-)
10	12.04	900.0	
11	12.18	(60.0)	$B^{10}(0.72)$ + n Th.
12	12.55	145.0	((-))
13	13.06	290.0	((-))
14	13.25	(60.0)	$B^{10}(1.74)$ + n Th.
15	13.63	(440.0)	$B^{10}(2.18)$ + n Th.
16	14.00	450.0	Shoulder to 15
17	14.67	250.0	
18	15.03	(480.0)	$B^{10}(3.58)$ + n Th.
19	15.73	160.0	weak

TABLE IV

This table lists the parameters which were used in the model-program described in the text to compute the cross sections shown in Figures 21-23. $E_{\lambda C.M.}$ is the energy at which the R-matrix has a pole; it coincides with the resonance energy E_r at which the scattering amplitude has a maximum in all cases except for the level marked $E_{\lambda C.M.} = 2.90$ MeV. This is due to the fact that E_B, the energy at which the level shift vanishes, is 1.656 MeV in the channel $J^{\pi} = 5/2^-$. The angle $\varphi = \tan^{-1} \frac{\gamma_{L+2}}{\gamma_L}$, in radians, specifies the mixture between the L and L + 2 amplitudes in the elastic channel.

See text page 63.

TABLE IV

List of Resonance Parameters

for a 7-level fit to the observed cross section for the reactions $Li^7(\alpha, \alpha)Li^7$ and $Li^7(\alpha, \alpha')Li^{7*}(.48)$, below the B^{10} + n threshold at $E_{\alpha L}$ = 4.38 MeV.

$E_{\lambda C.M.}$	J^{π}	$\Gamma_{tot.}$	Γ_I/Γ_E	φ	E_B	$\gamma_{3/2,E}$	$\gamma_{1/2,E}$	$\gamma_{1/2,I}$
1.209	$3/2^+$	0.15	4.0	0.0	1.209	0.159	0.053	0.820
1.590	$3/2^-$	0.2	0.05	1.4	1.590	-0.251	0.356	0.188
1.656	$5/2^-$	0.1	0.0001	1.1	1.656	0.052	0.624	0.005
1.940	$7/2^+$	0.075	1.0	0.0	1.941	0.238	0.106	0.468
2.90	$5/2^-$	3.0	2.0	1.1	1.656	0.076	0.907	0.886
2.50	$1/2^+$	4.0	1.0	0.0	1.0	0.0	0.713	0.822
2.61	$7/2^+$	0.075	0.0001	0.0	1.941	0.209	0.093	0.003

Figure 1: Energy Level Diagram of B^{11} (39)

This figure shows the various thresholds for the reactions involving B^{11}. The present experiment is concerned with the levels of B^{11} that can be seen in the reactions $Li^7(\alpha, \alpha)Li^7(E_{tr} = 8.666$ MeV) and $Li^7(\alpha, \alpha')Li^{7*}(.48)(E_{tr} = 9.144$ MeV). The deexcitation γ-ray occurring in the inelastic scattering indicates four levels between 9.8 and 11.4 MeV exc. in B^{11}. The 10.32 MeV level and a new one at 11.27 MeV exc. (not shown in this figure) can be seen in the elastic scattering. This figure may be compared with Figure 25.

See text page 1.

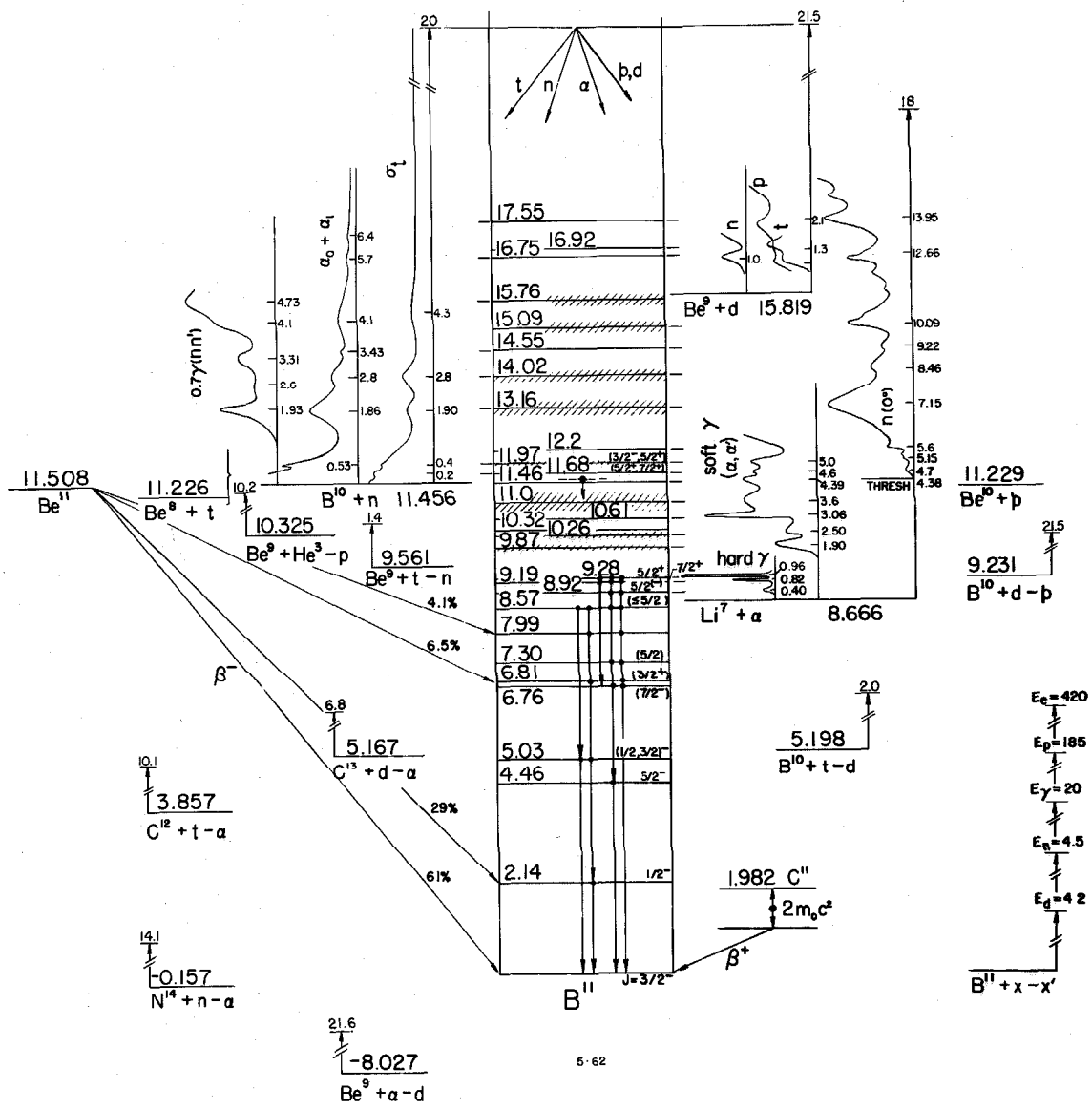
11.508
Be11
11.226
Be8 + t
10.2
10.325
Be9 + He3 − p
1.4
9.561
Be9 + t − n
B10 + n 11.456
4.1%
6.5%
β−
6.8
5.167
C13 + d − α
10.1
3.857
C12 + t − α
29%
61%
14.1
−0.157
N14 + n − α
21.6
−8.027
Be9 + α − d
17.55
16.75
16.92
15.76
15.09
14.55
14.02
13.16
12.2
11.97
11.68
11.46
11.0
10.6
10.32
10.26
9.87
9.28
9.19
8.92
8.57
7.99
7.30
6.81
6.76
5.03
4.46
2.14
B11
J=3/2−
5·62
t
n
α
p,d
Be9 + d 15.819
soft γ
(α, α′)
hard γ
Li7 + α
8.666
THRESH
11.229
Be10 + p
9.231
B10 + d − p
5.198
B10 + t − d
1.982 C11
2mec2
β+
Eα=420
Ep=185
Eγ=20
En=4.5
Ed=4.2
B11 + x − x′

Figure 1

Figure 2

We show here a schematic view of the experimental arrangement used on the 3-MeV E. S. G. to collect the data presented here below $E_{\alpha L}$ = 3.22 MeV. A similar arrangement was used at the tandem laboratory with the same cold trap extension and counter collimator.

See text pages 7 and 11.

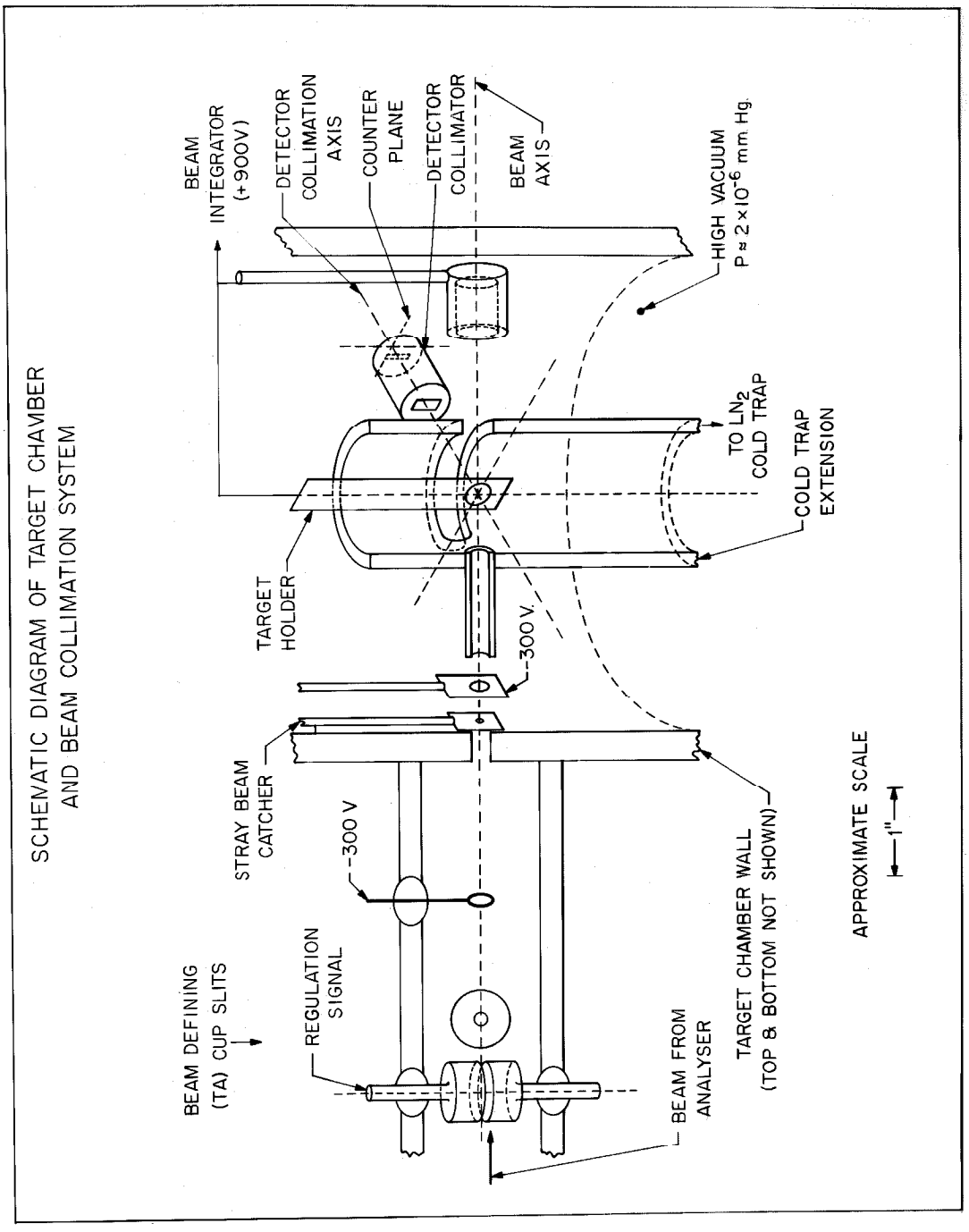
SCHEMATIC DIAGRAM OF TARGET CHAMBER
AND BEAM COLLIMATION SYSTEM
BEAM INTEGRATOR (+900V)
DETECTOR COLLIMATION AXIS
COUNTER PLANE
DETECTOR COLLIMATOR
BEAM AXIS
HIGH VACUUM P ≈ 2×10⁻⁶ mm Hg
TO LN2 COLD TRAP
COLD TRAP EXTENSION
TARGET HOLDER
-300 V.
STRAY BEAM CATCHER
-300 V
REGULATION SIGNAL
BEAM DEFINING (TA) CUP SLITS
BEAM FROM ANALYSER
TARGET CHAMBER WALL (TOP & BOTTOM NOT SHOWN)
APPROXIMATE SCALE
1"

Figure 2

Figure 3

This figure was obtained by measuring the deexcitation γ-ray yield curve for the reaction $Li^7(\alpha, \alpha')Li^{7*}(.48)$. The normalization is that of Li and Sherr[4]. The error bars on the data indicate the statistical counting and background subtraction errors. The Li^7F target used was approximately 40 keV thick for 3 MeV alpha particles.

See text pages 16 and 34.

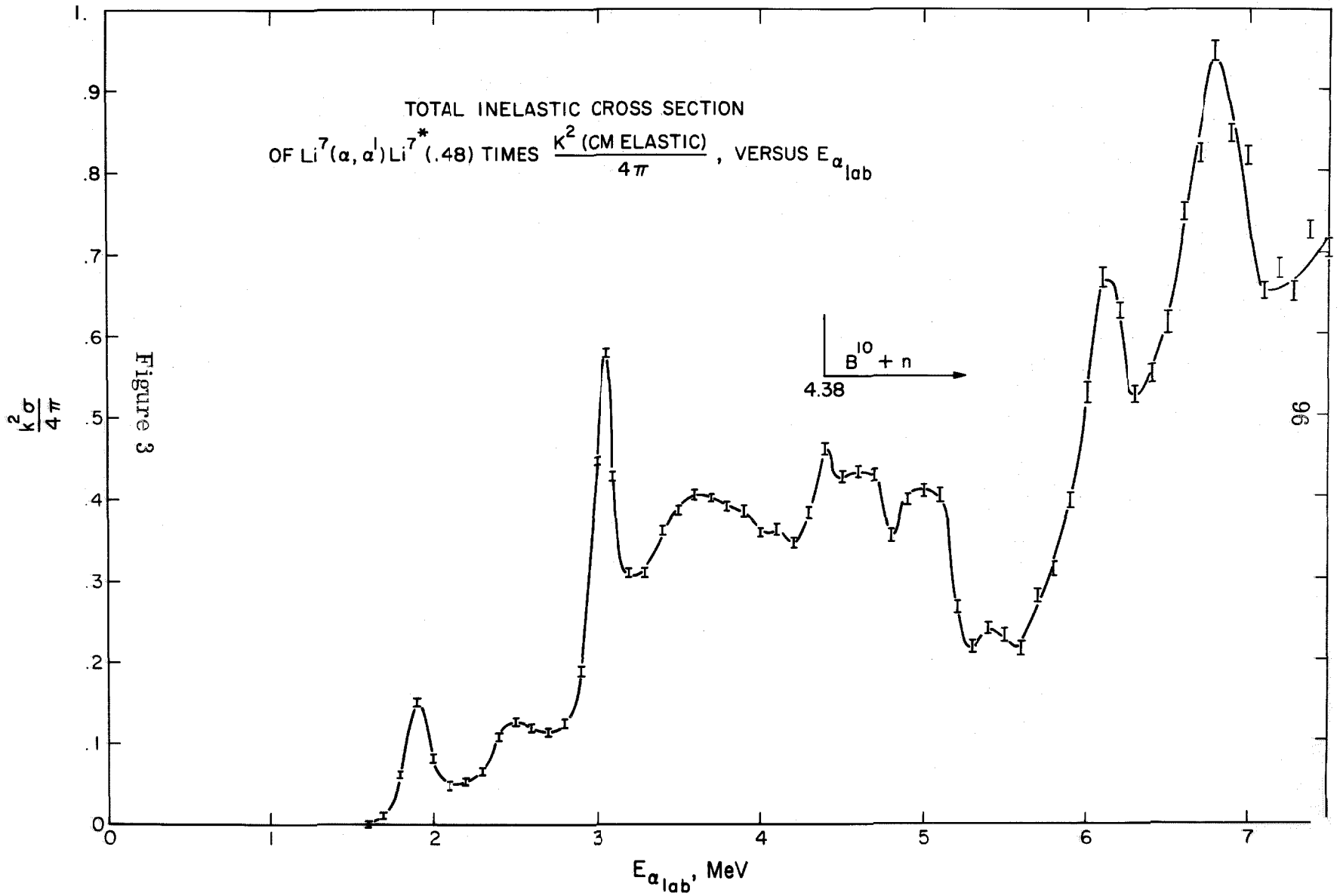
TOTAL INELASTIC CROSS SECTION
OF $Li^7(\alpha, \alpha')Li^{7*}$ (.48) TIMES $\frac{K^2 \text{ (CM ELASTIC)}}{4\pi}$, VERSUS $E_{\alpha_{lab}}$
$B^{10} + n$
4.38
$\frac{k^2\sigma}{4\pi}$
$E_{\alpha_{lab}}$, MeV
0
1
2
3
4
5
6
7
.1
.2
.3
.4
.5
.6
.7
.8
.9
1.

Figure 3

Figure 4

In this calculation we have taken the values of the energy loss for protons in H, Li^7, C^{12}, O^{16} from the tables of Whaling[37]. From these values we have calculated the energy loss of alpha particles in the compounds shown, using the formulae (II-1) and (II-2) given in the text. The value of the specific energy loss or stopping cross section in keV-$cm^2 \times 10^{-18}$ has the same units as the ordinate of the graph. The dotted lines for the lower energy portion of the graph indicate that the calculation, there, may be uncertain due to possible errors in our estimate of $\overline{Z^2}$. A measurement at 700 keV indicates a higher value for ΔE, in a Li^7OH target, than that predicted by the calculation.

See text page 9.

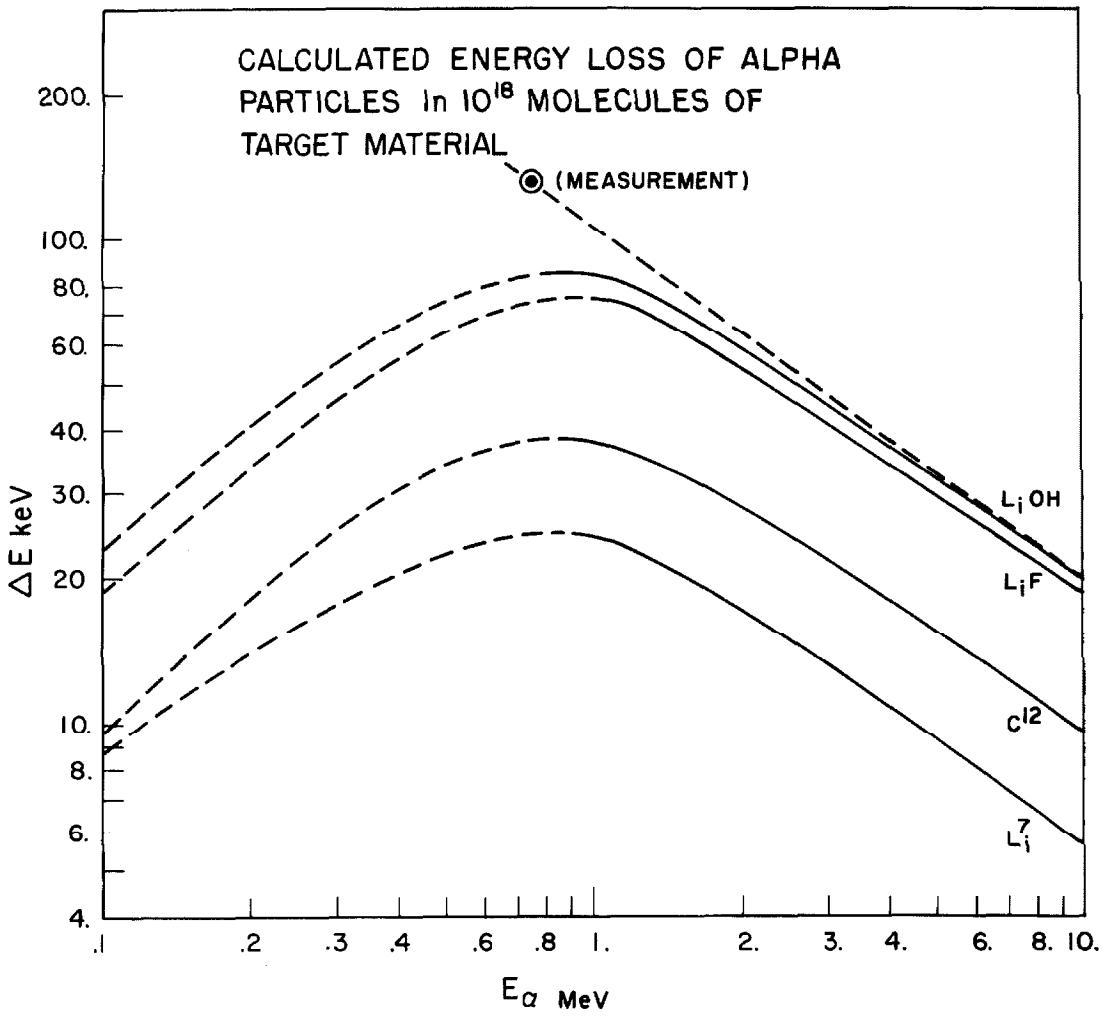
CALCULATED ENERGY LOSS OF ALPHA
PARTICLES In 10^{18} MOLECULES OF
TARGET MATERIAL
(MEASUREMENT)
200.
100.
80.
60.
40.
30.
20
10.
8.
6.
4.
ΔE keV
.1
.2
.3
.4
.6
.8
1.
2.
3.
4.
6.
8.
10.
E_α MeV
L_iOH
L_iF
C^{12}
L_i^7

Figure 4

Figure 5

We present here a spectrum showing the various contaminants in our targets, due mostly to the release agent used in the fabrication of the target foils (Duponol C). One may also notice the low energy rising background. This background was shown to be due to low energy ionizing particles (alphas or carbon recoils) and puts a lower limit to the energy of the alpha particles that can be detected. The small peak labelled L_i^7 may be due to a residual lithium contamination of the apparatus used in the fabrication of the foil, since this apparatus was also used to make lithium-bearing foils. No lithium or lithium salts were evaporated on this foil.

See text page 10.

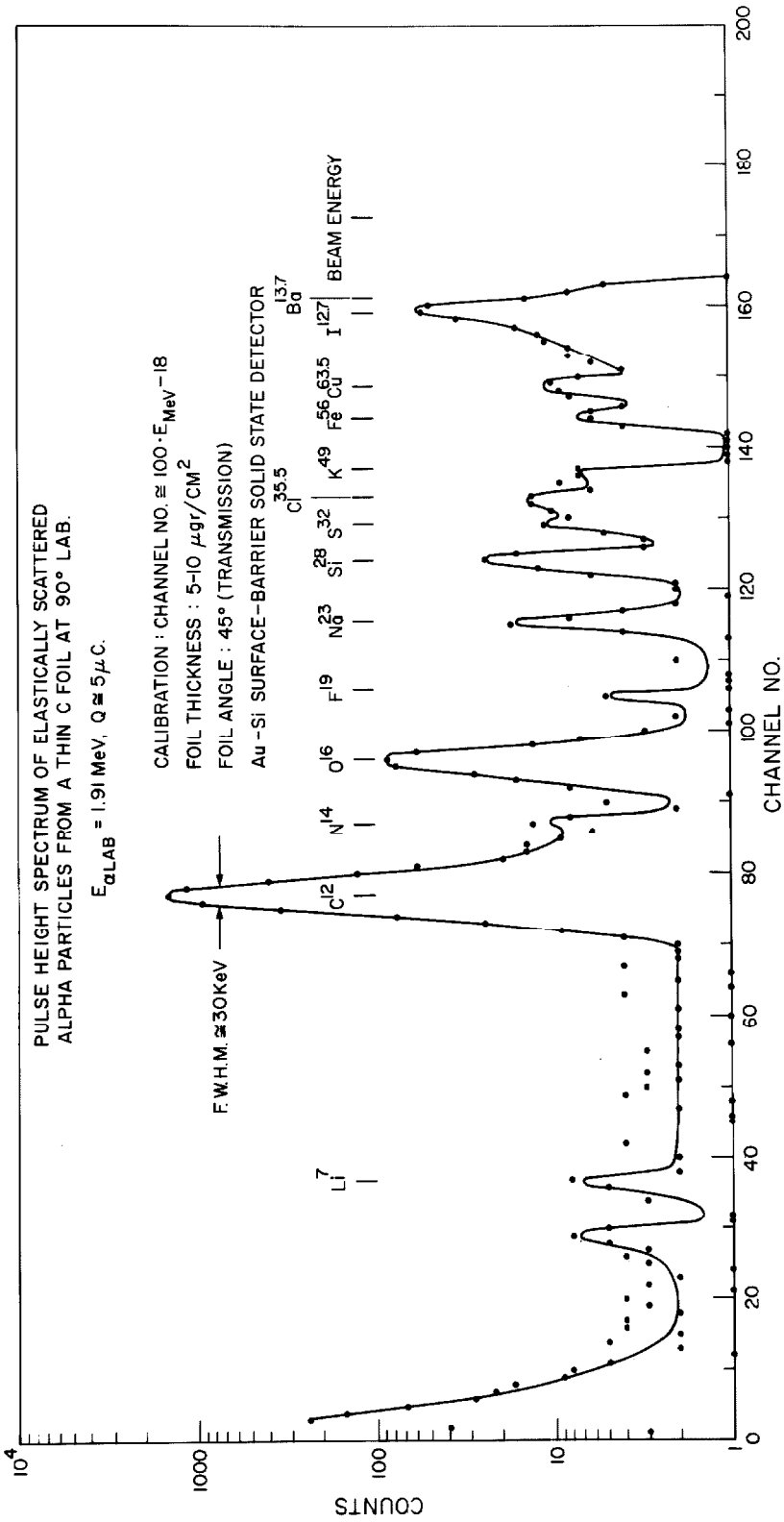
PULSE HEIGHT SPECTRUM OF ELASTICALLY SCATTERED
ALPHA PARTICLES FROM A THIN C FOIL AT 90° LAB.
$E_{\alpha LAB}$ = 1.91 MeV, Q ≅ 5μC.
CALIBRATION : CHANNEL NO. ≅ 100·E_{MeV} − 18
FOIL THICKNESS : 5-10 μgr/CM²
FOIL ANGLE : 45° (TRANSMISSION)
Au -Si SURFACE-BARRIER SOLID STATE DETECTOR
F.W.H.M. ≅ 30KeV
Li^{7}
C^{12}
N^{14}
O^{16}
F^{19}
Na^{23}
Si^{28}
S^{32}
$Cl^{35.5}$
K^{49}
Fe^{56}
$Cu^{63.5}$
I^{127}
Ba^{137}
BEAM ENERGY
COUNTS
CHANNEL NO.
10^4
1000
100
10
1
0
20
40
60
80
100
120
140
160
180
200

Figure 5

Figure 6

This profile was obtained to exhibit more clearly the energy distribution of the particles scattered from a thin foil at low energy. The front edge of the profile can be well understood from the known properties of the magnetic spectrometer. The back edge is broadened by the straggling effect and the non uniformity of the target thickness. The value of the stopping cross section deduced from this profile, agrees, within experimental uncertainties, with the calculated value.

See text page 11.

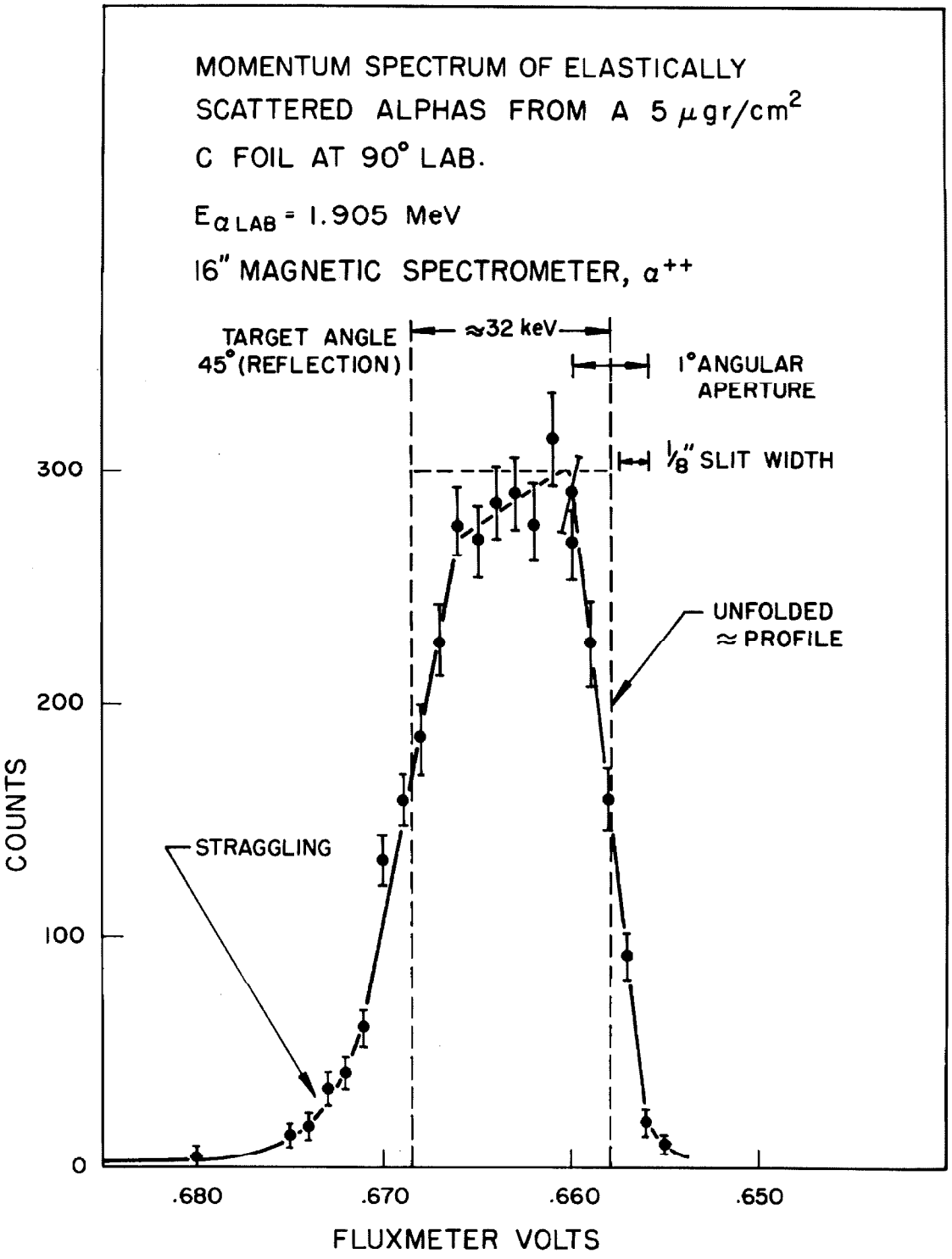
MOMENTUM SPECTRUM OF ELASTICALLY
SCATTERED ALPHAS FROM A 5 μgr/cm²
C FOIL AT 90° LAB.
Eα LAB = 1.905 MeV
16" MAGNETIC SPECTROMETER, α++
TARGET ANGLE
45° (REFLECTION)
≈32 keV
1° ANGULAR
APERTURE
1/8" SLIT WIDTH
UNFOLDED
≈ PROFILE
STRAGGLING
COUNTS
300
200
100
0
.680
.670
.660
.650
FLUXMETER VOLTS

Figure 6

Figure 7

This profile was obtained under conditions similar to those used in obtaining the profile shown in Figure 6. The small number of counts shows the effect of a higher $\partial E/\partial \theta$ and dE/dx in this case, as compared with Figure 6. The energy width of this profile is about 180 keV.

See text page 11.

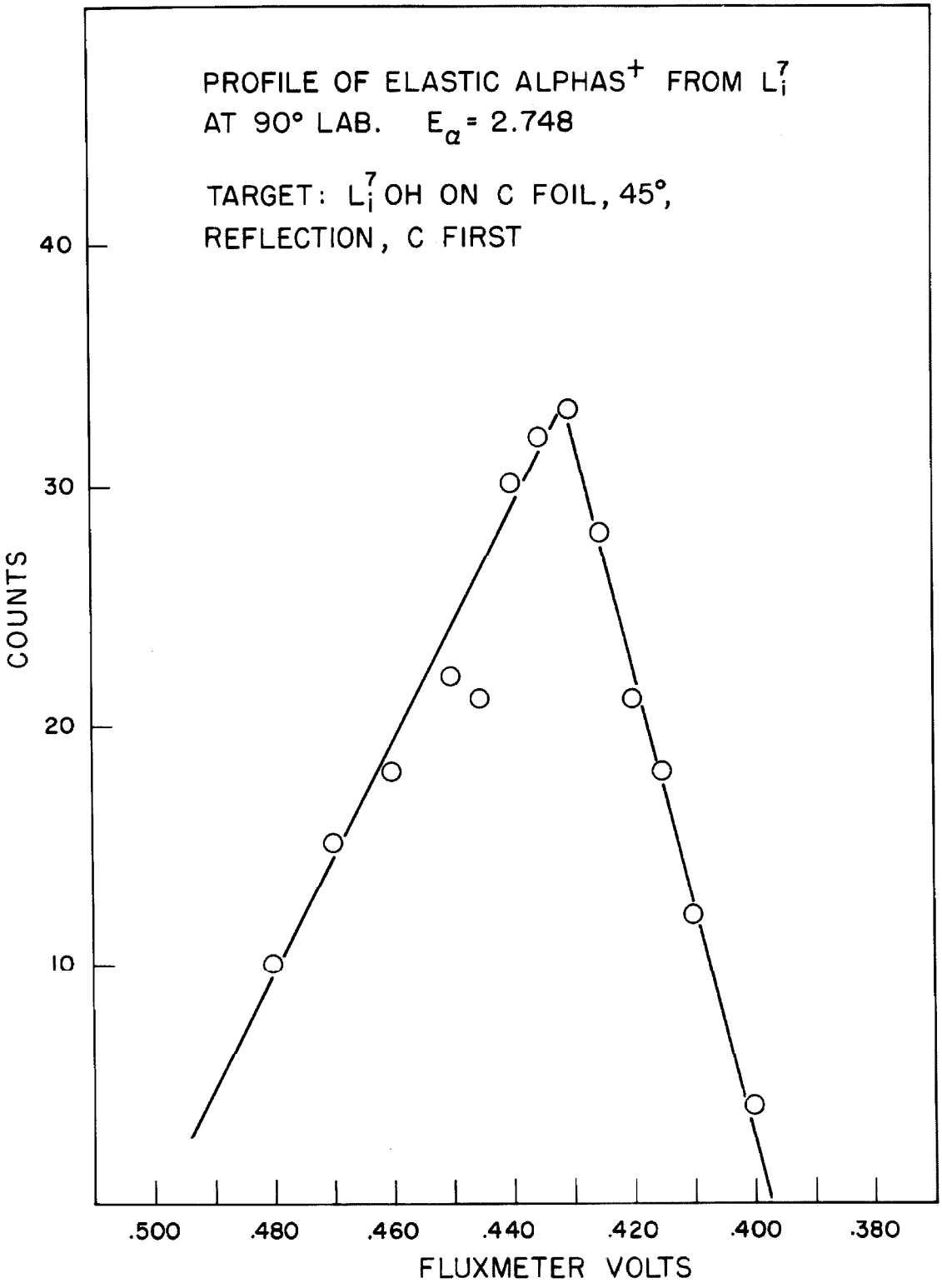
PROFILE OF ELASTIC ALPHAS+ FROM L_i^7
AT 90° LAB. E_α = 2.748
TARGET: L_i^7OH ON C FOIL, 45°,
REFLECTION, C FIRST
COUNTS
40
30
20
10
.500
.480
.460
.440
.420
.400
.380
FLUXMETER VOLTS

Figure 7

Figure 8

We illustrate here the target deterioration which takes place after about 1000 microcoulombs of bombardment on the same spot, when the target is not protected with a cold trap extension as shown in Figure 2. The energy loss of alphas traversing the L_i^7OH plus contaminants is 96 keV. Of this energy loss, about 36 keV is contributed by the incident beam and the rest by the lower energy scattered beam.

See text page 11.

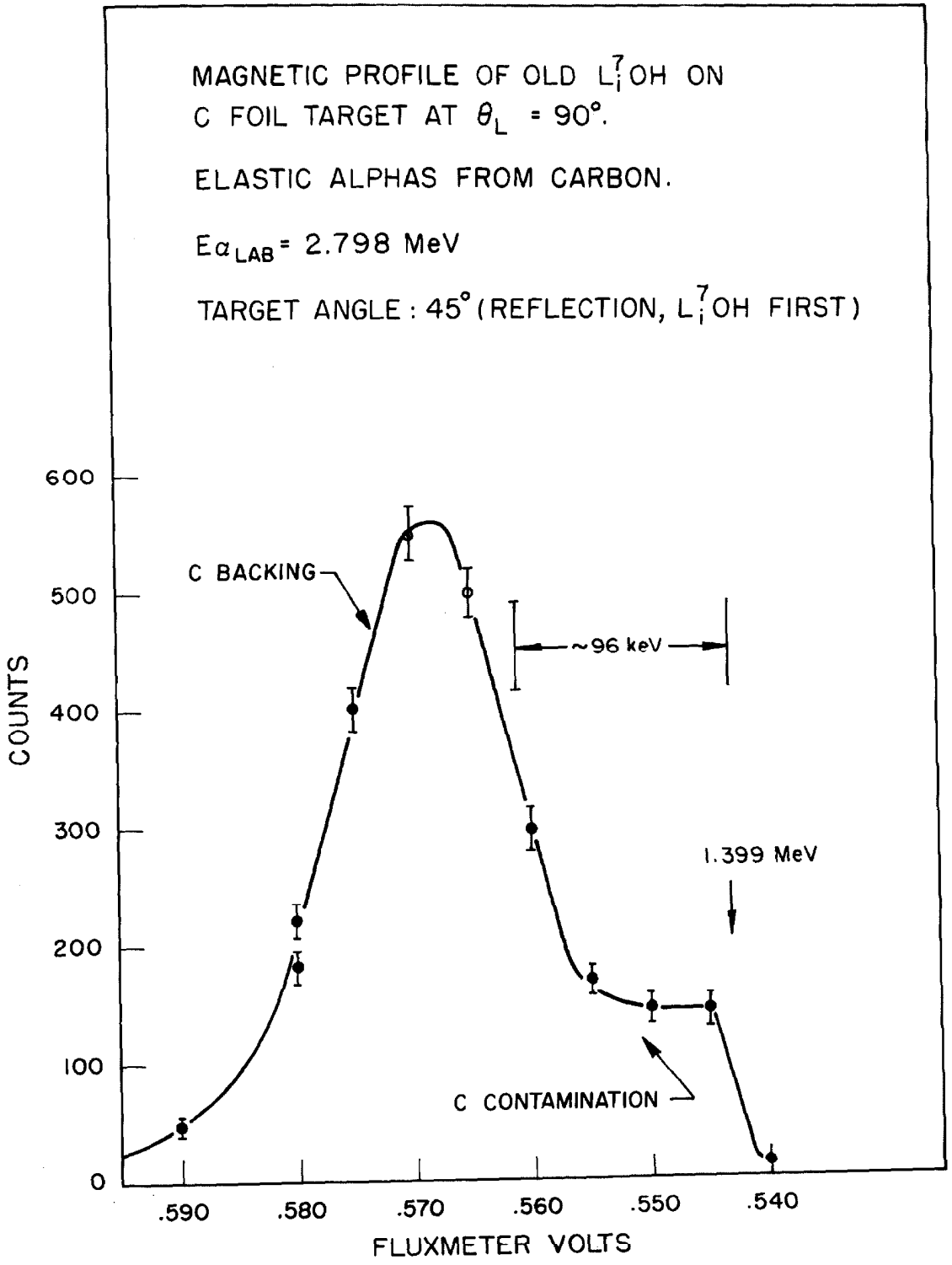
MAGNETIC PROFILE OF OLD L_i^7OH ON
C FOIL TARGET AT θ_L = 90°.
ELASTIC ALPHAS FROM CARBON.
$E\alpha_{LAB}$ = 2.798 MeV
TARGET ANGLE : 45° (REFLECTION, L_i^7OH FIRST)
C BACKING
~96 keV
1.399 MeV
C CONTAMINATION
COUNTS
600
500
400
300
200
100
0
.590
.580
.570
.560
.550
.540
FLUXMETER VOLTS

Figure 3

Figure 9

Assuming that a plot of the specific energy loss of the incident beam of particles in the target vs the distance inside the target has a rectangular shape, we have computed the yield from such a target, as the incident energy is varied over a resonance. We have assumed that, in the limit where the target thickness is zero, the yield curve has a Breit-Wigner shape. By simply changing the target angle with respect to the beam, one changes the target thickness. Curves 2 and 3 were found to be consistent with the observed yield over the 10.60 MeV resonance in B^{11}.

See text page 12.

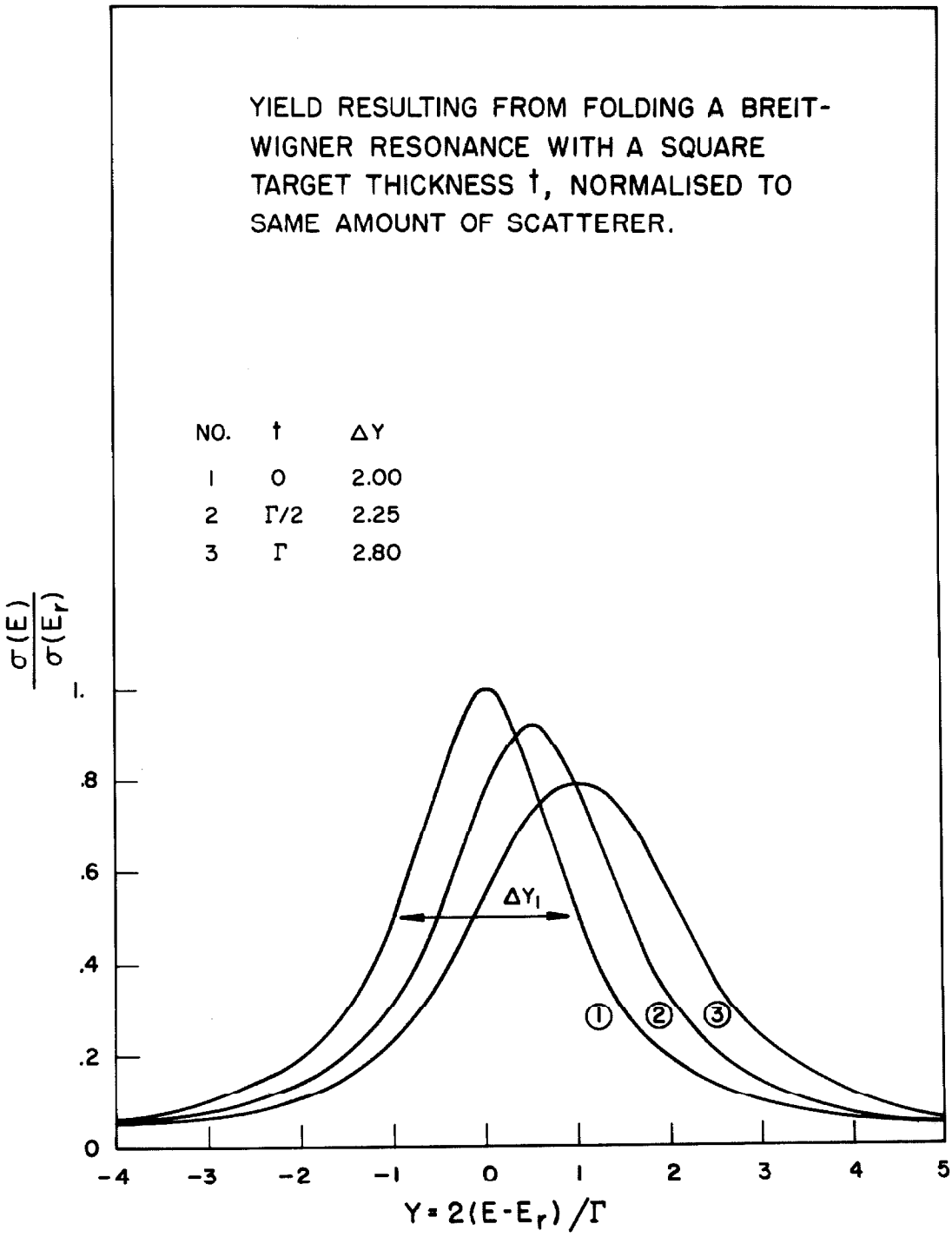
YIELD RESULTING FROM FOLDING A BREIT-WIGNER RESONANCE WITH A SQUARE TARGET THICKNESS t, NORMALISED TO SAME AMOUNT OF SCATTERER.
NO. t ΔY
1 0 2.00
2 Γ/2 2.25
3 Γ 2.80
σ(E)/σ(Er)
1.
.8
.6
.4
.2
0
ΔY1
①
②
③
-4 -3 -2 -1 0 1 2 3 4 5
Y = 2(E-Er)/Γ

Figure 9

Figure 10

We see here a good spectrum of alpha particles from which useable data was extracted. The spectrum shown here was used to obtain the points shown in Figures 14 and 18, at $\theta_{C.M.} = 90^{o}$ and $E_{\alpha L} = 2.97$ MeV. At backward and forward angles, the alpha groups from Li^{7} were not so well isolated and the background subtraction was not quite so obvious.

See text pages 13 and 15.

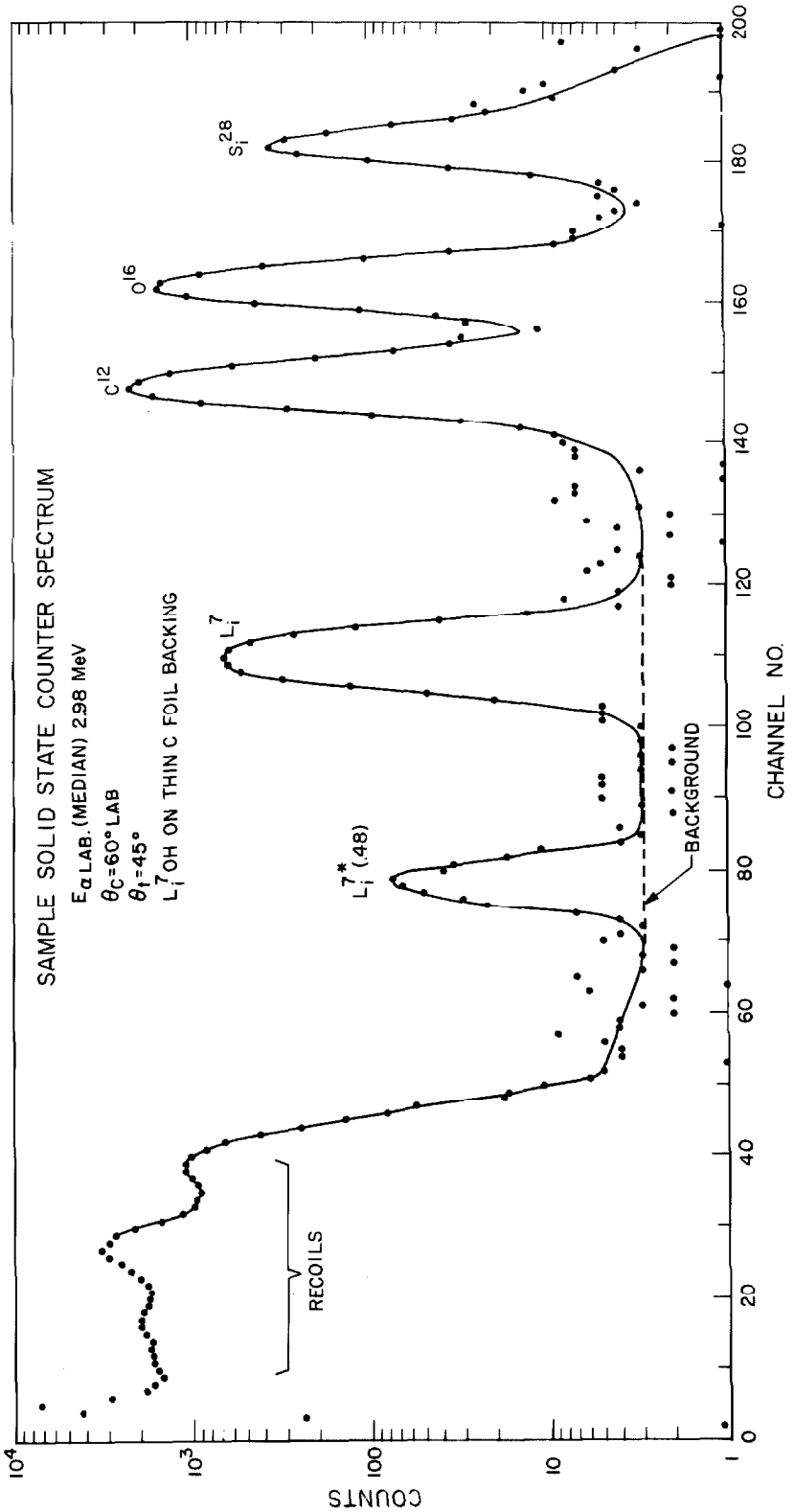
SAMPLE SOLID STATE COUNTER SPECTRUM
$E_{\alpha\,LAB.}$ (MEDIAN) 2.98 MeV
θ_C=60° LAB
θ_{Li}=45°
Li^7OH ON THIN C FOIL BACKING
C^{12}
O^{16}
Si^{28}
Li^7
Li^{7*} (.48)
BACKGROUND
RECOILS
COUNTS
CHANNEL NO.
10^4
10^3
100
10
1
0
20
40
60
80
100
120
140
160
180
200

Figure 10

Figure 11

Elastic Differential Cross Section Times the C. M. Wave Number Squared, for Alphas on L_i^7

This yield curve represents a smoothed average of several measurements, taken with various energy steps, sometimes as small as 20 keV. The scatter of the points, from which this curve was drawn, was less than 5%. The numbered energies correspond to entries in Table III where we have listed all the scattering anomalies observed in this experiment. Some of the listed anomalies are not visible in this graph. They have been observed in other yield curves as explained in the text.

See text pages 16 and 24.

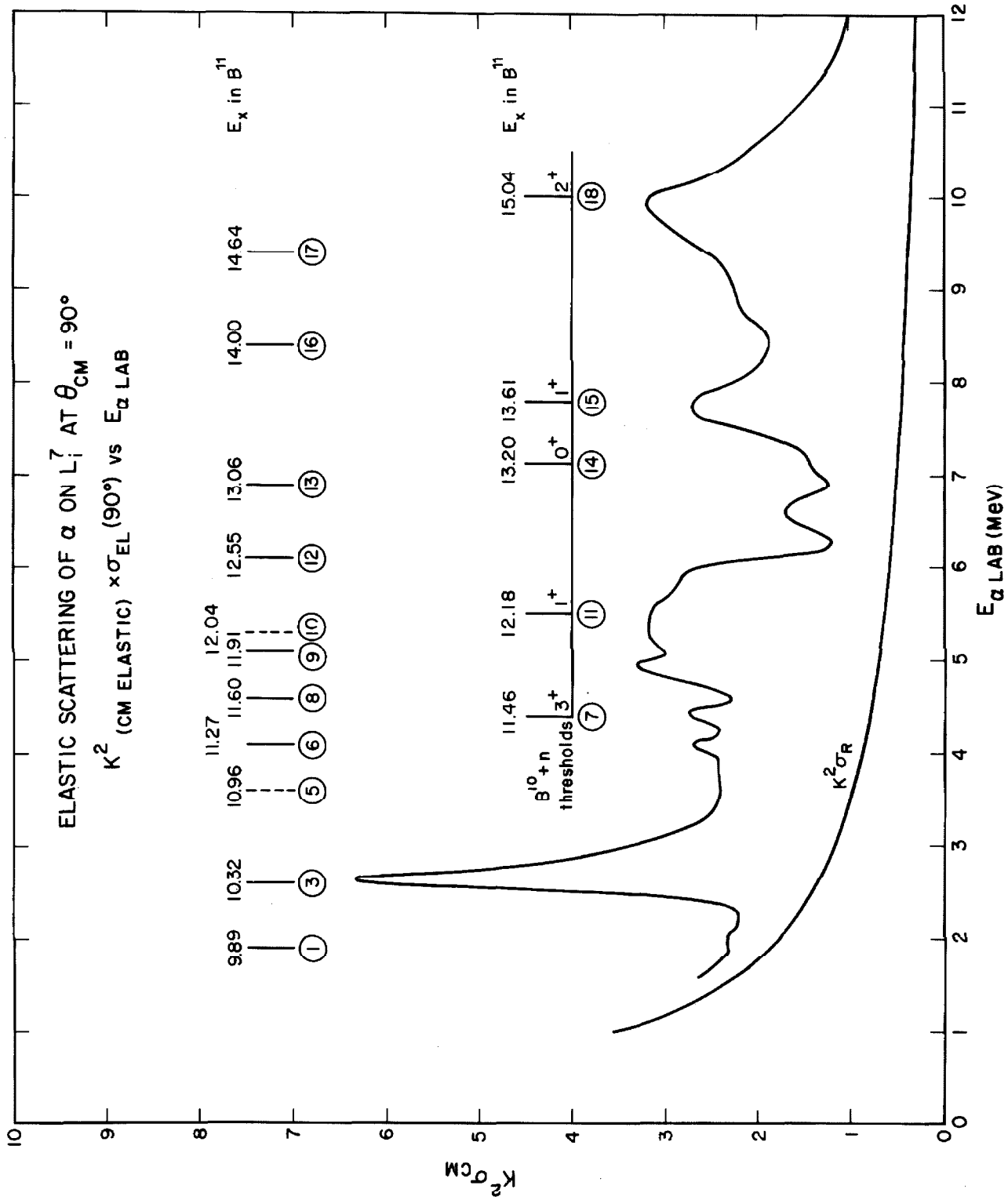
ELASTIC SCATTERING OF α ON L_i^7 AT θ_{CM} = 90°
K^2 (CM ELASTIC) ×σ_{EL}(90°) vs E_α LAB
$K^2\sigma_{CM}$
E_α LAB (MeV)
$K^2\sigma_R$
E_x in B^{11}
9.89
10.32
10.96
11.27
11.60
11.91
12.04
12.55
13.06
14.00
14.64
11.46
12.18
13.20
13.61
15.04
3^+
1^+
0^+
1^+
2^+
B^{10} + n thresholds

Figure 11

Figure 12

Inelastic Differential Cross Section of Alphas on L_i^7, Times k^2, the C. M. Wave Number Squared

This yield curve was obtained in the same way as Figure 11. Here, only anomalies number 3, 8, 10, 11, 14 are not visible. The quantity $k^2\sigma$ is plotted here again to make the units dimensionless and to remove some of the kinematical energy dependence.

See text pages 16 and 24.

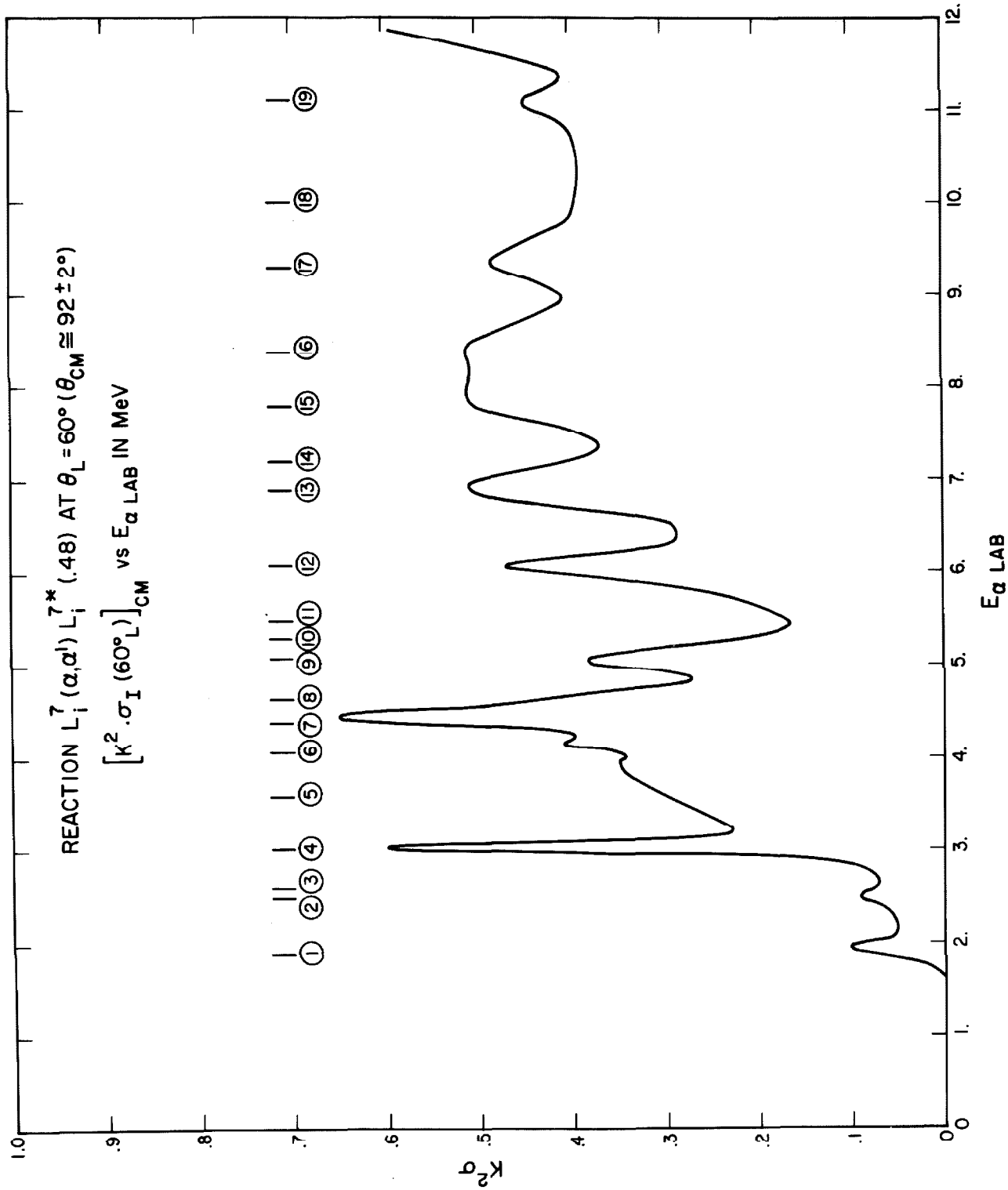
REACTION $L_i^7(\alpha,\alpha')L_i^{7*}(.48)$ AT $\theta_L = 60°$ ($\theta_{CM} \cong 92 \pm 2°$)
$[K^2 \cdot \sigma_I(60°_L)]_{CM}$ vs $E_{\alpha\ LAB}$ IN MeV
$K^2\sigma$
$E_{\alpha\ LAB}$
1.0
.9
.8
.7
.6
.5
.4
.3
.2
.1
0
1.
2.
3.
4.
5.
6.
7.
8.
9.
10.
11.
12.
① ② ③ ④ ⑤ ⑥ ⑦ ⑧ ⑨ ⑩ ⑪ ⑫ ⑬ ⑭ ⑮ ⑯ ⑰ ⑱ ⑲

Figure 12

Figure 13

The solid line shown here was taken from Figure 3. The experimental inelastic angular distributions (some of which are shown in Figure 14) were analyzed in series of Legendre polynomials. The overall normalization coefficient of all of these angular distributions was adjusted to make the coefficients of the P_0 term agree as well as possible with the solid curve. This adjustment provided us with the absolute normalization for the entire experiment. The error bars in the figure represent the fluctuations of the coefficient of P_0 as the number of fitting polynomials was increased from one to seven.

See text page 17.

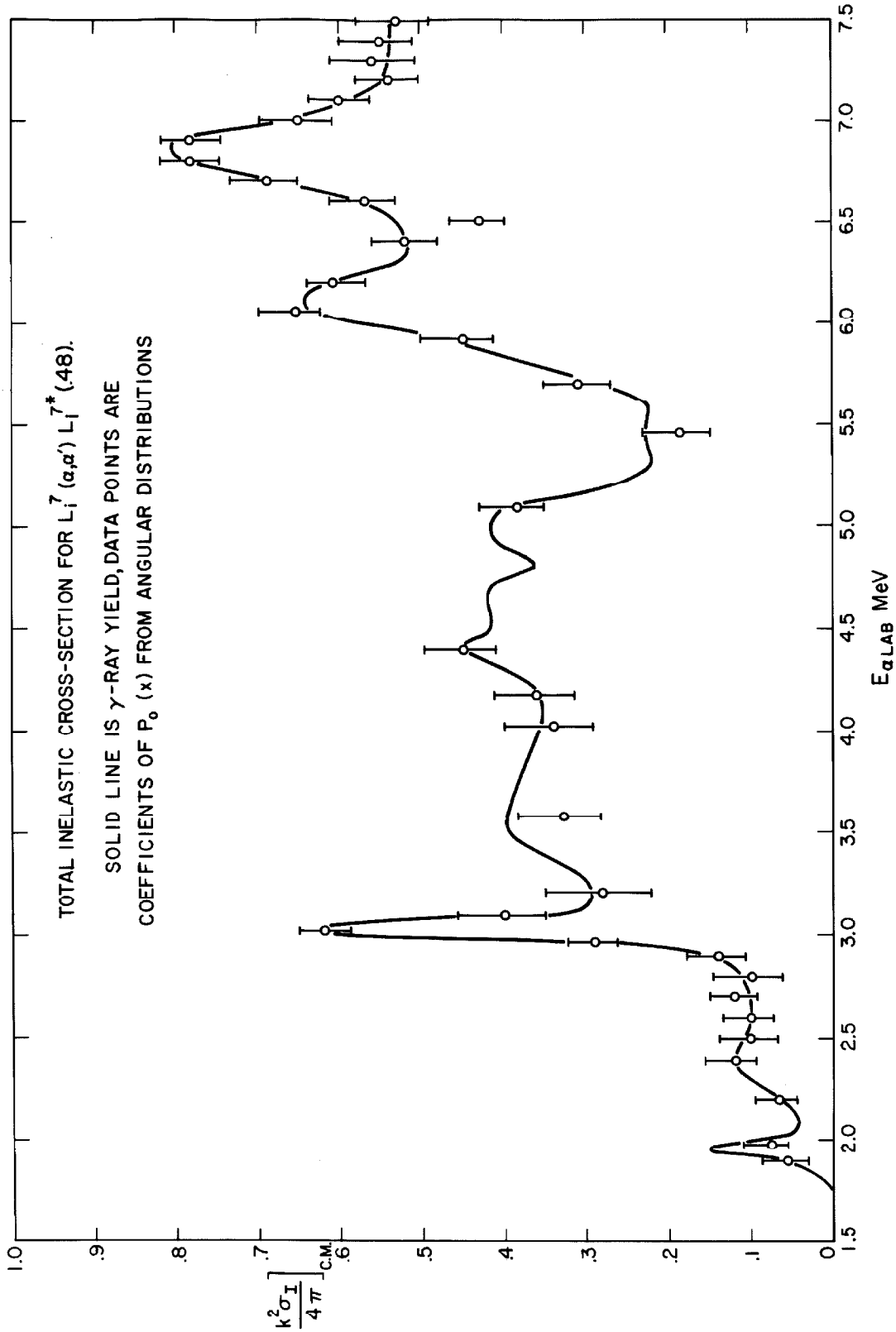
TOTAL INELASTIC CROSS-SECTION FOR L_i^7 (α,α') L_i^{7*}(.48).
SOLID LINE IS γ-RAY YIELD, DATA POINTS ARE
COEFFICIENTS OF P_o (x) FROM ANGULAR DISTRIBUTIONS
$\left[\frac{k^2\sigma_I}{4\pi}\right]_{C.M.}$
$E_{\alpha LAB}$ MeV
1.0
.9
.8
.7
.6
.5
.4
.3
.2
.1
0
1.5
2.0
2.5
3.0
3.5
4.0
4.5
5.0
5.5
6.0
6.5
7.0
7.5

Figure 13

Figure 14

Dimensionless Inelastic Differential Cross Section for $L_i^7(\alpha, \alpha')L_i^{7*}(.48)$

We show here several typical inelastic angular distributions. To provide an estimate of the accuracy with which such data were obtained, two distributions were taken at $E_{\alpha L} = 6.40$ MeV and analysed independently. The results are shown in the figure. Above $E_{\alpha L} = 4.39$ MeV, all the inelastic angular distributions show more or less pronounced minima near $\theta_{C.M.} = 60$ and 120^{o}. This might be due to a direct interaction contribution to the inelastic cross section.

See text page 37.

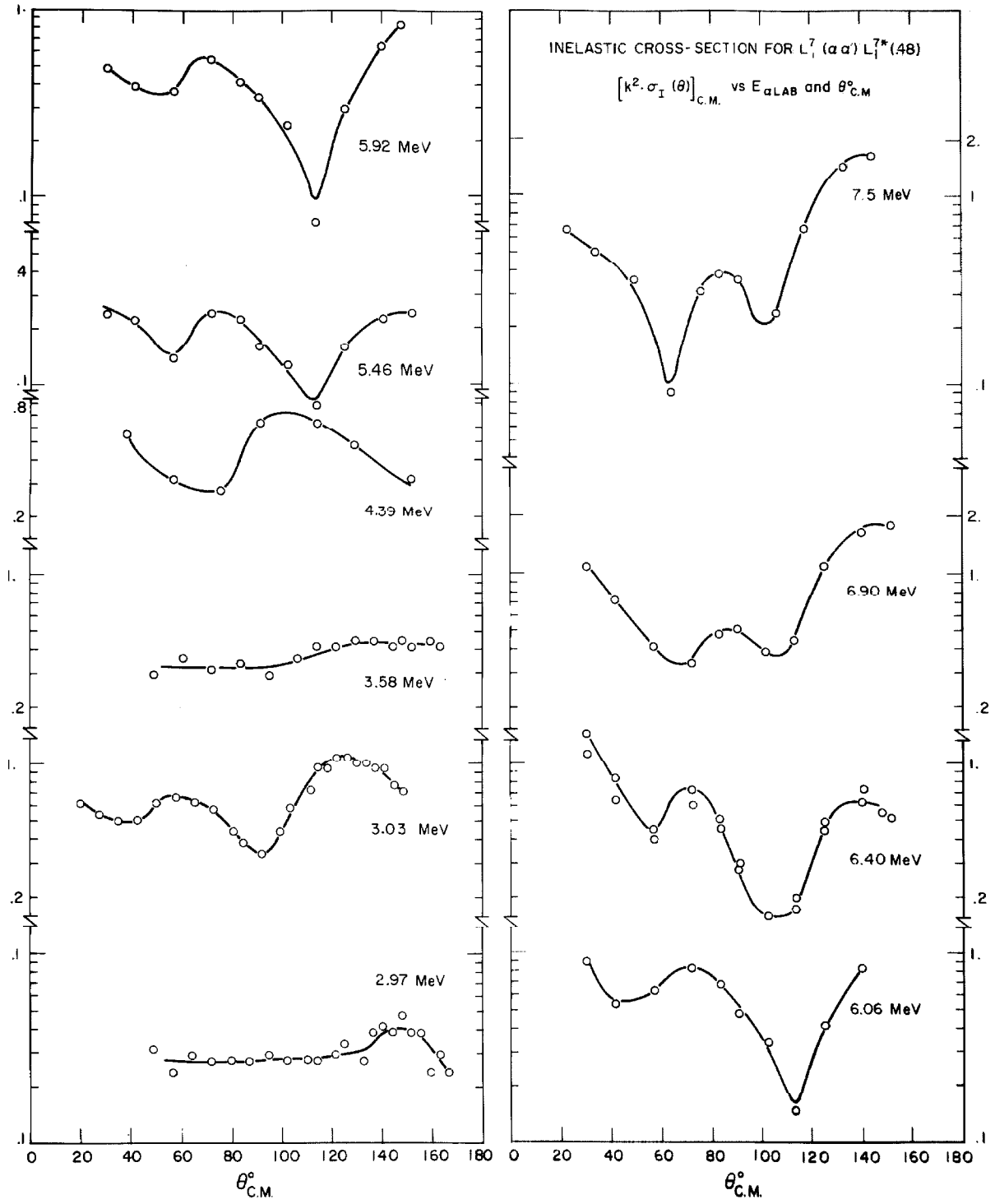
INELASTIC CROSS-SECTION FOR L_1^7 (α,α') $L_1^{7*}(.48)$
$[k^2 \cdot \sigma_I(\theta)]_{C.M.}$ vs $E_{\alpha LAB}$ and $\theta^\circ_{C.M.}$
5.92 MeV
5.46 MeV
4.39 MeV
3.58 MeV
3.03 MeV
2.97 MeV
7.5 MeV
6.90 MeV
6.40 MeV
6.06 MeV
0 20 40 60 80 100 120 140 160 180
$\theta^\circ_{C.M.}$

Figure 14

Figure 15

The penetration factor plotted here is dimensionless. For a narrow resonance involving one L value, the width is given by

$$\Gamma = 2P_L \gamma_L^2 ,$$

$$\gamma_L^2 = \frac{\hbar^2}{MR_o^2} \theta^2 ,$$

where $\frac{\hbar^2}{MR_o^2} = 0.451$ MeV in this case. θ^2 is dimensionless and equal to one for a square well. The energy scale is given for the elastic channel. One must subtract 0.752 MeV from the energy in the elastic channel to find the energy in the inelastic channel at which the inelastic penetration factor is to be evaluated.

See text pages 16 and 28.

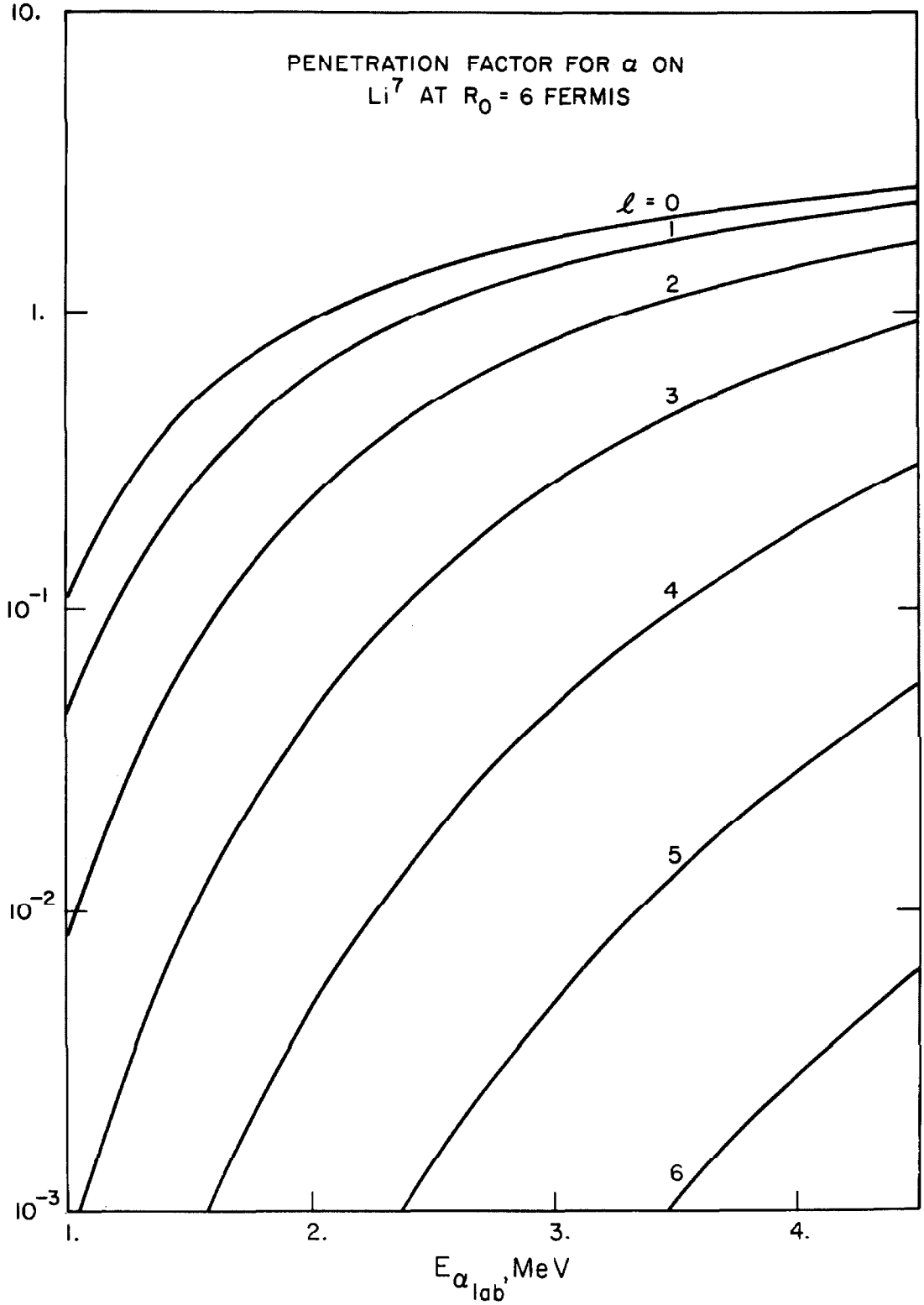
PENETRATION FACTOR FOR α ON
Li7 AT R0 = 6 FERMIS
ℓ = 0
1
2
3
4
5
6
10.
1.
10-1
10-2
10-3
1.
2.
3.
4.
Eα lab, MeV

Figure 15

Figure 16

Measured Dimensionless Differential Elastic Cross Section at $\theta_{C.M.} = 159^{o}$

This figure gives the elastic cross section at the largest C. M. angle for which reliable data could be obtained, for all energies down to $E_{\alpha L} = 1.6$ MeV. The values of the cross section were obtained from the smoothed elastic angular distributions shown in Figures 17-19. The curve was completed by doing an excitation function at this angle, in steps of 40 keV. The first six anomalies were fitted using a multilevel R-matrix model-program. The seventh occurs near the threshold for B^{10} + n and was not fitted for this reason.

See text page 24.

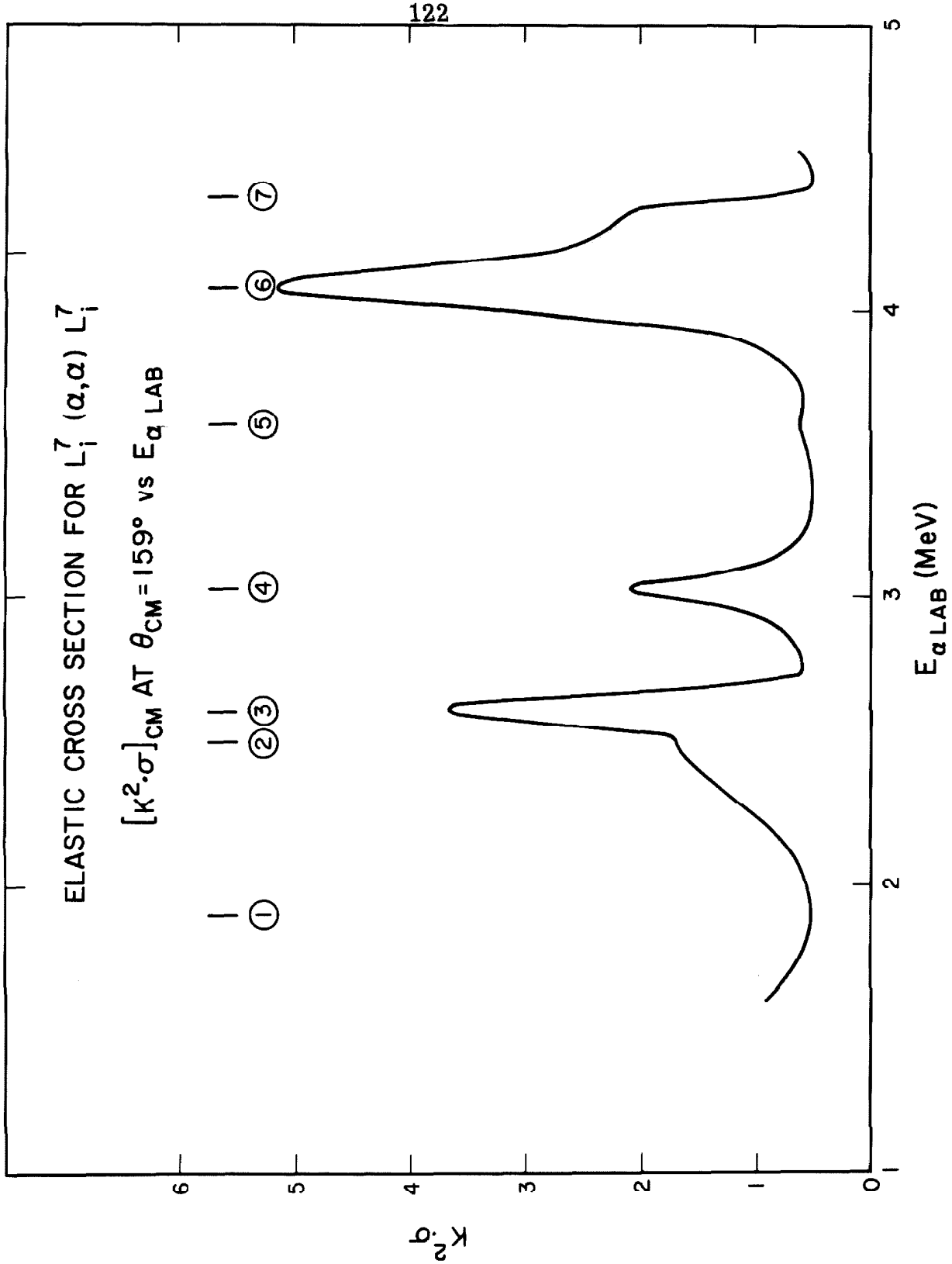
ELASTIC CROSS SECTION FOR L_i^7 (α,α) L_i^7
$[K^2.\sigma]_{CM}$ AT θ_{CM}=159° vs $E_{\alpha\ LAB}$
①
②③
④
⑤
⑥
⑦
$K^2.\sigma$
$E_{\alpha\ LAB}$ (MeV)
0
1
2
3
4
5
6

Figure 1

Figure 17

Elastic Differential Cross Sections for $L_i^7(\alpha, \alpha)L_i^7$, for Various Laboratory Energies

These angular distributions were obtained by measuring the cross section at intervals of 10^0 in the laboratory system, starting at forward angles and going towards backward angles. The process was then reversed, but this time the selected angles were taken between the previous ones, to check on target depletion. The solid lines are the results of a least squares fit to the data using Legendre polynomials up to P_6. Although the fits are good, the numerical values of the coefficients were not meaningful, being sometimes too large by a factor of 10^5. The excellent fit seen here is thus the result of taking the difference (which should be of order 1) of functions which are very large.

See text page 14.

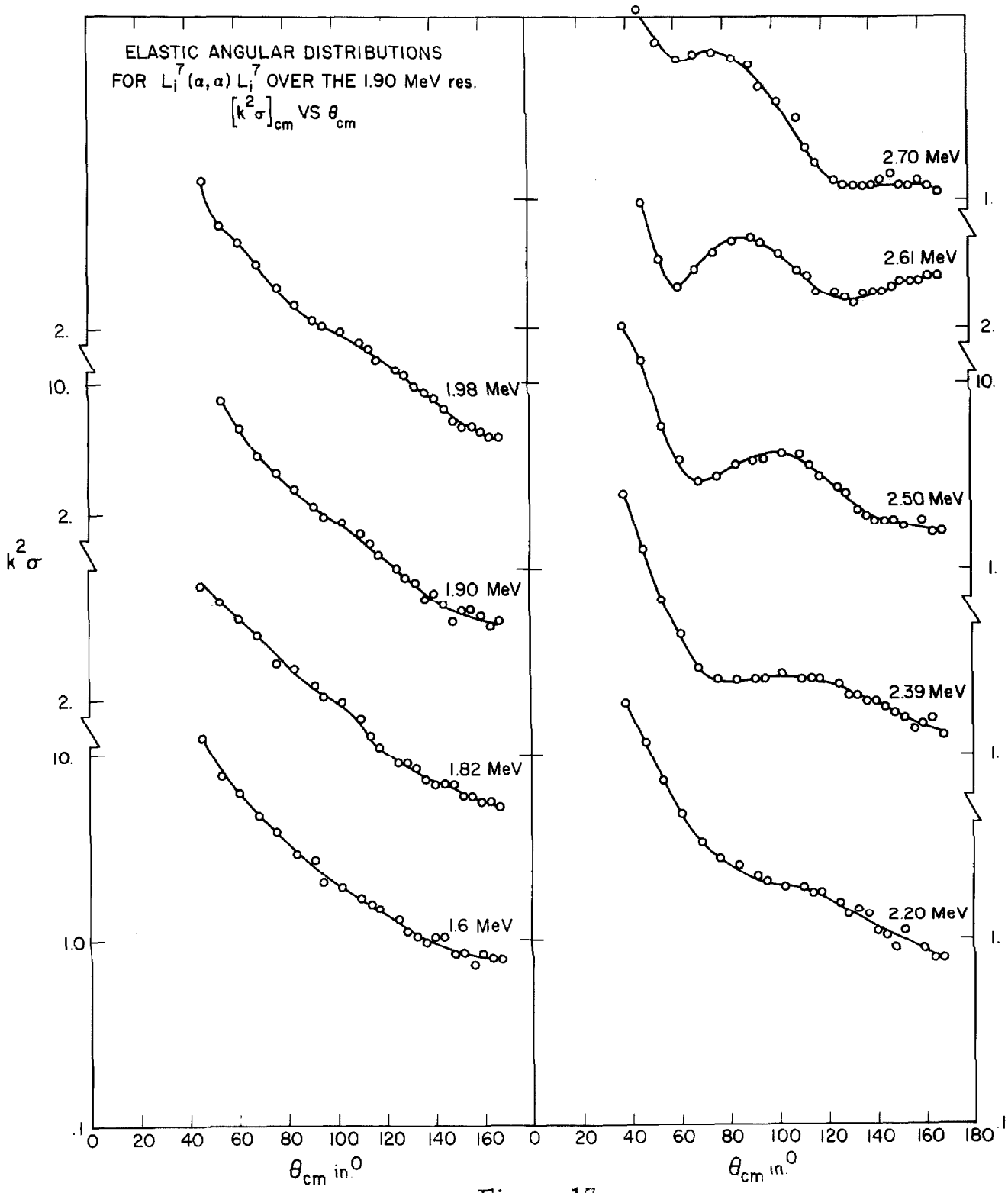
ELASTIC ANGULAR DISTRIBUTIONS
FOR $Li^7(\alpha,\alpha)Li^7$ OVER THE 1.90 MeV res.
$[k^2\sigma]_{cm}$ VS θ_{cm}
$k^2\sigma$
1.98 MeV
1.90 MeV
1.82 MeV
1.6 MeV
2.70 MeV
2.61 MeV
2.50 MeV
2.39 MeV
2.20 MeV
θ_{cm} in ^{0}
θ_{cm} in ^{0}

Figure 17

Figure 18

Elastic Differential Cross Sections for $L_i^7(\alpha, \alpha)L_i^7$

The comments made for Figure 17 also apply to all the angular distributions presented in this work. In addition, we may draw attention to the pronounced anomaly at backward angles, centered at 3.03 MeV. At $\theta_{C.M.} = 140.8^{o}$, a zero of $P_3(\cos\theta)$, the anomaly vanishes, thus indicating an L = 3 resonance in B^{11}. The assignment $J^{\pi} = 7/2^{+}$ is proposed in the text for this level.

See text pages 14 and 33.

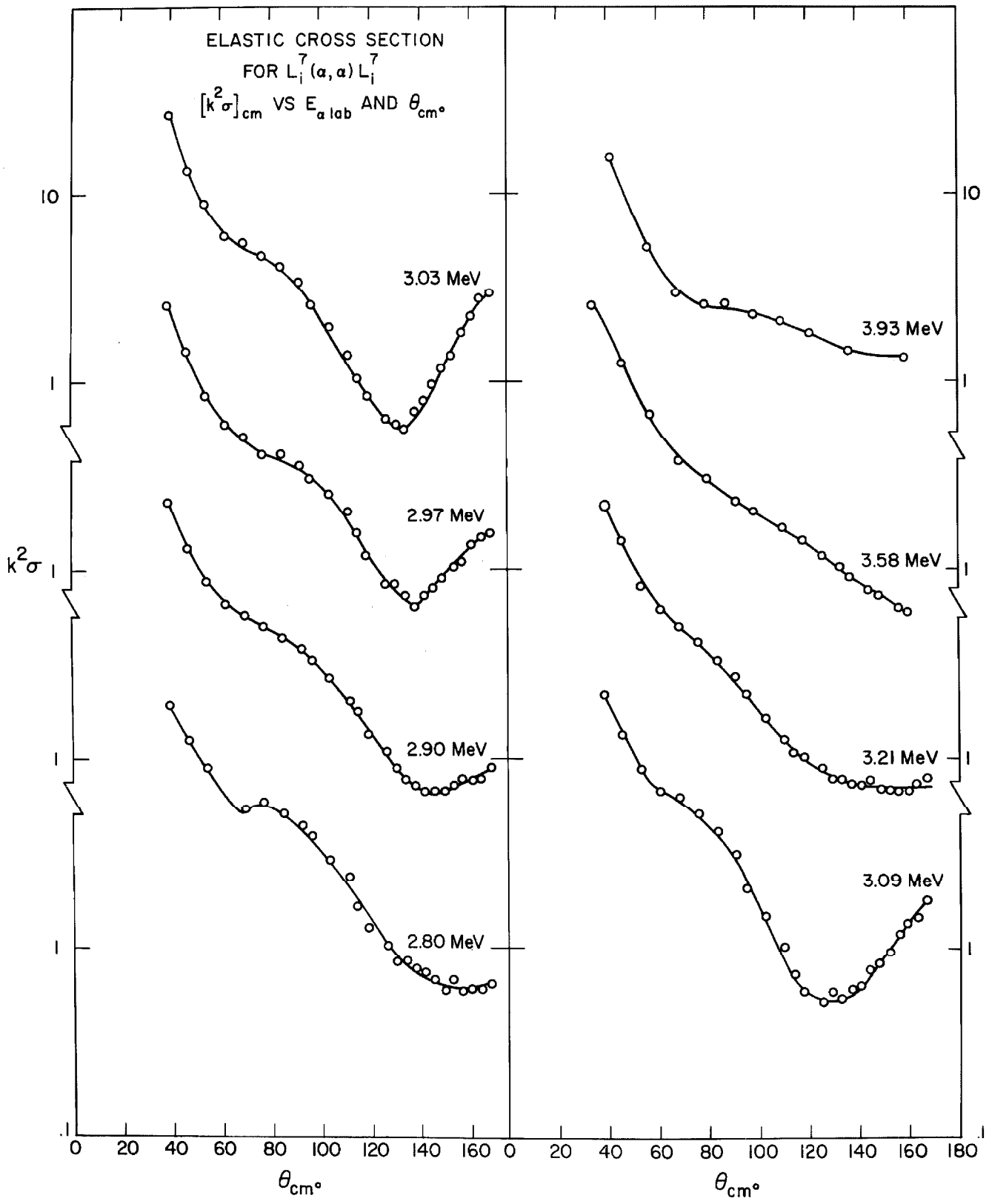
ELASTIC CROSS SECTION
FOR $L_i^7(\alpha,\alpha)L_i^7$
$[k^2\sigma]_{cm}$ VS $E_{\alpha\ lab}$ AND $\theta_{cm°}$
$k^2\sigma$
10
1
.1
3.03 MeV
2.97 MeV
2.90 MeV
2.80 MeV
3.93 MeV
3.58 MeV
3.21 MeV
3.09 MeV
0 20 40 60 80 100 120 140 160
0 20 40 60 80 100 120 140 160 180
$\theta_{cm°}$
$\theta_{cm°}$

Figure 18

Figure 19

Elastic Differential Cross Sections for $L_i^7(\alpha, \alpha)L_i^7$

In the energy range covered by this figure, the angular distributions undergo rapid fluctuations both as a function of energy and angle. No analysis was undertaken above $E_{\alpha L} = 4.39$ MeV largely because of the apparent complexity of the scattering process and because of the paucity of reliable nuclear reaction data, at these energies.

See text pages 14 and 38.

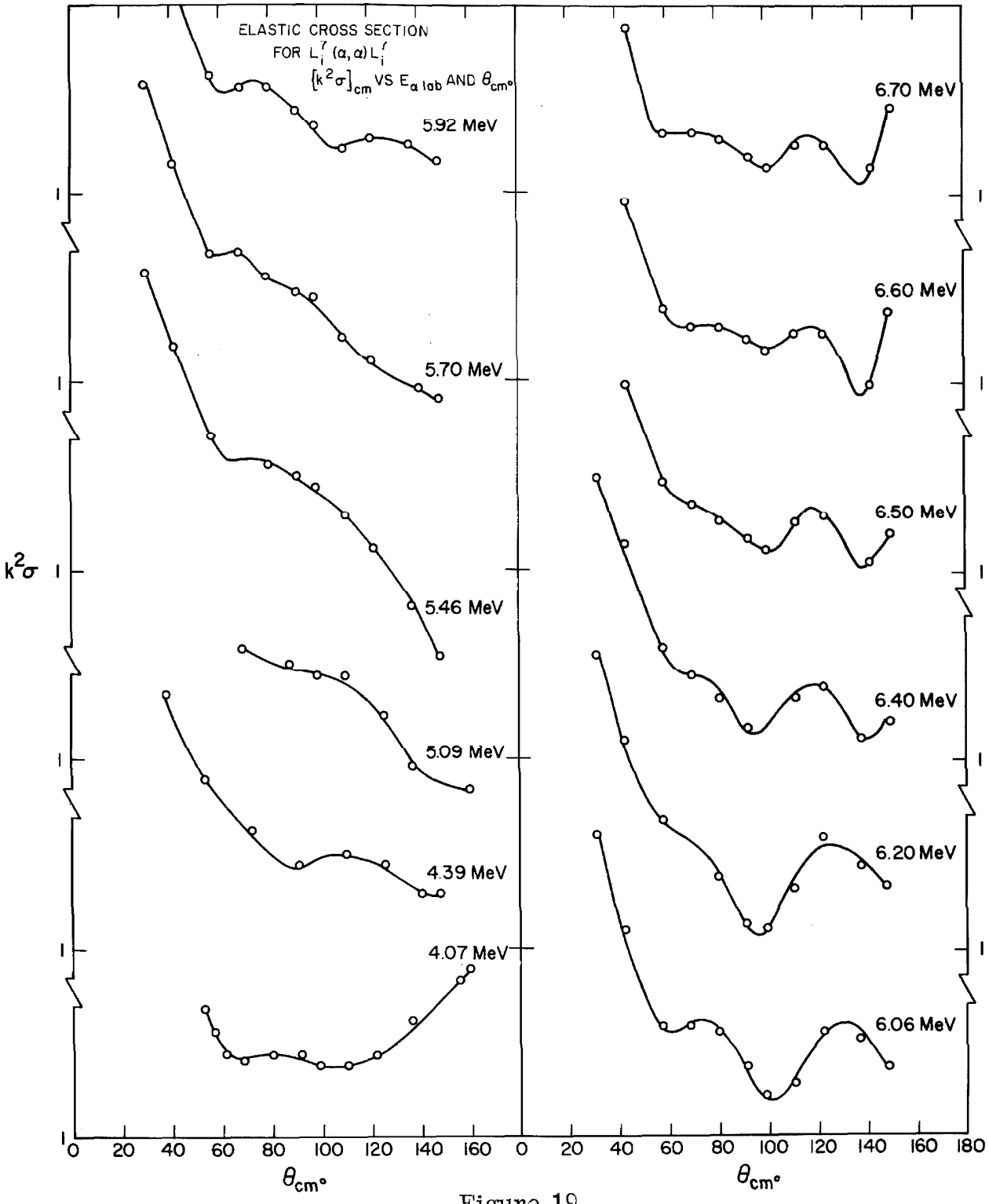
ELASTIC CROSS SECTION
FOR $L_i^f(\alpha,\alpha)L_i^f$
$[k^2\sigma]_{cm}$ VS $E_{\alpha\ lab}$ AND $\theta_{cm°}$
5.92 MeV
5.70 MeV
5.46 MeV
5.09 MeV
4.39 MeV
4.07 MeV
6.70 MeV
6.60 MeV
6.50 MeV
6.40 MeV
6.20 MeV
6.06 MeV
$k^2\sigma$
0 20 40 60 80 100 120 140 160
0 20 40 60 80 100 120 140 160 180
$\theta_{cm°}$
$\theta_{cm°}$

Figure 19

Figure 20

Elastic Differential Cross Sections for $L_i^7(\alpha, \alpha)L_i^7$

All the angular distributions shown in this figure show pronounced backward peaking. This may be an indication that non-resonant triton exchange scattering contributes sizeably to the nuclear cross section, at these energies.

See text pages 14 and 38.

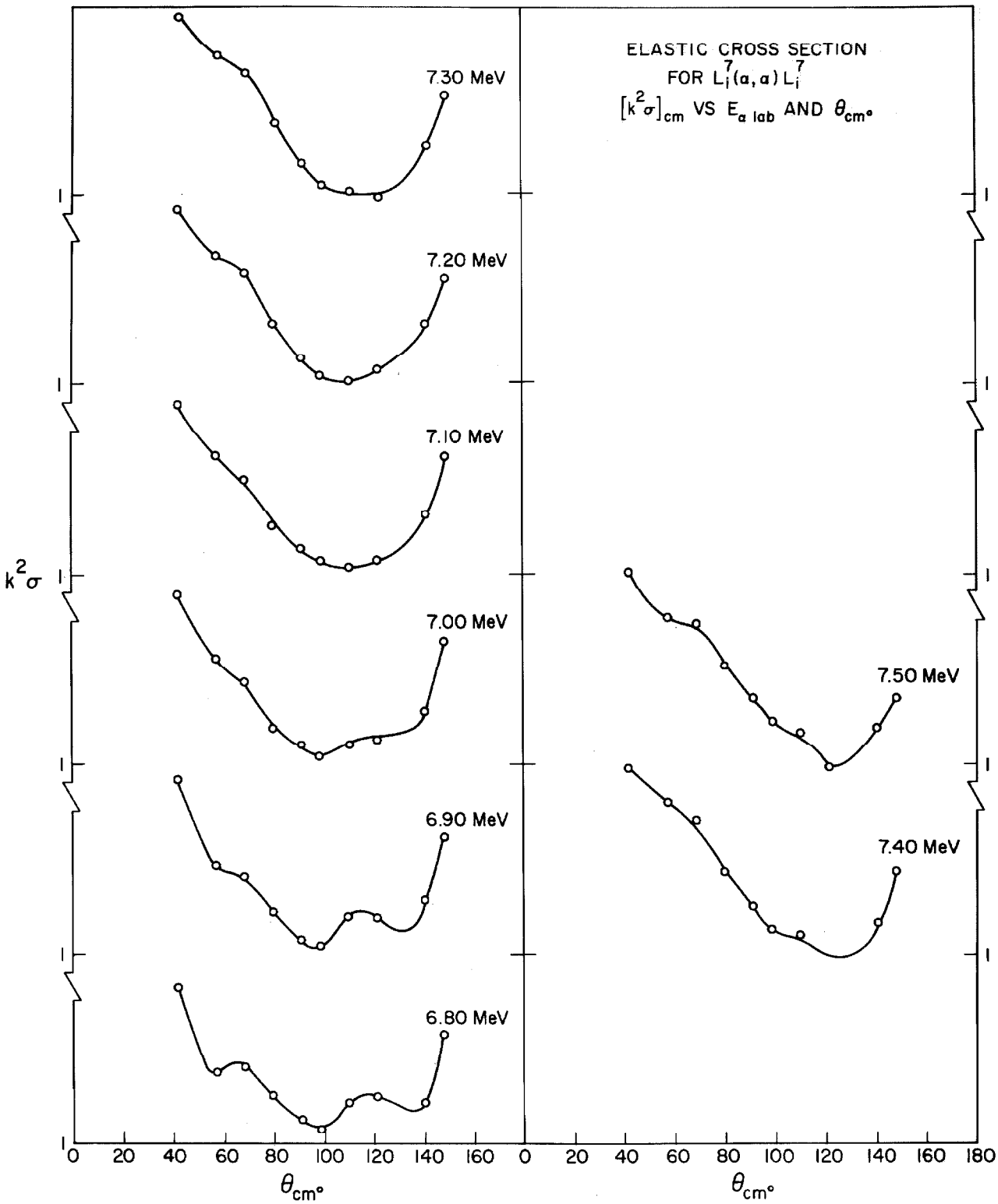
ELASTIC CROSS SECTION
FOR $L_i^7(\alpha,\alpha)L_i^7$
$[k^2\sigma]_{cm}$ VS $E_{\alpha\ lab}$ AND $\theta_{cm°}$
7.30 MeV
7.20 MeV
7.10 MeV
7.00 MeV
6.90 MeV
6.80 MeV
7.50 MeV
7.40 MeV
$k^2\sigma$
0 20 40 60 80 100 120 140 160
0 20 40 60 80 100 120 140 160 180
$\theta_{cm°}$
$\theta_{cm°}$

Figure 20

Figure 21

Dimensionless Calculated Total Inelastic Cross Sections

The solid curve represents a calculation of the total inelastic cross section for the reaction $Li^7(\alpha, \alpha')Li^{7*}(.48)$, using the model-program described in the text. The experimental points show the measured cross section and were taken from Figure 3. Levels number 3 and 6 contribute little to this cross section since they have a small inelastic width. There is good qualitative agreement between the computed and the measured cross section. This graph is typical of the fits that we have obtained.

See text pages 26-36.

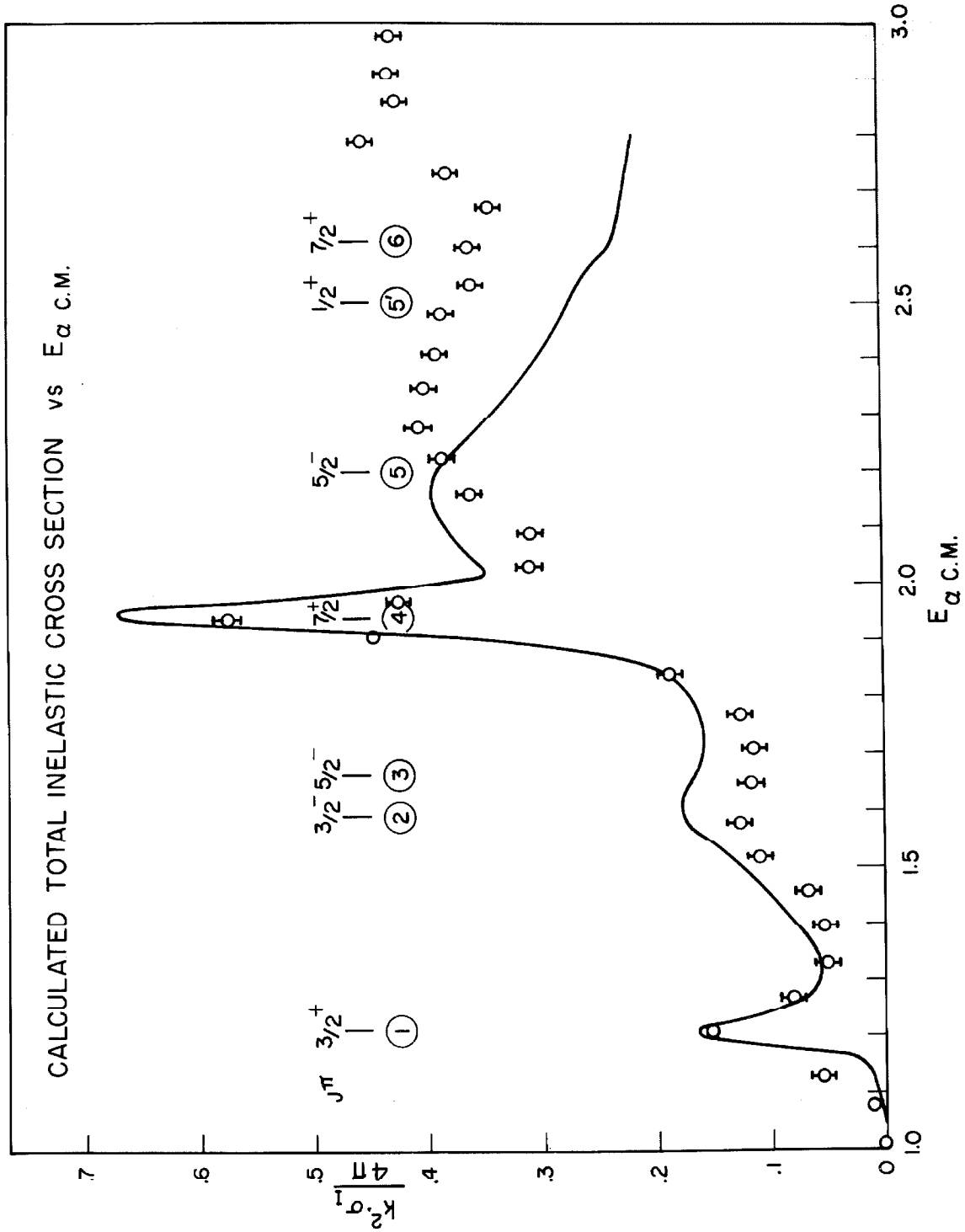
CALCULATED TOTAL INELASTIC CROSS SECTION vs E_α c.m.
$\frac{k^2\sigma_I}{4\pi}$
E_α C.M.
J^π
$3/2^+$ — ①
$3/2^-$ $5/2^-$ — ② ③
$7/2^+$ — ④
$5/2^-$ — ⑤
$1/2^+$ $7/2^+$ — ⑤' ⑥
0 .1 .2 .3 .4 .5 .6 .7
1.0 1.5 2.0 2.5 3.0

Figure 21

Figure 22

This represents a calculation of the elastic cross section at $\theta_{C.M.} = 159^{o}$ for the scattering $Li^{7}(\alpha, \alpha)Li^{7}$, using the model-program discussed in the text. The corresponding measured cross section is given in Figure 16. The C. M. energy is related to the laboratory energy by $E_{\alpha C.M.} \cong 0.636\, E_{\alpha L}$.

The parameters given in the figure were used in the model-program. A complete list of the level parameters is given in Table IV.

See text pages 26-36.

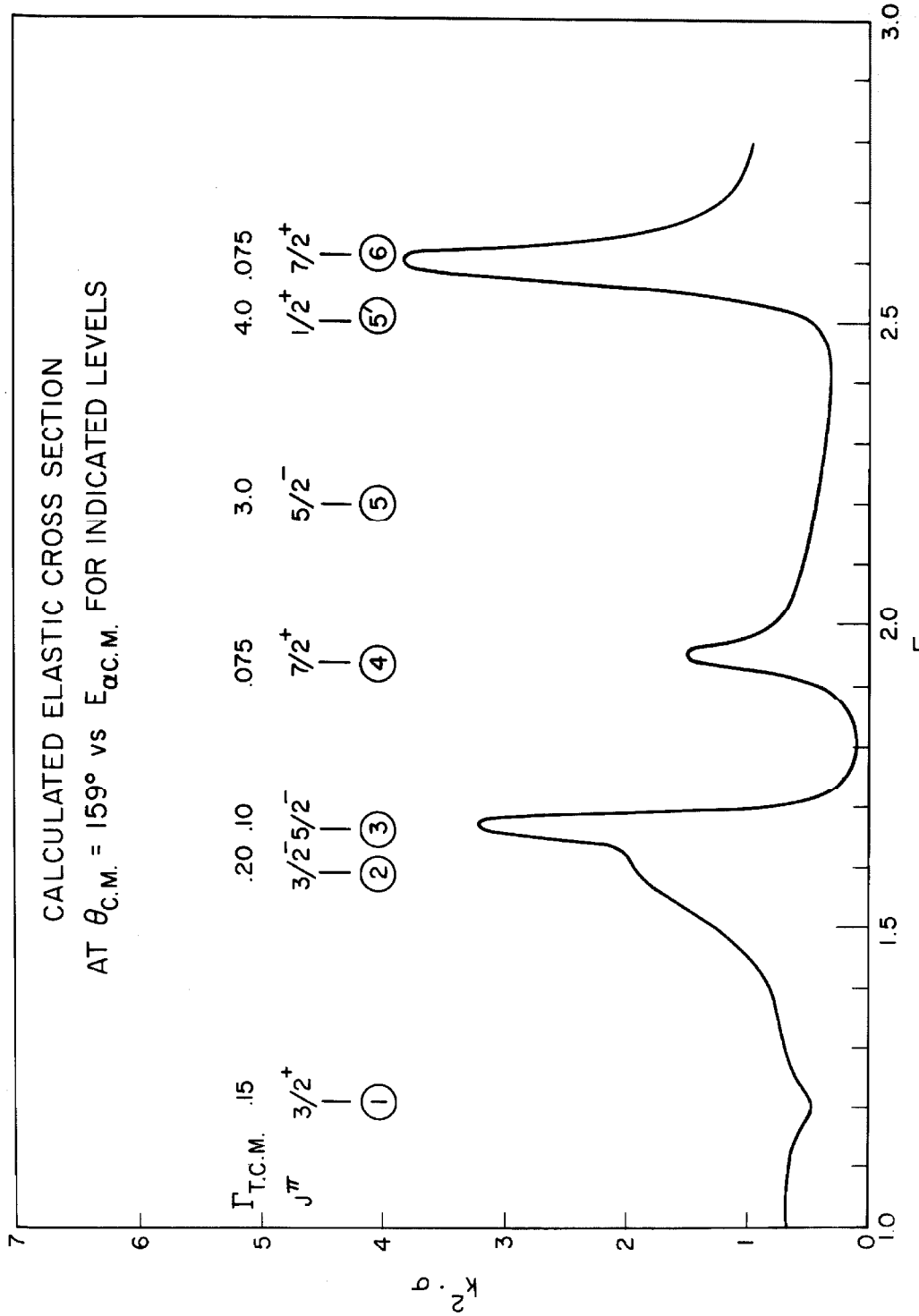
CALCULATED ELASTIC CROSS SECTION
AT $\theta_{C.M.}$ = 159° vs $E_{\alpha C.M.}$ FOR INDICATED LEVELS
$\Gamma_{T.C.M.}$ .15 .20 .10 .075 3.0 4.0 .075
J^{π} $3/2^+$ $3/2^-$ $5/2^-$ $7/2^+$ $5/2^-$ $1/2^+$ $7/2^+$
① ② ③ ④ ⑤ ⑤' ⑥
$K^2 \cdot a$
$E_{\alpha C.M.}$
0 1 2 3 4 5 6 7
1.0 1.5 2.0 2.5 3.0

Figure 22

Figure 23

This figure is similar to Figure 22 but at $\theta_{C.M.} = 90^{\circ}$. The experimental data is given in Figure 11. The agreement with the data is poorer here, for levels 2 and 3. We believe this is due to our failure to find the proper background. Such a failure becomes more obvious at forward angles because of the increased interference with the Coulomb amplitude. However, this difficulty should not invalidate our conclusions which are not very sensitive to the background at backward angles and for the inelastic cross section.

See text pages 26-36.

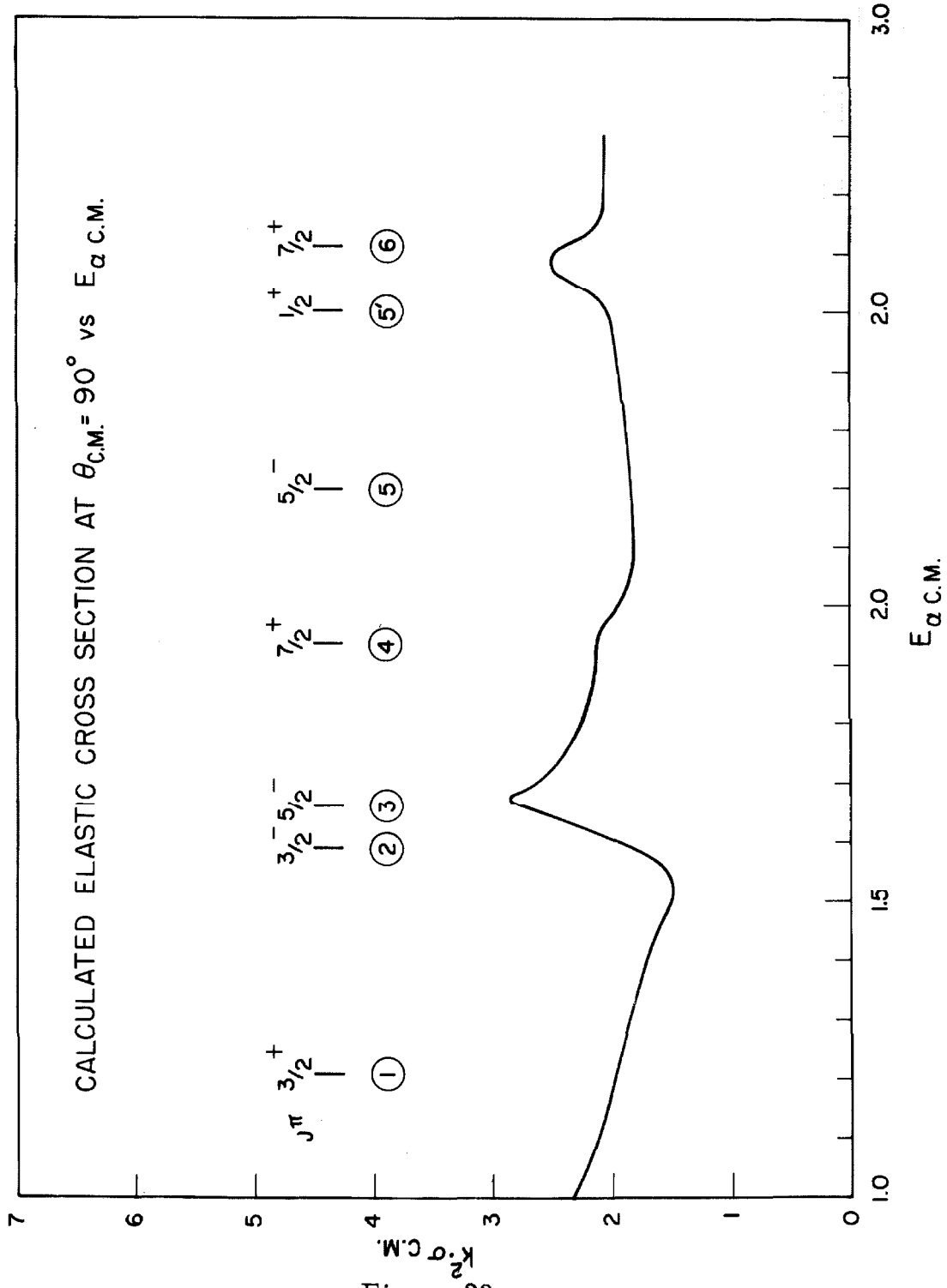
CALCULATED ELASTIC CROSS SECTION AT $\theta_{C.M.} = 90^\circ$ vs E_α C.M.
J^π
$3/2^+$
$3/2^-$
$5/2^-$
$7/2^+$
$5/2^-$
$1/2^+$
$7/2^+$
1
2
3
4
5
5'
6
$k^2\sigma$ C.M.
E_α C.M.
0
1
2
3
4
5
6
7
1.0
1.5
2.0
2.0
3.0

Figure 23

Figure 24

This graph represents the sum of the single particle energies in an axially-symmetric potential. The symbols used are those of Nilsson[8]. For example, 1^4 indicates that four particles are placed in the Nilsson orbit number one. These orbits may be characterized, in the limit $\eta = 0$, by giving the L value, the j value and $|k|$, the projection of j along the axis of symmetry. We then have the correspondence

Nilsson's number	L_j, $\|K\|^\pi$
1	$S_{1/2}$, $1/2^+$
2	$P_{3/2}$, $3/2^-$
3	$P_{3/2}$, $1/2^-$
4	$P_{1/2}$, $1/2^-$
6	$D_{5/2}$, $1/2^+$

K_{min} is then the smallest value of K that can be obtained with the given configuration.

See text page 46.

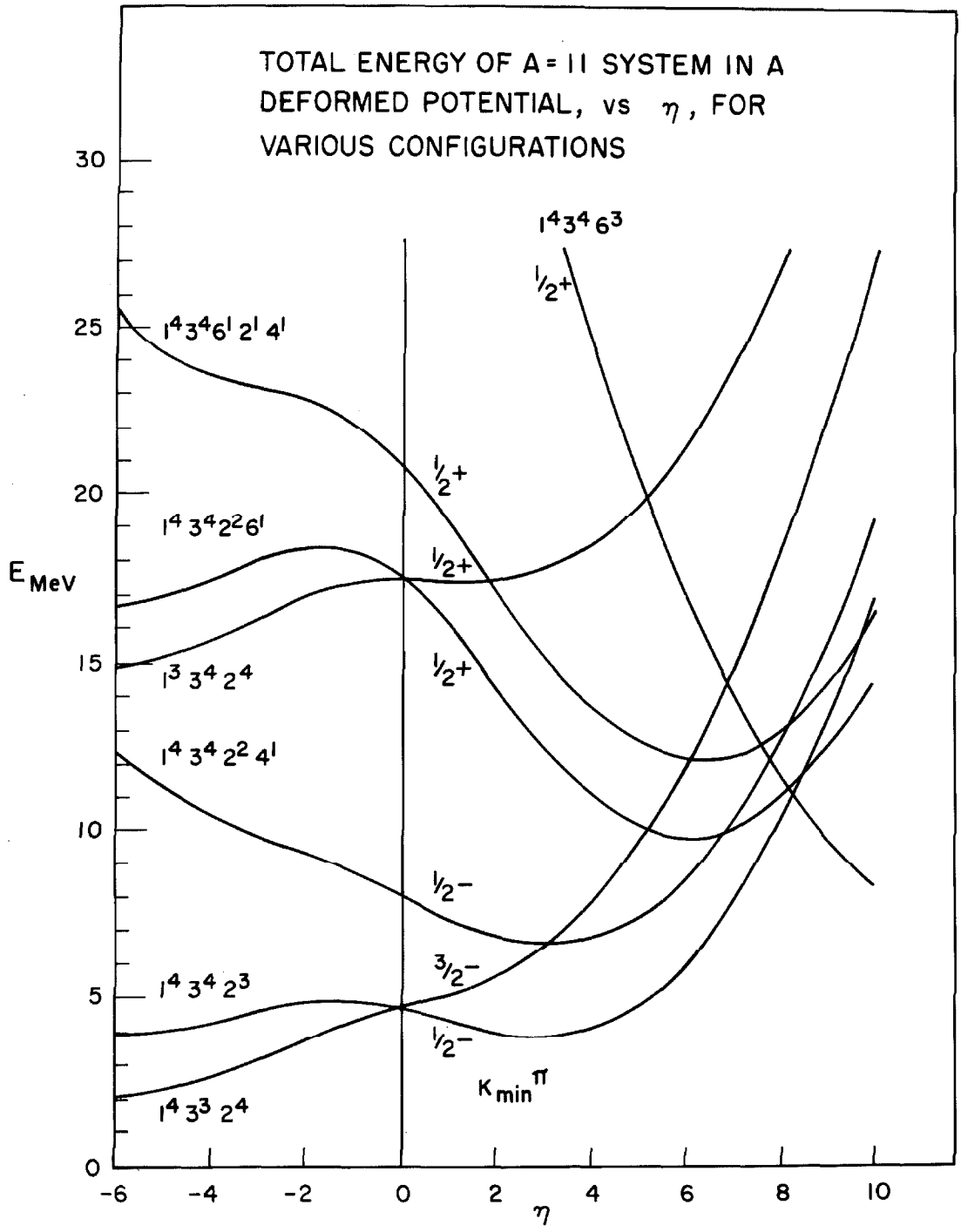
TOTAL ENERGY OF A = 11 SYSTEM IN A DEFORMED POTENTIAL, vs η, FOR VARIOUS CONFIGURATIONS
E MeV
η
K min π
1⁴3⁴6³
1/2+
1⁴3⁴6¹2¹4¹
1/2+
1⁴3⁴2²6¹
1/2+
1³3⁴2⁴
1/2+
1⁴3⁴2²4¹
1/2−
1⁴3⁴2³
3/2−
1⁴3³2⁴
1/2−
30
25
20
15
10
5
0
-6
-4
-2
0
2
4
6
8
10

Figure 24

Figure 25

Comparison of the Level Diagrams of B^{11} and C^{11}

We now present, at the conclusion of this work, a detailed comparison of the energy levels of B^{11} and C^{11}, below $E_{exc.} \cong 11.3$ MeV in B^{11}. The various references consulted in drawing this diagram are given in the text. The results of the present work concern the levels between 9.88 and 11.27 MeV exc. in B^{11}. Our assignments are consistent with those for the analogue levels in C^{11} for the cases where they are known in both nuclei. The nearly identical level spacing for the two nuclei, which has previously been observed at lower energy, continues up to the maximum excitation energy studied in detail in this experiment.

See text page 42.

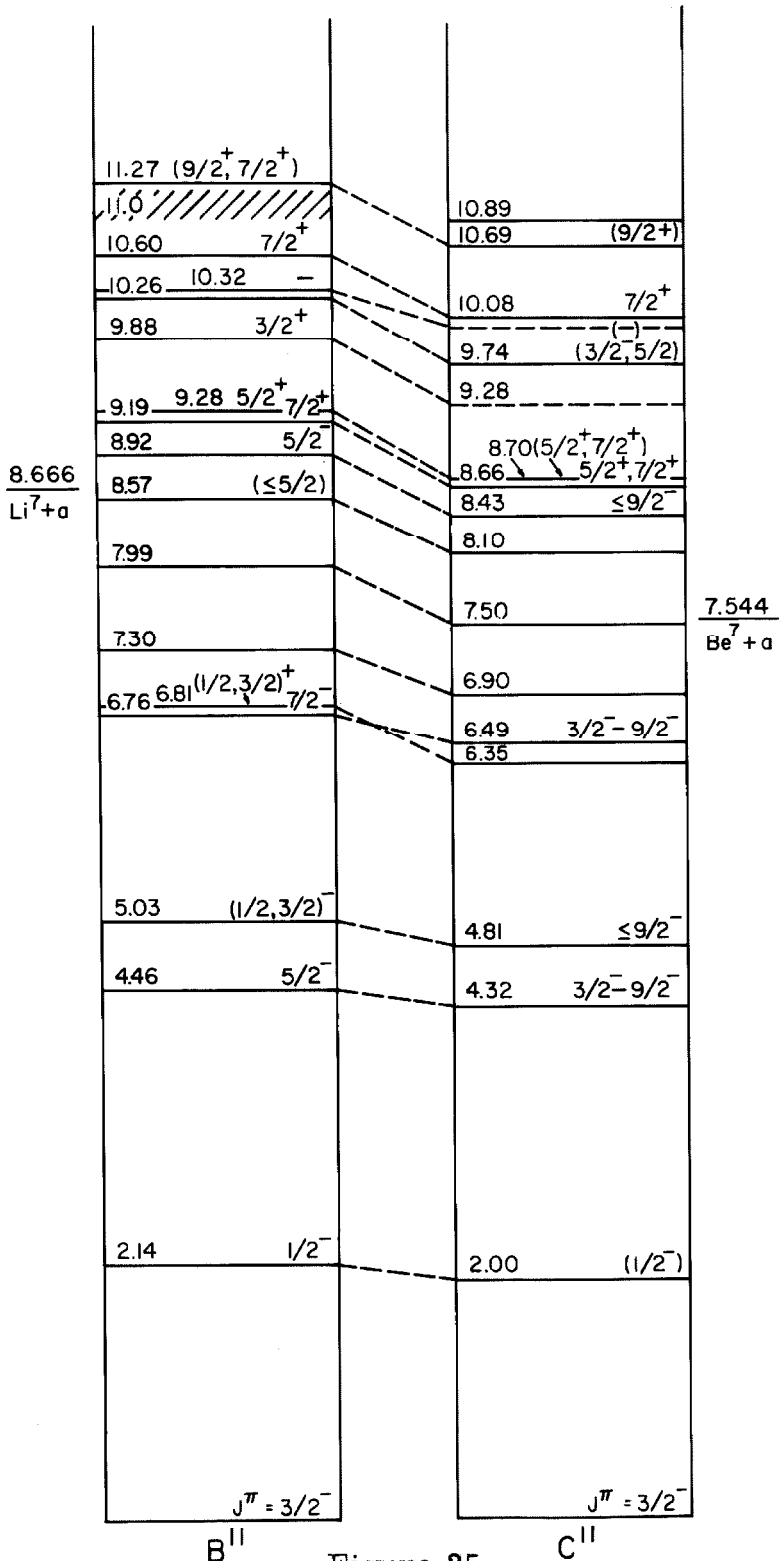
11.27 (9/2+, 7/2+)
11.0
10.60 7/2+
10.26 10.32 –
9.88 3/2+
9.19 9.28 5/2+ 7/2+
8.92 5/2–
8.57 (≤5/2)
8.666
Li7+a
7.99
7.30
6.76 6.81 (1/2,3/2)+ 7/2–
5.03 (1/2,3/2)–
4.46 5/2–
2.14 1/2–
Jπ = 3/2–
B11
10.89
10.69 (9/2+)
10.08 7/2+
(–)
9.74 (3/2–,5/2)
9.28
8.70(5/2+,7/2+)
8.66 5/2+, 7/2+
8.43 ≤9/2–
8.10
7.50
7.544
Be7 + a
6.90
6.49 3/2– 9/2–
6.35
4.81 ≤9/2–
4.32 3/2– 9/2–
2.00 (1/2–)
Jπ = 3/2–
C11

Figure 25